Doctoral Dissertation

Development of Natural Polymer Nanofiber-based Mesoporous Carbon *via* Nanoparticle Templating

ナノ粒子鋳型法による天然高分子ナノファイバー由来のメソポーラスカーボンの開発

MARK ADAM MALALUAN FERRY

June 2022

Graduate School of Engineering
Osaka University

Table of Contents

General Introduction

Biomass-based Porous Carbon

Porous carbon is a class of materials synthesized through pyrolysis at high temperature at the absence of oxygen, and characterized by its high surface area, developed hierarchical porosity, and chemical inertness.[1,2] Because of these properties, porous carbons are usually used for various applications such as adsorbents[3], supercapacitor electrodes[4], CO_2 capture[5], filters[6], and catalyst support media[7]. While prior carbon materials were made from fossil-fuel based products such as tar pitch[8] and fossil fuel-derived polymers like polyacrylonitrile[9,10] or resins[11] there is a focus on utilizing sustainably sourced raw materials to reduce reliance on non-renewable resources while reducing waste. The types of biomass used to form porous carbon range from directly carbonized plant and animal material, functionalized treated polymers, to fully converted biomass that does not resemble the initial raw resource. This should be noted since for biomass-derived porous carbon, the precursor material has a significant impact on the resulting structure and properties of the final carbon material product[12] (**Figure 1**).

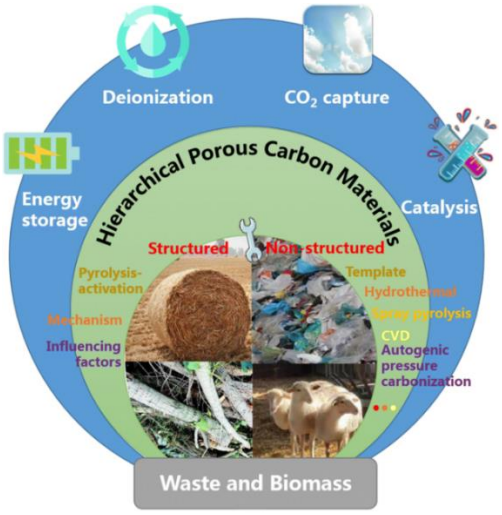

Figure 1. Diagram of biomass-derived carbon materials from their sources, treatment methods, and eventual applications from Zhou et al.[13]

The most commonly available type of study in biomass-derived carbon focuses on the immediate conversion of biomass through pyrolysis with some additional treatment. For directly converted biomass, the precursor could range from pine needle leaf litter[14], or produce waste[4,15], to biomass specifically removed from the environment like the invasive species water hyacinth[16]. The degree of pretreatment is considered minimal or does not significantly alter the chemical structure nor the existing morphology of the biomass. Some studies such as that by Jiang et al.[17] use tobacco straw simply powderized *via* ball milling and directly placed inside the furnace. Another study by Zhu et al.[18] used commercially available dewaxed cotton as acquired, albeit soaked in a magnesium nitrate solution that would later form MgO nanoparticles (NPs) to form pores. A study using cicada sloughs (molted exoskeleton remains) as a source of chitin was simply immersed in dilute HCl for 24 h to remove inorganic matter that would have contaminated the product. The morphology of the carbon material, specifically its microporosity, is usually retained from the original structure of the precursor (**Figure 2**). Utilizing biomass as is has benefits in reduced material cost, and ease of manufacturing, however variations in chemical composition and morphology between batches could lead to problems in product quality and property reproducibility.

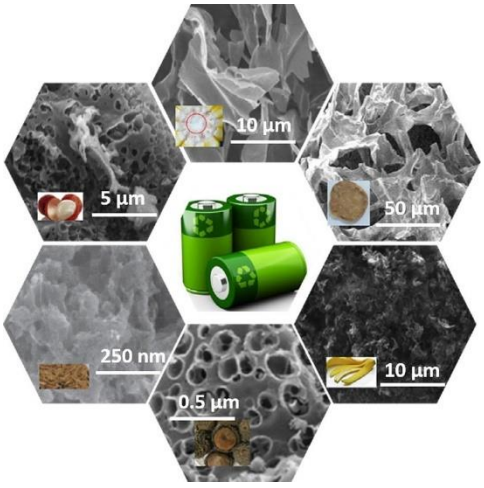

Figure 2. Diagram showing multiple biomass-based carbon sources used for lithium sulfur batteries with the macropore morphology being highly dependent on the waste biomass origin from Liu et al.[19]

Therefore, other researchers have gone around this problem by either extracting distinct compounds or polymers from biomass, or start from functionalized polymers that would then undergo various treatments. As an example, cellulose, hemicellulose, and lignin were extracted from wood[20–22], and these are used individually as carbon sources. Studies using cellulose in the form of carboxymethyl cellulose[23], or cellulose acetate[24]. Using a pure carbon precursor allows for more predictable reactions and thus could more easily observe structure-property correlations.

Another way of utilizing biomass is through monomers[25], oligomers[26], and polymers[27] that would then be fully treated to form carbon with a structure that is fully artificially synthesized. There would be little to no resemblance to naturally-occurring structures unless intentionally recreated. Some studies perform phase separation and use the gel as the carbon precursor while the sol formed the porous channels that would run across the monolith[28–30]. However, not all biomass can undergo phase separation, which limits carbon precursor selection. Another widely used method is hydrothermal treatment (HT), which induces crosslinking and oxidation at high temperature and high pressure in a stainless-steel autoclave. With HT most biomass will precipitate into a solid called a hydrochar, which is mostly uniform in structure in composition.

Hydrothermally treated cellulose

In the case of cellulosic polymers (cellulose, hemicellulose, lignin, chitin, chitosan, etc) the uniform composition has been described to be similar to phenol formaldehyde resin due to the breakdown of the polymer into constituent aqueous phase, and organic phase-soluble compounds. According to a study by Gagic et al.[31], cellulose first undergoes chain scission into glucose, cellobiose, or lactose (**Figure 3**). All three compounds eventually form glucose after 1h, then undergo 6→5-member ring transformation into fructose, which is then further

oxidized to form 5-hydroxymethylfurural (5-HMF) which is a keystone component where the rest of the hydrochar is built. If glucose or fructose do not form 5-HMF, then the ring opens and decomposes into molecules such as erythrose, pyruvaldehyde, dihydroxyacetone. These compounds are considered to comprise the water-soluble phase of a hydrothermal system. In the organic phase-soluble system (**Figure 4**), 5-HMF further breaks down either by ring opening to form saturated and unsaturated acids such as levulinic acid, 1,3-butadien carboxylic acid, and 4-hydroxy-4-methyl-2-pentanone. The rest forms aromatic species that lead to the aromatization of the hydrochar in bulk, giving the resin-like structure. The decomposition of cellulose, hemicellulose, and lignin were confirmed to be a function of temperature and time, and described as the decomposition severity factor ($logR_0$)[32]. They also noted that there is no correlation between solid and liquid content. Chitin and chitosan despite containing amines and amides are still reported to undergo a similar decomposition mechanism, albeit with side reactions specific to nitrogen-containing compounds found in both the aqueous and organic phases[33,34]. After a certain period of time,

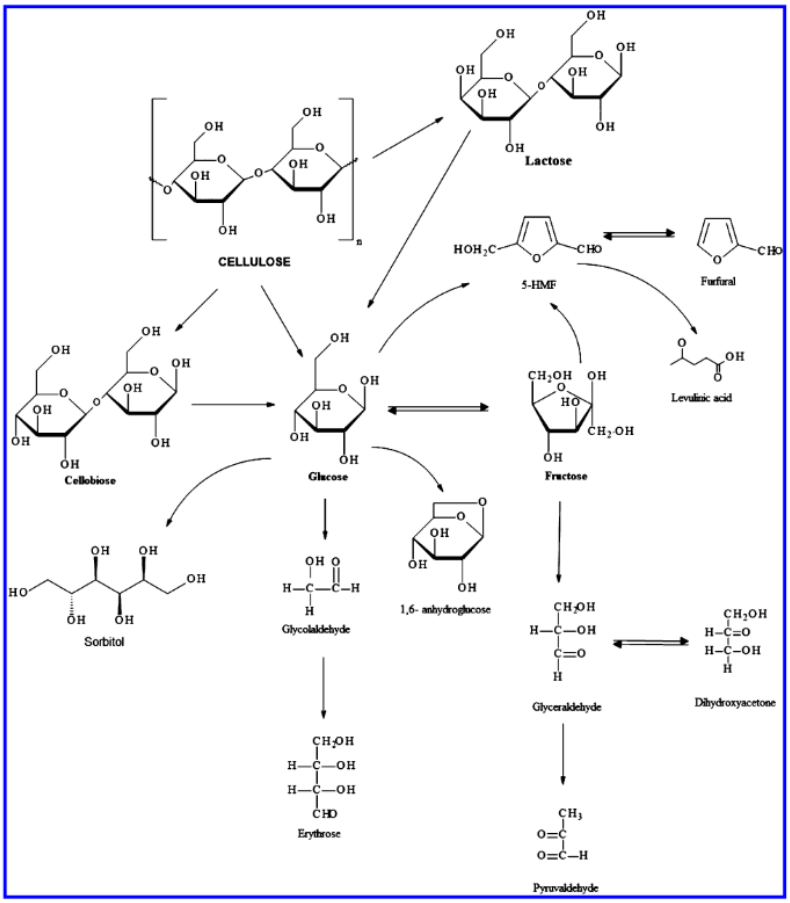

Figure 3. Reaction pathway of aqueous phase-soluble products during hydrothermal treatment of cellulose from Gagic et al.[31]

the decomposition products from the starting material crosslink and aggregate, forming the solid. A study by Ho et al.[35] showed that the solids form through nucleation following the La Mer model[36], with nuclei formed from hydrophobic-hydrophilic interactions and growing until a critical mass is reached and the precipitates start fusing to one another.

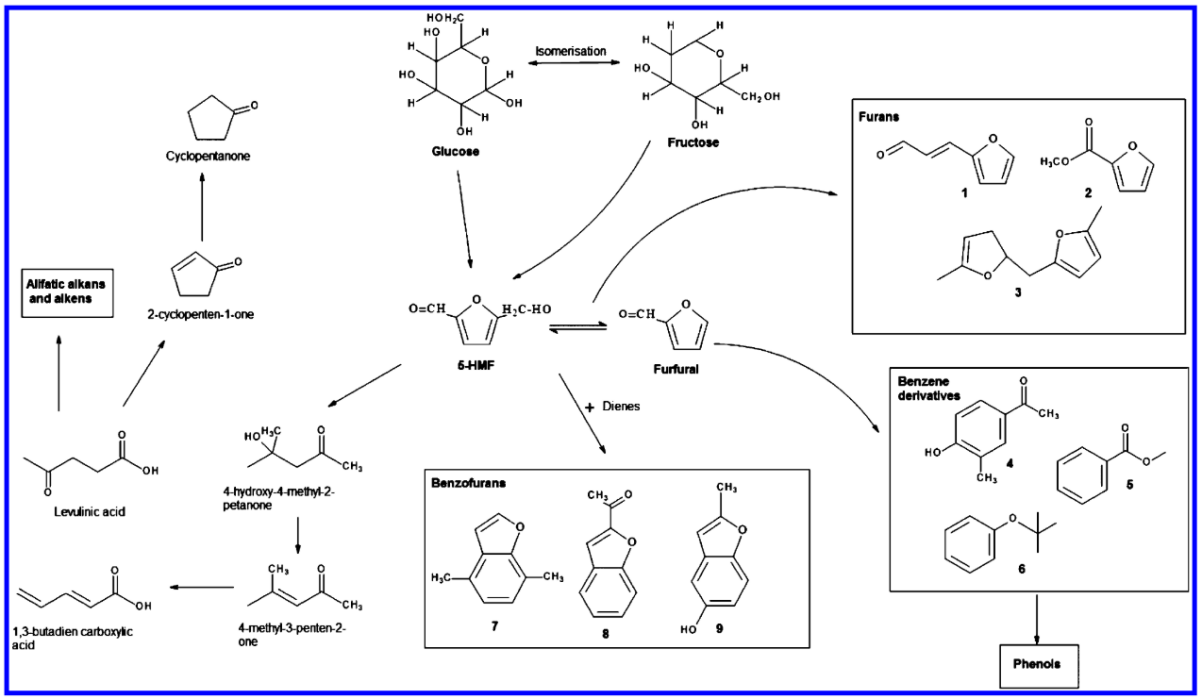

Figure 4. Reaction pathway of organic phase-soluble products during hydrothermal treatment of cellulose from Gagic et al.

Studies on hydrochar synthesized from monosaccharides and polysaccharides such as glucose[26,37], fructose[38,39], and sucrose[26], as well as polymers such as cellulose[32,40], chitin[41,42], and chitosan[43,44]. In general, hydrochar-derived carbon materials exhibit high surface area from varying degrees of porosity and high oxygen content that steadily decreases with increasing carbonization temperature[26,37]. In order to control the structure of hydrothermally treated biomass to be similar to phase-separated carbon precursors, structure-directing agents such as pore-forming template materials must be mixed in the hydrochar matrix.

Nanoparticle Templating

There are a range of materials to choose from when it comes to templating hydrochar. Metal oxide NPs are characterized by their thermal and dimensional stability, which allows the NP to remain relatively intact even after heat treatment[2]. To form the pore, the template needs to be removed usually *via* acid washing to dissolve the NPs[45]. The wash could then be isolated and the NPs reformed, preventing all of the materials from fully going to waste. Silica[10] was one of the earlier NPs to be used, followed by MgO, ZnO[46], and zeolites[47]. Interestingly, metal oxide NPs can be formed *in situ* during hydrothermal treatment. MgO NPs were reported to be formed from magnesium acetate and magnesium citrate[48,49]. Discrete MgO and $Mg(OH)_2$[50] NPs are commercially available and are an economically viable option as well. ZnO on the other hand have shown interesting shapes such as tetrahedra and even star-like conformations that resulted in unique pore structures[46].

Another class of materials used for templating is polymer NPs, such as polystyrene NPs[51], poly(methyl methacrylate) (PMMA) NPs[52], and block copolymer micelles[53,54]. Because polymers thermally degrade at temperatures below the pyrolysis onset temperature, care has to be taken to make sure that the polymer NP degrades after the carbon precursor structure has set[54] to prevent pore collapse. Polymer NPs however have an advantage in template removal: simultaneous pore formation and carbonization occurs during heat treatment, shortening the synthesis method.

Natural polymer nanofiber as nanoparticle template stabilizer

When nanoparticle templating is not used in tandem with hydrothermal treatment, the NP must be properly stabilized within the matrix,[55] otherwise proper pore formation might not occur. Therefore, strategies to stabilize NPs without over-reliance on crosslinking must be adapted to ensure pore structure reproducibility. One class of materials that is not yet fully

utilized for nanoparticle templating is the use of natural polymer nanofibers. Nanofibers have properties that lie between neat fibers and discrete polymers, allowing NP stabilization by trapping the NPs within the fiber network[56,57]. A study by Lee et al.[58] has shown that cellulose nanofibers could stabilize zeolitic imidazole frameworks (ZIF-8/67) by allowing it to grow on the fiber surface[56]. Given the potential of nanoparticle templating to produce hierarchically porous carbons[53], researching methods to improve this technology could greatly help drive scientific and economic incentive to utilize biomass as a commercial carbon precursor.

Contents of this dissertation

In this dissertation, the advantage of using natural polymer-based nanofibers as the sustainably sourced precursor material for porous carbon synthesized in tandem with nanoparticle templating is presented. There are three chapters corresponding to the research the author has published with each having a different set of conditions that showcase the broad potential of this porous carbon synthesis technique.

Chapter 1

In this chapter, TEMPO-oxidized cellulose nanofibers (TOCN) were used as the carbon precursor, while polystyrene latex (PSL) was used as the nanoparticle template. Hydrothermal treatment with subsequent carbonization was done to yield porous carbon monoliths (CMs). To stabilize PSL within the TOCN matrix throughout the hydrothermal treatment, a triblock copolymer surfactant called Pluronic F-127 (PF127) was added. It was found that PF127 had a dual purpose in this study: 1) it coated the surface of PSL, and 2) excess PF127 precipitated in larger spheres which then acted as a secondary template. The inclusion of two templates of differing sizes resulted in a unique morphology wherein fused hollow carbon spheres exhibited porous honeycomb spheres which allow access to the inner void of the carbon sphere. Because

of this multimodal porosity, the CMs exhibited high surface area. Together with a balance of surface wettability, the carbon monoliths exhibited excellent oil-water separation capacity better than that of commercially available activated carbon pellets of similar size.

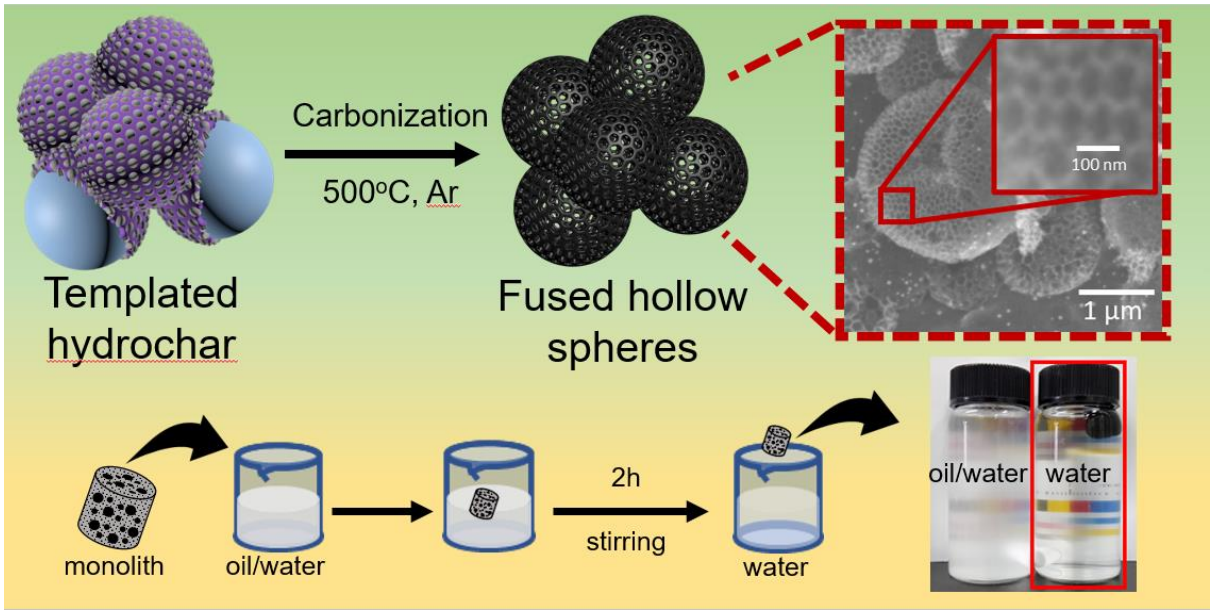

Figure 5. Graphical abstract of Chapter 1.

Chapter 2

In this chapter, the hydrothermal treatment method from the previous chapter was optimized by using TEMPO-oxidized chitin nanofibers (CtNF) to directly stabilize PSL without needing an interface stabilizing polymer. Without the risk of accidental secondary templates within the system, CMs synthesized with CtNF showed highly uniformly distributed pores which resulted in a highly inter-connected network within the entire monolith. To impart the material with hierarchical porosity, chemical activation with KOH was performed to selectively form micropores on the surface of the CM, and forming activated hierarchically porous carbon (AHPC). The uniform pore structure formed by CTNF however had another effect: it induced selective removal of amorphous carbon during activation of AHPC, which resulted in the exposure of graphene edge sites. Together with high surface area and hierarchical porosity, the

exposure of edge sites made AHPC have incredibly high electrochemical specific capacitance. AHPC also exhibited stable charge-discharge behavior in cyclic voltammetry at various scan rates and in galvanostatic charge-discharge at various current densities. Lastly, charging AHPC 2000 times at 5 A g^{-1} and 10 000 times at 10 A g^{-1} confirmed that the material can be used for potential long-term applications with high degree of reliable input-output. AHPC can then be considered as a potential eco-friendly supercapacitor electrode.

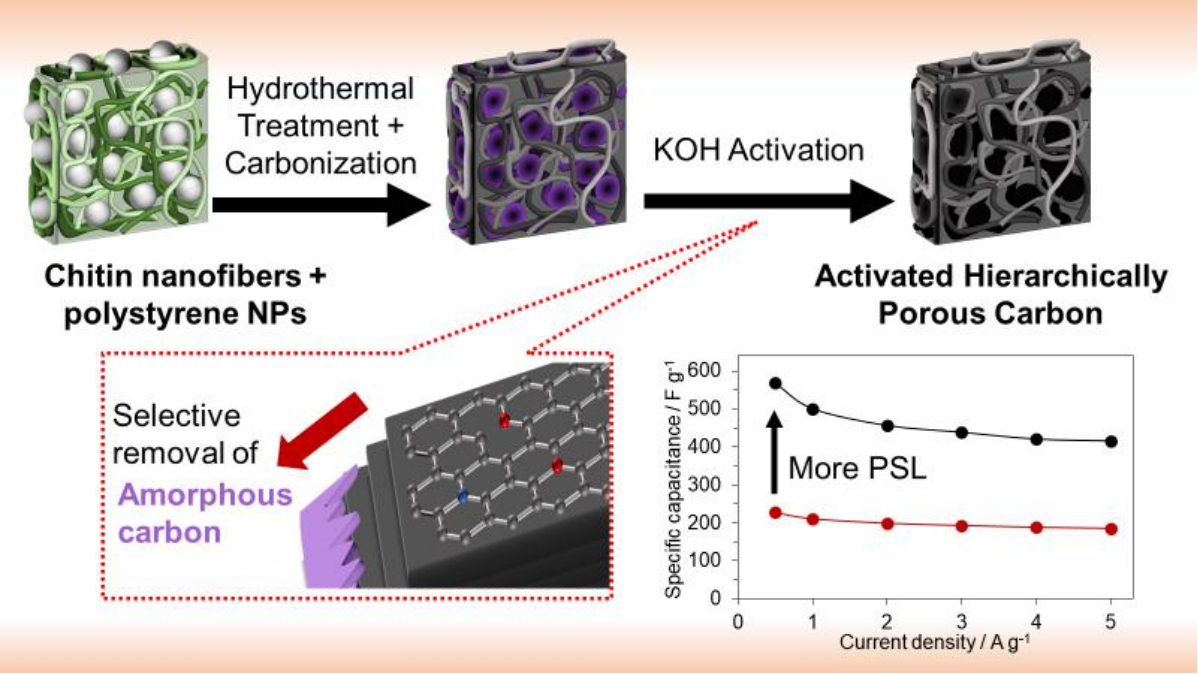

Figure 6. Graphical abstract of Chapter 2.

Chapter 3

In Chapter 3, the process of synthesizing porous carbon for supercapacitor electrodes from Chapter 2 was streamlined to make both the reagents and the synthesis method have as little environmental impact as possible. Going back to cellulose nanofibers as the carbon precursor, direct conversion of TOCN into templated activated carbon (TAC) was performed. Because hydrothermal treatment was omitted asa pre-treatment step, PSL was replaced with 50 nm MgO NPs which can be stabilized by TOCN through nanofiber physical entanglement alone.

Furthermore, instead of the typical 2-step heat treatment process where carbonization and activation are performed separately, in this research an integrated heating, carbonization, and activation was conducted consecutively without any cooldown between treatment phases. In the integration of activation in the same heat treatment step, TOCN was then impregnated with KOH prior to inserting in the furnace. It was found that the same hierarchical porosity could be achieved through the facile method, proving a pseudo-honeycomb structure. While the specific capacitance of TAC was lower than that of AHPC from Chapter 2, the ease of fabrication and compatibility with scaling to larger production allows this synthesis method to be more practical and commercializable.

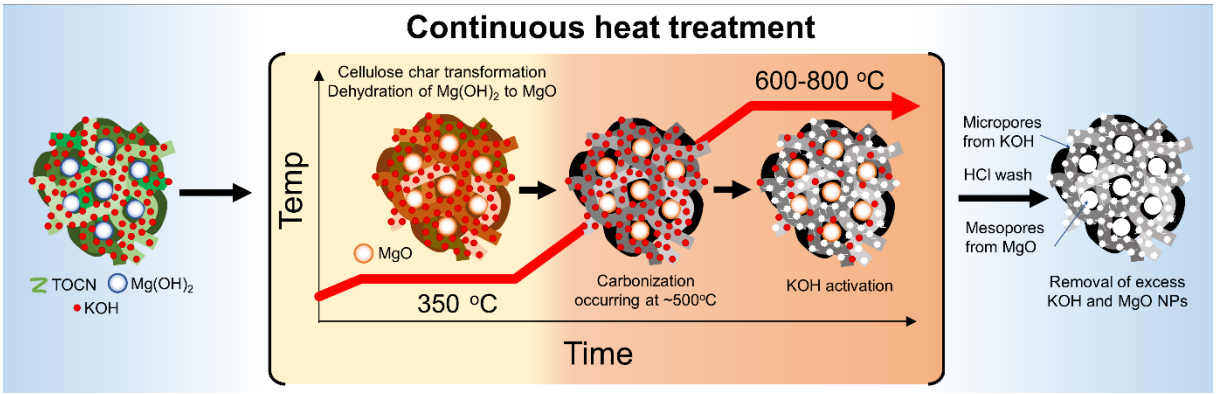

Figure 7. Graphical abstract of Chapter 3.

References

[1] S. Dutta, A. Bhaumik, K. C. W. Wu, *Energy Environ. Sci.* **2014**, *7*, 3574–3592.
[2] J. Lee, J. Kim, T. Hyeon, *Adv. Mater.* **2006**, *18*, 2073–2094.
[3] Z. Gong, K. Alef, B. M. Wilke, P. Li, *J. Hazard. Mater.* **2007**, *143*, 372–378.
[4] Z. Wang, Y. Tan, Y. Yang, X. Zhao, Y. Liu, L. Niu, B. Tichnell, L. Kong, L. Kang, Z. Liu, F. Ran, *J. Power Sources* **2018**, *378*, 499–510.
[5] J. Du, W. C. Li, Z. X. Ren, L. P. Guo, A. H. Lu, *J. Energy Chem.* **2020**, *42*, 56–61.
[6] Y. Yang, J. Li, H. Wang, X. Song, T. Wang, B. He, X. Liang, H. H. Ngo, *Angew. Chemie - Int. Ed.* **2011**, *50*, 2148–2150.
[7] M. Borghei, J. Lehtonen, L. Liu, O. J. Rojas, *Adv. Mater.* **2018**, *30*, 1–27.
[8] Y. Jiang, Z. He, X. Cui, Z. Liu, J. Wan, Y. Liu, F. Ma, *New J. Chem.* **2022**, 6078–6090.
[9] B. Xu, F. Wu, R. Chen, G. Cao, S. Chen, Z. Zhou, Y. Yang, *Electrochem. commun.* **2008**, *10*, 795–797.
[10] D. Lee, J.-Y. Jung, M.-J. Jung, Y.-S. Lee, *Chem. Eng. J.* **2015**, *263*, 62–70.
[11] J. Qu, Q. Han, F. Gao, J. Qiu, *New Carbon Mater.* **2017**, *32*, 86–91.
[12] J. Wang, P. Nie, B. Ding, S. Dong, X. Hao, H. Dou, X. Zhang, *J. Mater. Chem. A* **2017**, *5*, 2411–2428.
[13] X. L. Zhou, H. Zhang, L. M. Shao, F. Lü, P. J. He, *Waste and Biomass Valorization* **2021**, *12*, 1699–1724.
[14] C. Leng, K. Sun, J. Li, J. Jiang, *ACS Sustain. Chem. Eng.* **2017**, *5*, 10474–10482.
[15] S. Li, Q. Chen, Y. Gong, H. Wang, D. Li, Y. Zhang, Q. Fu, C. Pan, *ACS Omega* **2020**, *5*, 29913–29921.
[16] H. Shokry, M. Elkady, E. Salama, *Sci. Rep.* **2020**, *10*, 1–17.
[17] B. Jiang, L. Cao, Q. Yuan, Z. Ma, Z. Huang, Z. Lin, P. Zhang, *Materials (Basel).* **2022**, *15*, 1–11.
[18] C. Zhu, T. Akiyama, *Green Chem.* **2016**, *18*, 2106–2114.
[19] P. Liu, Y. Wang, J. Liu, *J. Energy Chem.* **2019**, *34*, 171–185.
[20] S. D. Stefanidis, K. G. Kalogiannis, E. F. Iliopoulou, C. M. Michailof, P. A. Pilavachi, A. A. Lappas, *J. Anal. Appl. Pyrolysis* **2014**, *105*, 143–150.
[21] S. Chen, Y. Xia, B. Zhang, H. Chen, G. Chen, S. Tang, *J. Hazard. Mater.* **2021**, *408*, 124956.
[22] Y. Tan, X. Wang, F. Xiong, J. Ding, Y. Qing, Y. Wu, *Ind. Crops Prod.* **2021**, *171*, 113980.
[23] S. Lin, L. Mo, F. Wang, *J. Electrochem. Energy Convers. Storage* **2022**, *19*, 1–9.
[24] Y. Wang, J. Cui, Q. Qu, W. Ma, F. Li, W. Du, K. Liu, Q. Zhang, S. He, C. Huang, *Microporous Mesoporous Mater.* **2022**, *329*, 111545.
[25] P. Li, C.-N. Feng, H.-P. Li, X.-L. Zhang, X.-C. Zheng, *J. Alloys Compd.* **2021**, *851*, 156922.
[26] L. Yu, C. Falco, J. Weber, R. J. White, J. Y. Howe, M. M. Titirici, *Langmuir* **2012**, *28*, 12373–12383.
[27] H. Wang, X. Li, J. Peng, Y. Cai, J. Jiang, Q. Li, *Nanoscale Adv.* **2021**, *3*, 4858–4865.
[28] Y. Shu, J. Maruyama, S. Iwasaki, S. Maruyama, Y. Shen, H. Uyama, *J. Power Sources* **2017**, *364*, 374–382.
[29] A. Dobashi, J. Maruyama, Y. Shen, M. Nandi, H. Uyama, *Carbohydr. Polym.* **2018**, *200*, 381–390.
[30] J. Zhou, Z. Sun, M. Chen, J. Wang, W. Qiao, D. Long, L. Ling, *Adv. Funct. Mater.* **2016**, *26*, 5368–5375.
[31] T. Gagić, A. Perva-Uzunalić, Ž. Knez, M. Škerget, *Ind. Eng. Chem. Res.* **2018**, *57*, 6576–6584.

[32] A. M. Borrero-López, E. Masson, A. Celzard, V. Fierro, *Ind. Crops Prod.* **2018**, *124*, 919–930.
[33] E. Savitri, Sumarno, A. Rosyadi, *Macromol. Symp.* **2015**, *353*, 212–219.
[34] S. Suenaga, M. Osada, *Cellulose* **2018**, *25*, 6873–6885.
[35] H. C. Ho, M. Goswami, J. Chen, J. K. Keum, A. K. Naskar, *Sci. Rep.* **2018**, *8*, 1–13.
[36] V. K. La Mer, *Ind. Eng. Chem.* **1952**, *44*, 1270–1277.
[37] N. Brun, C. A. García-González, I. Smirnova, M. M. Titirici, *RSC Adv.* **2013**, *3*, 17088–17096.
[38] W. Zhao, M. Zhang, P. Pan, D. Song, S. Huang, J. Wei, X. Li, W. Qi, K. Zhang, J. Zhao, Z. Yang, *Surf. Coatings Technol.* **2017**, *320*, 595–600.
[39] D. Jung, M. Zimmermann, A. Kruse, *ACS Sustain. Chem. Eng.* **2018**, *6*, 13877–13887.
[40] M. Sevilla, A. B. Fuertes, *Chem. Phys. Lett.* **2010**, *490*, 63–68.
[41] R. J. White, M. Antonietti, M.-M. Titirici, *J. Mater. Chem.* **2009**, *19*, 8645.
[42] I. F. Nata, S. S. S. Wang, T. M. Wu, C. K. Lee, *Soft Matter* **2012**, *8*, 3522–3525.
[43] Q. Wu, M. Gao, S. Cao, J. Hu, L. Huang, S. Yu, A. J. Ragauskas, *J. Taiwan Inst. Chem. Eng.* **2019**, *101*, 231–243.
[44] X. Tong, Z. Chen, H. Zhuo, Y. Hu, S. Jing, J. Liu, L. Zhong, *Carbohydr. Polym.* **2019**, *207*, 764–774.
[45] Y. Kado, Y. Soneda, *Microporous Mesoporous Mater.* **2021**, *310*, 110646.
[46] B. Yan, J. Zheng, F. Wang, L. Zhao, Q. Zhang, W. Xu, S. He, *Mater. Des.* **2021**, *201*, 109518.
[47] T. Kyotani, T. Nagai, S. Inoue, A. Tomita, *Chem. Mater.* **1997**, *9*, 609–615.
[48] T. Morishita, Y. Soneda, T. Tsumura, M. Inagaki, *Carbon N. Y.* **2006**, *44*, 2360–2367.
[49] T. Morishita, T. Tsumura, M. Toyoda, J. Przepiórski, A. W. Morawski, H. Konno, M. Inagaki, *Carbon N. Y.* **2010**, *48*, 2690–2707.
[50] E. Unur, S. Brutti, S. Panero, B. Scrosati, *Microporous Mesoporous Mater.* **2013**, *174*, 25–33.
[51] R. Balgis, T. Ogi, A. F. Arif, G. M. Anilkumar, T. Mori, K. Okuyama, *Carbon N. Y.* **2015**, *84*, 281–289.
[52] X. Meng, H. Cui, J. Dong, J. Zheng, Y. Zhu, Z. Wang, J. Zhang, S. Jia, J. Zhao, Z. Zhu, *J. Mater. Chem. A* **2013**, *1*, 9469.
[53] S. Kubo, R. J. White, K. Tauer, M.-M. Titirici, *Chem. Mater.* **2013**, *25*, 4781–4790.
[54] N. Díez, M. Sevilla, A. B. Fuertes, *Carbon N. Y.* **2021**, *178*, 451–476.
[55] Y. Xia, Z. Yang, R. Mokaya, *Nanoscale* **2010**, *2*, 639–659.
[56] J. Tang, J. Sisler, N. Grishkewich, K. C. Tam, *J. Colloid Interface Sci.* **2017**, *494*, 397–409.
[57] Z. Y. Wu, H. W. Liang, L. F. Chen, B. C. Hu, S. H. Yu, *Acc. Chem. Res.* **2016**, *49*, 96–105.
[58] Y. R. Lee, H. Yoo, J. Choi, W. S. Ahn, *Cellulose* **2020**, *27*, 2723–2735.

Chapter 1

Fused sphere carbon monoliths with honeycomb-like porosity from cellulose nanofibers for oil and water separation

1.1. Introduction

Oil-water separation is a crucial technology in protecting our freshwater and saltwater ecosystems from accidental oil spills. While other materials already exist to perform the same application such as cotton, wood, and lauric acid-derived materials [1], utilizing waste biomass in upcycling allows for waste to reintegrate in a more circular economy as oil adsorbent materials.

Cellulose is one of the most abundant natural polymers, and thus was chosen as the first material to be used as the carbon precursor. In order to form cellulose into a nanofiber, TEMPO oxidation[2], to obtain nanofibers with uniform size. Furthermore, the selective oxidation of the C6 -OH group into carboxylic acid group allows ester crosslinking between fibers, which further stabilizes the cellulose matrix after hydrothermal treatment.

Polystyrene latex (PSL) was chosen as the nanoparticle template in this study due to its thermal degradation temperature at around 400 ^{o}C[3] allowing for stable templating during hydrothermal treatment, as well as simultaneous carbonization and template removal occurring at its degradation temperature. This allows for the method to be more rapid and facile, with the pores of the carbon material being present right after heat treatment. PSL however does not readily template with TOCN due to both having negative ζ-potential[4], repelling one another. Thus, a triblock copolymer surfactant called Pluronic F-127 (PF127) was chosen to stabilize PSL within TOCN. PF127 has been shown to stabilize PSL within fructose-based hydrochar, such as from the study of Kubo et al.[5] while also forming larger macro-sized channels within the monolith, providing hierarchical porosity.

In this study, TOCN, together with PF127-stabilized PSL was turned into porous carbon monoliths (CMs) through hydrothermal carbonization. The pore formation mechanism, effect of each polymer component, the hydrothermal treatment conditions, and the effect of carbonization temperature were investigated to understand this method of forming porous carbon from natural nanofibers. CMs were then tested as oil adsorbents in an oil-water dispersion.

1.2. Experimental Section

1.2.1. Materials

The list of reagents used are as follows: cellulose powder $(C_6H_{10}O_5)_n$ from Nacalai Tesque, NaBr from Sigma-Aldrich, (2,2,6,6-Tetramethylpiperidin-1-yl)oxyl or TEMPO ($C_9H_{18}NO$) from Tokyo Chemical Industry, 8.5~13.5 % NaClO from Nacalai Tesque, sodium dodecyl sulfate or SDS ($NaC_{12}H_{25}SO_4$) from Wako Pure Chemical Corporation, 0.5 M sodium hydroxide solution (NaOH) from Sigma-Aldrich, styrene monomer (C_8H_8) from Nacalai Tesque distilled once under low vacuum, ammonium persulfate or APS ($(NH_4)_2S_2O_8$) from Sigma-Aldrich, Pluronic F-127 from Sigma-Aldrich, activated carbon pellets from Wako Pure Chemical Corporation, tetrachloroethylene (C_2Cl_4) from Tokyo Chemical Industry, octanoic acid ($C_7H_{15}COOH$) from Nacalai Tesque, and isooctane (C_8H_{18}) from Nacalai Tesque. Except for styrene, all other reagents were reagent grade, and used as received.

1.2.2. Synthesis of TEMPO-oxidized Cellulose Nanofibers (TOCN)

Cellulose (4.0 g), NaBr (0.768 g), and TEMPO (0.075 g) were added to water (300 mL) and stirred for 1h until homogeneous. NaClO (18 mL of 8.5~13.5 % solution) was then added dropwise. The mixture was stirred overnight while maintaining the pH at 10.5 using an autotitrator with 0.5 M NaOH to maintain excess ^-OH as oxygen source for oxidation. When the reaction is complete indicated by the color change from yellow to white, the cellulose pulp

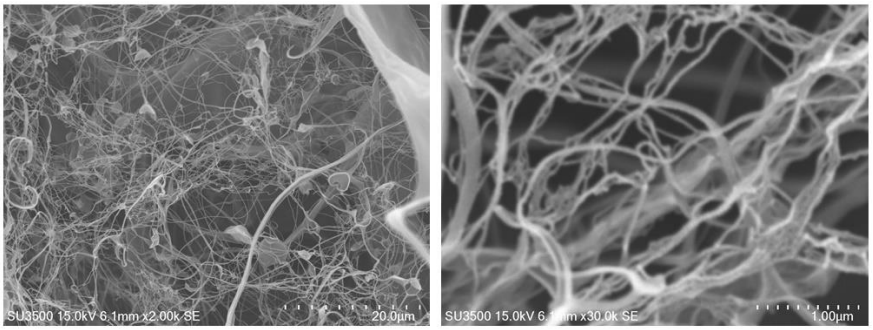

Figure 1-1. SEM micrographs of TOCN.

was separated from the liquid via centrifugation at 4000 rpm. The white pulp re-dispersed in 40 mL water, then centrifuged again at 4000 rpm. The process of redispersion and centrifugation was repeated 4 times to clean the pulp. The purified cellulose was then diluted with water to around 1 wt%, then fibrillated using a blender for 0.5 h. An average size of 53±15 nm was calculated from scanning electron microscopy (SEM) images of TOCN (**Figure 1-1**).

1.2.3. Synthesis of Polystyrene Latex (PSL)

SDS (1.5 g) was dissolved in water (258 mL), then styrene (30 mL) was added dropwise. APS (0.01 g) dissolved in water (12 mL) was added and stirred, then the reaction flask was purged with $N_{2(g)}$ for 0.5 h. The reaction flask was then placed in a 70°C water bath and stirred for 3h. The PSL was placed in a 50 kDa dialysis tube, and dialyzed for 5 days with regular water changes until no trace of styrene monomer was detected. The PSL diameter was found to be at 66 ± 55 nm using dynamic light scattering (DLS) analysis (**Figure 1-2**).

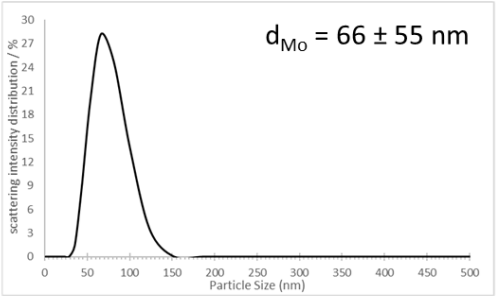

Figure 1-2. DLS spectra of PSL.

1.2.4. Synthesis of Porous Carbon Monoliths (PCM)

TOCN dispersion (10 g of the 1 wt%, corresponding to 0.1 g dry TOCN), PSL, Pluronic F-127 (PF 127), and water for a total volume of 12.8 mL was mixed for 1 h until homogeneous. The viscous mixture was then transferred to a hydrothermal reaction vessel and placed in an oven for 48 h. The flask was cooled to room temperature, then the resulting solid called the hydrochar monolith (HM) was separated from the supernatant. HM was washed with EtOH 3 times and then with water for another 3 times. The hydrochar was then freeze-dried for 48 h. The dried hydrochar was placed in a furnace under $Ar_{(g)}$ atmosphere with a constant flow rate of 75 mL min^{-1}. The temperature was raised with a heating rate of 5°C min^{-1} to a temperature T_{hold}, maintained for 2 h, then allowed to cool down overnight. The final product was a carbon monolith (CM) The list of experiments performed and their corresponding conditions are listed in **Table 1-1**.

Table 1-1. List of samples. Samples after HTT are labelled as HM-XXX, and samples after carbonization are labelled CM-XXX, where XXX is the code listed below.

Code	PSL / g	PF 127 / g	HTT temp /°C	T_{hold} /°C
Variation of PSL content				
S1	0.016	0.010	180	500
S2	0.032	0.010	180	500
S5	0.080	0.010	180	500
S10	0.160	0.010	180	500
Variation of PF 127 content				
F1 (=S5)	0.080	0.010	180	500
F2	0.080	0.020	180	500
F5 (=H180, C500)	0.080	0.050	180	500
F10	0.080	0.100	180	500
Removal of polymer components for determining structure formation				
SxF1	-	0.010	180	500
SxF5	-	0.050	180	500
S5Fx	0.08	-	180	500
Variation of HTT temperature				
H180 (=F5, C500)	0.080	0.050	180	500
H200	0.080	0.050	200	500
Variation of carbonization temperature (T_{hold})				
500c (=F5, H180)	0.080	0.050	180	500
600c	0.080	0.050	180	600
700c	0.080	0.050	180	700
800c	0.080	0.050	180	800
900c	0.080	0.050	180	900

1.2.5. Characterization

Field Emission Scanning Electron Microscopy (FESEM) micrographs were taken from a JEOL JSM-6700F microscope. Scanning Electron Microscopy (SEM) micrographs were obtained using a Hitachi SU3500 microscope. Infrared Spectroscopy (IR) spectra were taken by a Nicolet iS5 Attenuated Total Reflectance spectrometer. IR spectra taken using the KBr pellet method used a Jasco FT/IR-4100 infrared spectrometer. Thermogravimetric Analysis (TGA) was measured using a SII TG/DTA7200 instrument. Dynamic Light Scattering (DLS) spectra were taken by an Otsuka ELSZ-2000 Particle size Analyzer. Brunauer-Emmett-Teller Surface Area Analysis (BET) was taken from a Quantachrome NOVA 4200e Surface Area and Pore Size Analyzer. All samples were dried in vacuum at 70 °C for 24 h before BET analysis. X-ray photoelectron spectroscopy (XPS) spectra were taken by a JEOL JPS-9010MC XPS instrument with monochromatic AlKα-radiation. CasaXPS Version 2.3.15 was used for analyzing the C1s narrow XPS profile. The water contact angle was controlled to drop 1µm water by DropMaster DM 300. FAMAS was used to analyze the water contact angle images.

1.2.6. Adsorption Experiments

The adsorption adsorbate, calibration, extraction, and analysis were based on the oil and grease determination method through mid-infrared method[6]. All adsorption experiments were conducted in 50 mL silicone-sealed brown borosilicate glass to prevent oxidation and contamination. 50 mL of 5 mg mL^{-1} mixture of 1:1 octanoic acid and isooctane dispersed in water was stirred at 150 rpm for 0.5 h then a CM of 0.02 g was placed inside. The CM was removed after 120 min, then the remaining oil was extracted using C_2Cl_4. The extract was diluted then analyzed using a Jasco FT/IR-4100 spectrometer at 2933.2 cm^{-1}. The FTIR conditions were set at a of resolution 8 cm^{-1}, 64 scans, quartz cell with path length of 10 mm

(**Figure 1-3**). Comparative studies of the synthesized monoliths with commercially available activated carbon pellets were also performed using the same conditions.

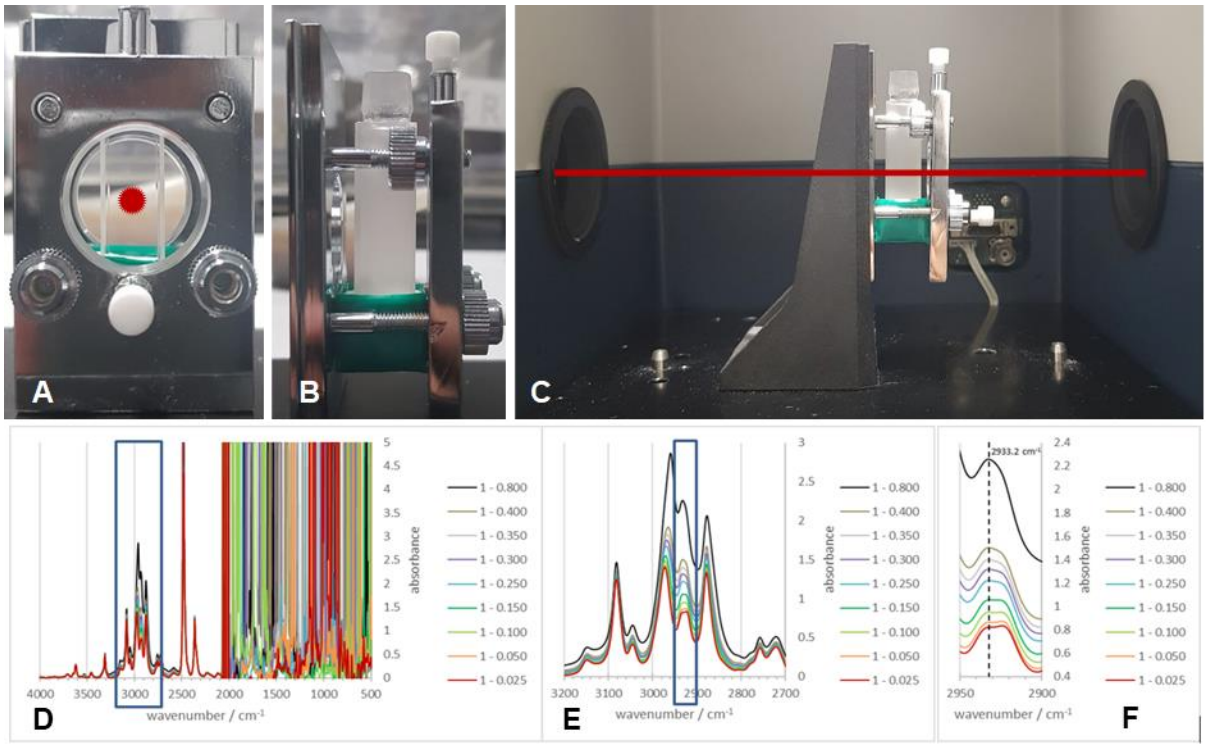

Figure 1-3. Liquid IR setup. Images of the setup of the glass cell in the FTIR chamber: A) front view, B) side view, C) entire chamber setup. The green handle at the bottom of the cuvette is made of foam to prevent contact of the cuvette with the metal, avoiding breakage of the cuvette. The IR beam is at the center of the circular cutout, and the foam holder does not interfere with the beam (red). IR spectra of the calibration curve standards: D) 4000-400 cm^{-1}, E) 3200-2700 cm^{-1}, F) 2950-2900 cm^{-1}.

1.3. Results and Discussion

1.3.1. Effect of Polystyrene Latex

PSL is the primary template in the system that is removed upon carbonization, forming pores arranged neatly in a honeycomb pattern on the surface of the CM. The maximum amount of PSL that can be loaded into the TOCN matrix before structural failure was investigated. SEM

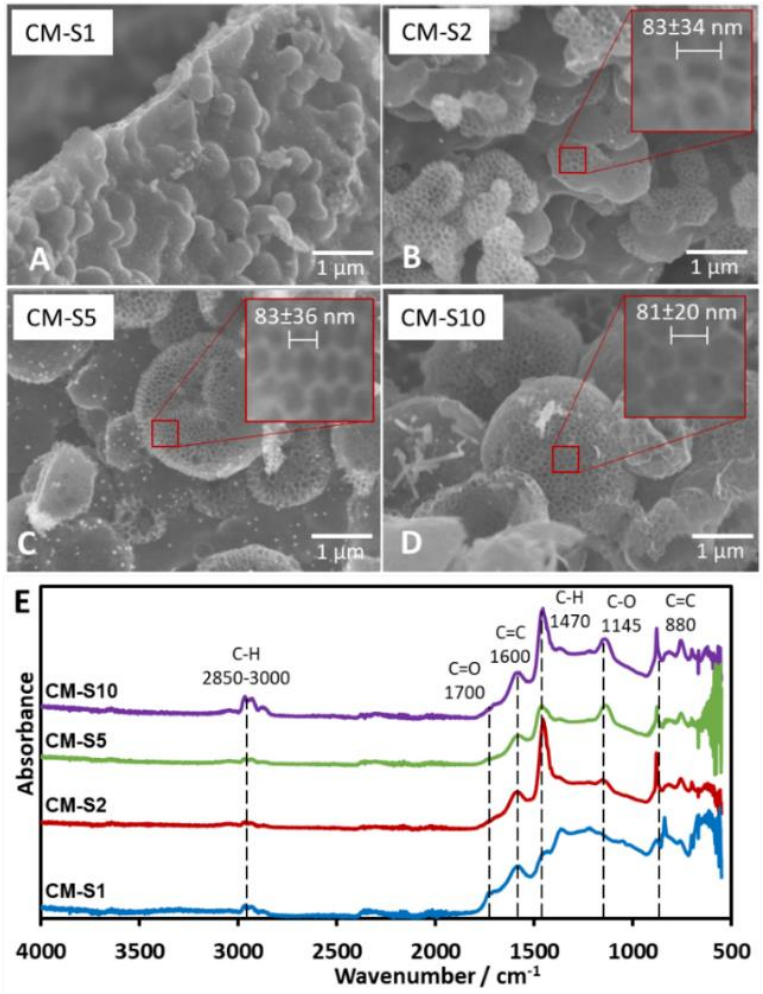

Figure 1-4. A-D) SEM images of carbon monoliths with increasing amounts of PSL CM-S1 to CM-S10, E) IR spectra of CM-S1 to CM-S10.

images (**Figure 1-4**) reveal that the minimum amount of PSL required for significant pore formation starts at 32 mg (CM-S2). Pore formation on the surface of CM-S1 is not observed.

Too much PSL resulted in a less stable structure as seen in CM-S10 due to the TOCN matrix being spread too thin among the template particles, leading to weaker carbon walls (**Figure 1-4**D). It is also notable that pores with diameter in multiples of the PS particle diameter (nd, n = 2, 3, …, d is the diameter of the PS particle) is not observed, indicating that PSL is stable in the system, does not aggregate, forms uniform pores on the surface of the material, and shows a consistent pore size of around 80 nm (**Figure 1-4**A-D), slightly larger than the PSL

template. Above the lower critical concentration of PSL, the amount of PSL does not affect the final pore size after carbonization. The absence of PSL in the system results to CM without 80 nm pores. From the IR spectra (**Figure 1-4**E), the samples are predicted to be composed almost purely of carbon and oxygen, due to the presence of possible C=C (stretching at 1600 cm^{-1}, bending at 880 cm^{-1}), C=O (stretching at 1700 cm^{-1}), and C-O (stretching at 1145 cm^{-1}), with little C-H present (stretching at 2850-3000 cm^{-1}, bending at 1470 cm^{-1}).

1.3.2. Effect of Pluronic F-127

It has been reported by Kubo et al. that the concentration of PF 127 has an effect on the macrostructure of the CM by inducing variations in the channels within the material through the thickening of the so-called branches of the bulk material[5] with glucose. However, using TOCN resulted to a different interaction between TOCN, PF 127, and PSL. PF 127 has an effect during HTT by stabilizing the interface between TOCN and PSL to allow PSL-based templating. PF 127 is also reported to form micelles[7] that could form the cavities several micrometers across.[5,8] Other studies using starch[9] and glucose[10] have reported distinct carbon spheres[11,12], while a study by Zhu et al.[13] reported organic self-assembly of mesoporous carbon spheres from the formation of PF 127 micelles that act as a core for the hydrochar shell during HTT. A similar phenomenon is observed in this study and is confirmed for PF 127 forming micelles 1 µm across (**Figure 1-5**A) that then turn to hollow carbon spheres wherein the carbon shell is dotted with 80 nm pores. To confirm that the micelles are not PSL aggregates, monoliths with 10 to 50 mg PF 127 but with no PSL (CM-SxF1, CM-SxF5 respectively) were synthesized. An increase in the number of 1 µm- sized spheres was observed (**Figure 1-6**A). The templating effect of PF 127 also occurs during HTT, and the structure is preserved after carbonization. In this research, the prevalence of fusion of the carbon spheres to form a

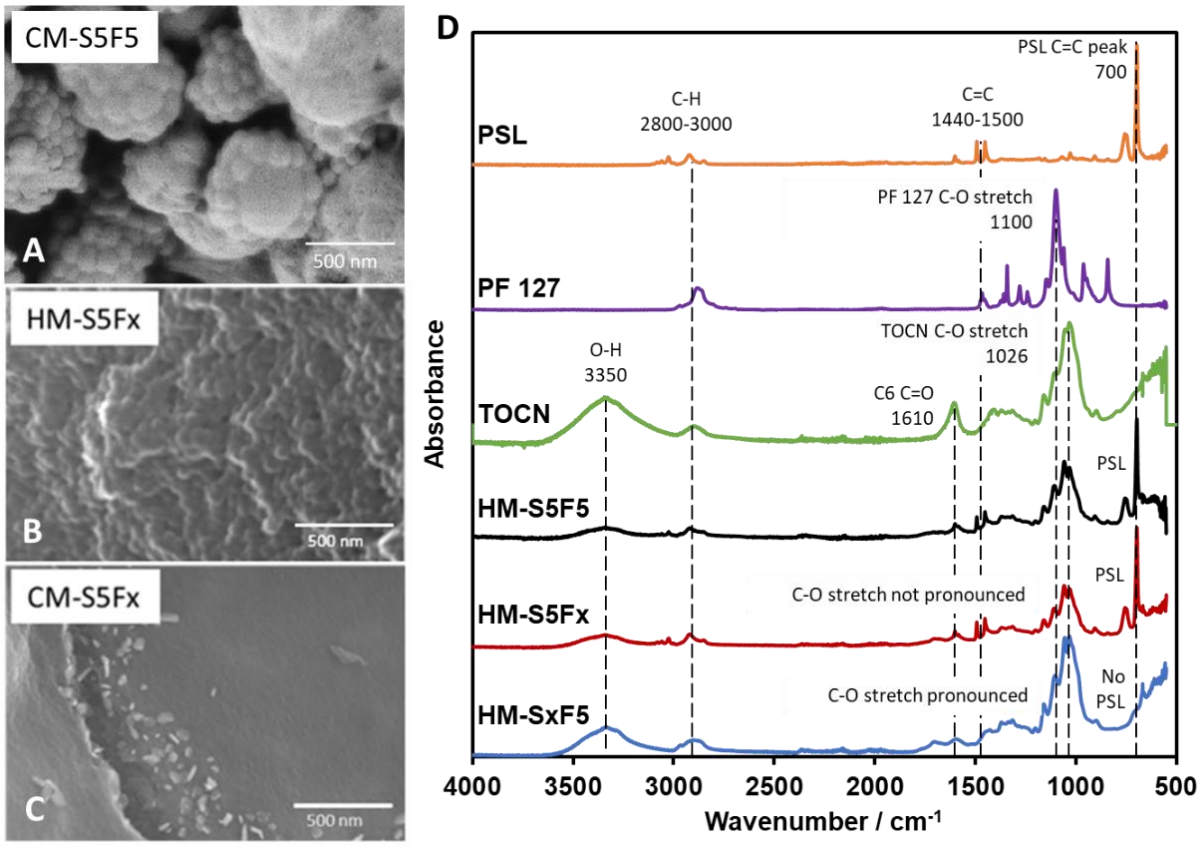

Figure 1-5. A) FESEM image of HM-S5F5 showing the inner PF 127 micelle. B) SEM image of hydrochar without PF 127 added (HM-S5Fx). C) SEM image of HM-S5Fx after furnace treatment (CM-S5Fx). D) IR spectra of the polymer components (PSL, PF 127, TOCN), and hydrochars (HM-S5F5, HM-S5Fx, HM-SxF5).

monolith, unlike other structures (branched[5], distinct spheres[11,12]) is likely due to TOCN fibers entangling and/or one fiber is embedded in adjacent spheres. When PF 127 is not added, HM-S5Fx did not have the 1 µm spheres (**Figure 1-5**B), and after carbonization (**Figure 1-5**C) even the 80 nm pores were absent in CM-S5Fx, showing that the presence of PF 127 as the interface between PSL and TOCN also extends to the pore formation during carbonization. The formation of monoliths even without PSL (CM-S5Fx, **Figure 1-5**C) or PF 127 (CM-SxF5, **Figure 1-6**B) indicates that PF 127 and PSL are not the main nucleating agents in the system. TOCN through fiber entanglement, crosslinking, and hydrothermal degradation aggregates into

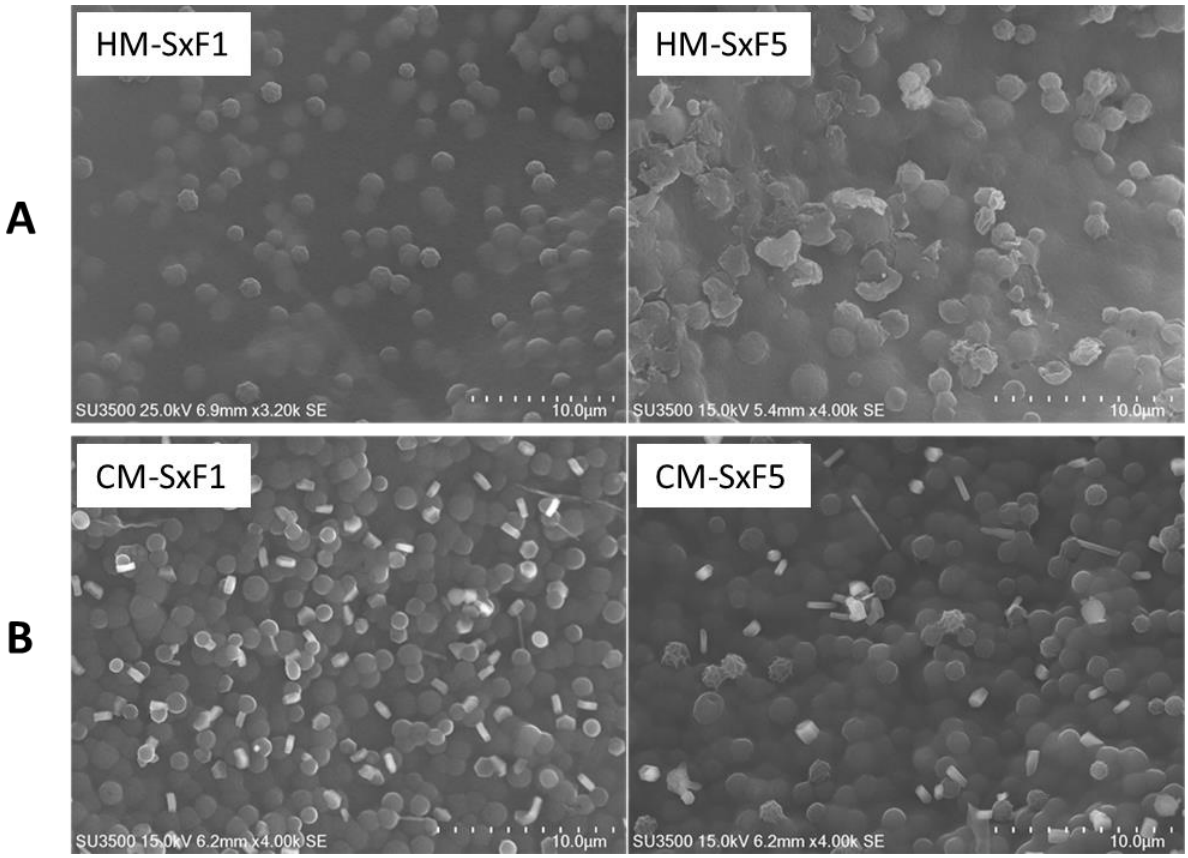

Figure 1-6. SEM images of monoliths with no PSL and varied PF 127 content: A) hydrochar of HM-SxF1 and HM-SxF5, and B) carbon monolith of CM-Sx-F1 and CM-SxF5.

a monolith during HTT. IR spectra of HM (**Figure 1-5**D) shows that PF 127 and the C6 carboxy group of TOCN are preserved even after HTT with the pronounced C-O stretch at the 1050-1100 cm^{-1} region, and the presence of a C=O peak at the 1700 cm^{-1} respectively. PSL is also intact, just coated with the TOCN nanofibers that turned to hydrochar (**Figure 1-7**A). The amount of PF 127 changes the apparent macroporosity of the material, as well as the density of the unique 1µm spheres covered in PSL. The amount of PF 127, shown from samples HM-F1 to HM-F10 affect the density and the uniformity of the spherical shape of the 1 µm spheres, but at 200 mg (HM-F20) too much PF 127 will contribute a significant mass and volume to the hydrochar matrix, covering the structures formed with PSL. After carbonization (**Figure 1-7**B) CM-F1 and CM-F5 exhibited the hollow spheres with a honeycomb surface, while CM-F10 did

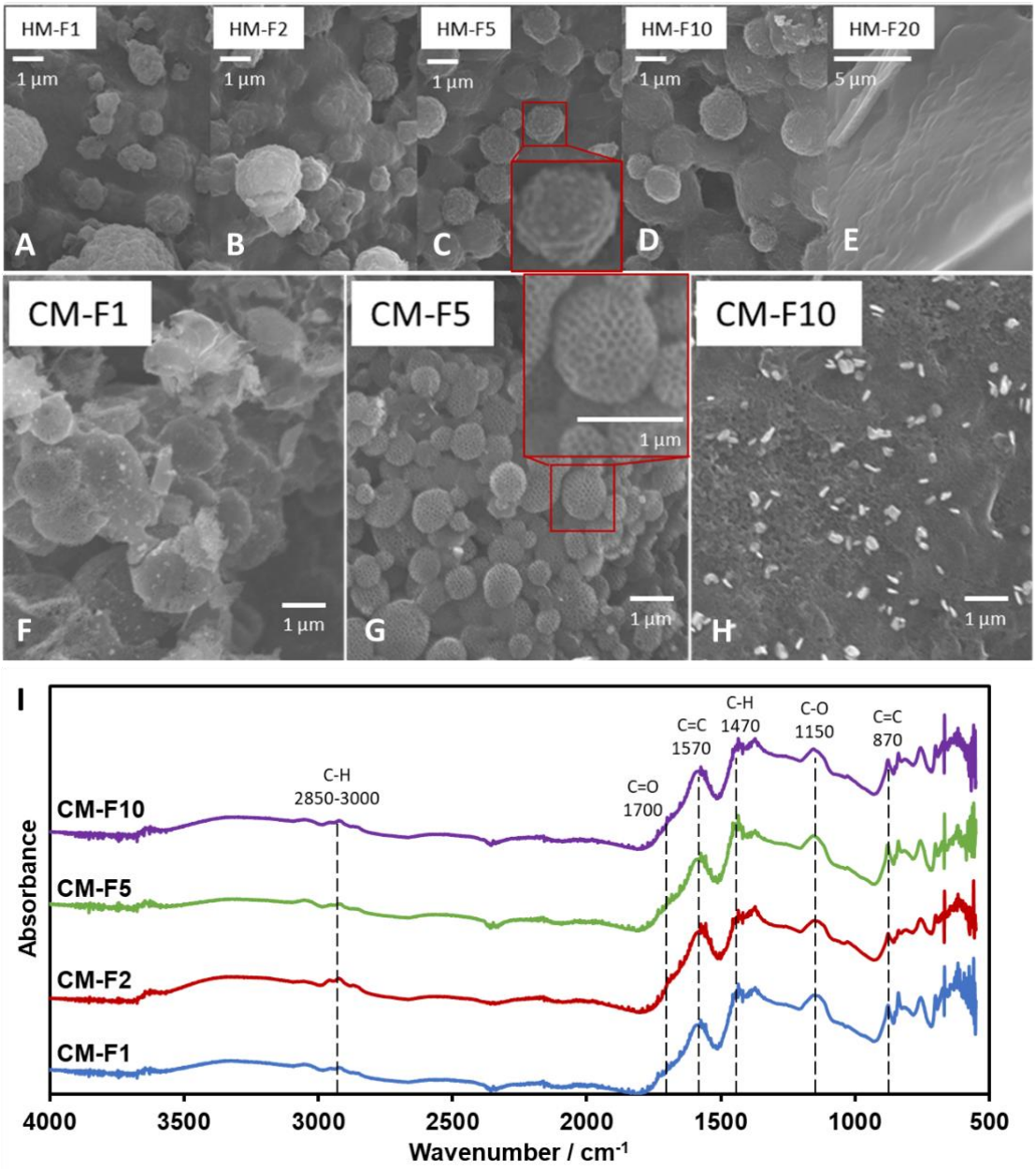

Figure 1-7. A-E) SEM images of HM with increasing PF 127 content. F-H) SEM images of CM with increasing PF 127 content. I) IR spectra of CM with increasing PF 127 content.

not, indicating that 100 mg is also too much PF 127, which could be from 1) high gas evolution rate affecting structure stability, and 2) significant amounts of PF 127 leading to carbon contribution to the monolith, altering the structure made with carbon only from TOCN. The IR spectra (**Figure 1-7**I) shows similar peaks as that of samples with increasing PSL content, indicating that PF 127 and PSL both do not significant affect the final functional groups present

in the carbon monolith. Peaks for C=C bending at 870 cm^{-1}, stretching at 1570 cm^{-1}, C=O stretching at 1700 cm^{-1}, and ether C-O stretching 1150 cm^{-1} point out highly unsaturated carbon oxidized with oxygen. Little C-H is also observed with stretching at 2850-3000 cm^{-1}, and bending at 1470 cm^{-1}.

1.3.3. Effect of Hydrothermal Treatment

From **Figure 1-8**A, it can be observed that HTT when using TOCN has 3 phases: 1) dehydration and heat-induced crosslinking, 2) degradation of polymers into organic compounds such as 5-HMF and phenols and 3) repolymerization, monolith formation, and water release. At 0.5 h, degradation indicated by color change has not yet occurred. A stable monolith was

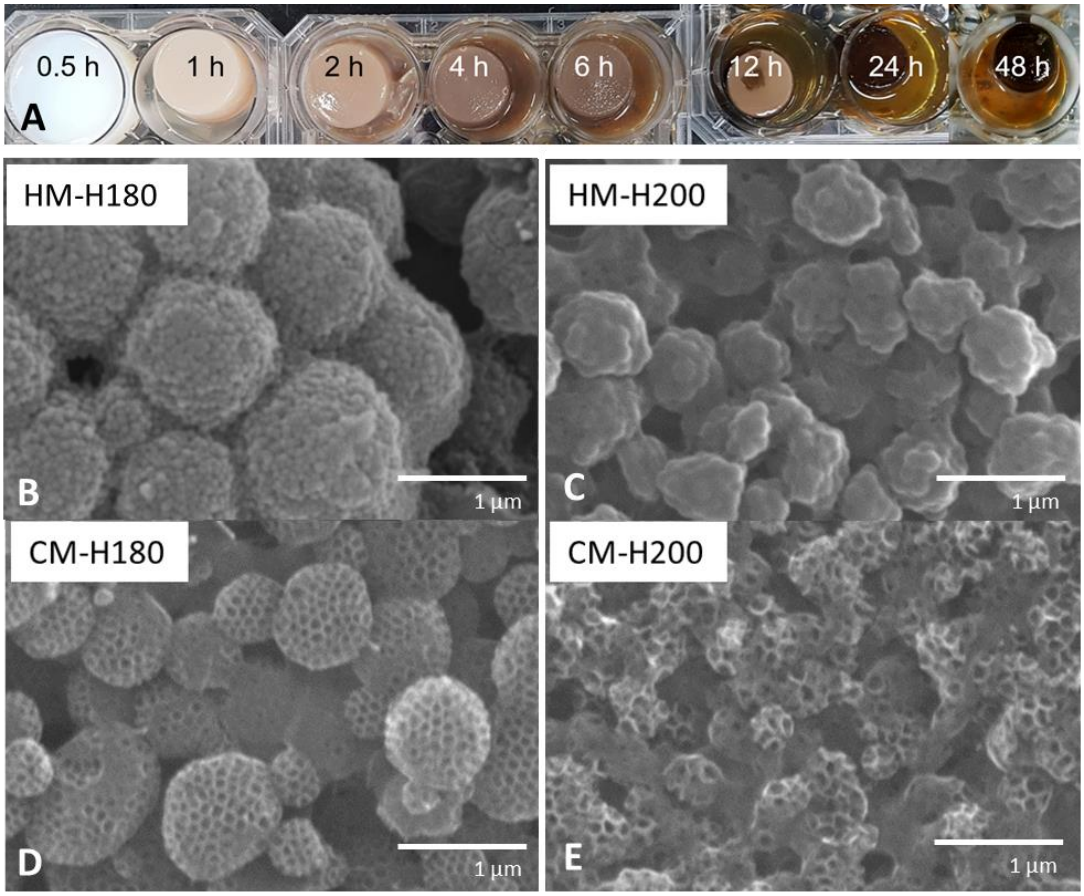

Figure 1-8. A) Images of the monolith formed after varying HTT time. B-C) SEM images of monolith formed with HTT at 180 °C (HM-H180) and 200 °C (HM-H200). a. D-E) SEM images of monolith formed at 180 °C (CM-H180) and 200 °C (CM-H200).

formed by 1 h, indicating that there is sufficient crosslinking *via* esterification or H-bonding to hold the polymer components in place. Phase 2 occurs as degradation of the polymers as the hydrochar turns darker at 2 h, but not all of the organic compounds and PSL have repolymerized back into the hydrochar at 6 h as indicted by the cloudy supernatant. By 12 h, Phase 1 and 2 are complete, and development of Phase 3 continues from 12-48 h when the water becomes clearer, and sufficient water has been removed from the monolith. Because Phase 3 only starts from 12 h, the optimal time will be when Phase 3 has occurred long enough to accumulate majority of the mass from the reagents to get high yield. Only at 48 h did the supernatant become transparent, and thus was considered as the optimal reaction time. Investigating the effect of increasing HTT temperature revealed that increasing the temperature from 180 ^{o}C (HM-H180) to 200 °C (HM-H200) affected the size of the PF 127-based sphere from 1 μm to 500 nm (**Figure 1-8**B, C). It is suggested that polymers that nucleate to form spheres under HTT can be described by the La Mer Nucleation Model[14,15]. Except for the change in size, the structure remains the same, suggesting the same process occurs at both temperatures. Carbonizing the monoliths at 500 °C formed the same type of structure as well, but cavities between spheres of CM-H200 are smaller than that of CM-H180.

1.3.4. Effect of Carbonization Temperature

Replication of furnace conditions in TGA (**Figure 1-9**) show that hydrochar mass loss occurs at two distinct temperatures: 201 °C and 295 °C. The peak at 201 °C corresponds to acid-catalyzed dehydration described as pre-pyrolysis, while 295°C refers to the complete loss of crystallinity and actual decomposition also called the main pyrolysis[16]. The main pyrolysis step of hydrochars is 19 °C lower than pure TOCN, indicating lower crystallinity of remaining cellulosic chains. The PF 127 degradation peak at 378 °C does not change with the hydrochar, indicating that PF 127 does not chemically change during HTT. PSL dispersed in the monolith

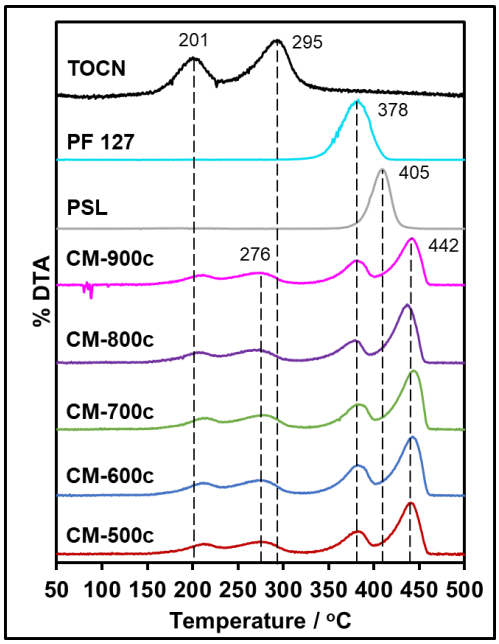

Figure 1-9. First derivative of the TGA curve (DTA) of CM-500c to CM-900c, PSL, PF 127, and HM-TOCN. No peaks observed above 450 °C, indicating no mass loss.

has a higher degradation temperature of 442°C, unlike pure PSL decomposing at 405 °C. PSL could subsequently react to the carbon matrix formed during the main pyrolysis step of the TOCN component, stabilizing PSL.

SEM images at **Figure 1-10** show a similar structure forming for all monoliths, indicating that the structure formed during HTT is not affected by the carbonization step. The surface area (S_{BET}) of CM increases significantly as carbonization temperature increases (**Table 1-2**) from 109 $m^2\ g^{-1}$ at 500 °C to 1534 $m^2\ g^{-1}$ at 800 °C, then remains relatively the same at 900 °C with 1563 $m^2\ g^{-1}$. The same trend is present for $V_{total}\ N_2$ from BJH analysis increasing from 0.396 $cm^3\ g^{-1}$ of CM-500c to 2.1149 $cm^3\ g^{-1}$ of CM-800c, but CM-800c and CM-900c had similar $V_{total}\ N_2$ of 2.149 and 2.129 $cm^3\ g^{-1}$ respectively. All CMs show a hybrid of Type IV H1/H3 BET curves, indicating the abundance of relatively uniform mesopores in the material (**Figure 1-10**). The macro- and mesoporosity of CM is formed *via* templating PSL and PF 127, thus the increase in S_{BET} is due to the increase in microporosity from increased carbonization

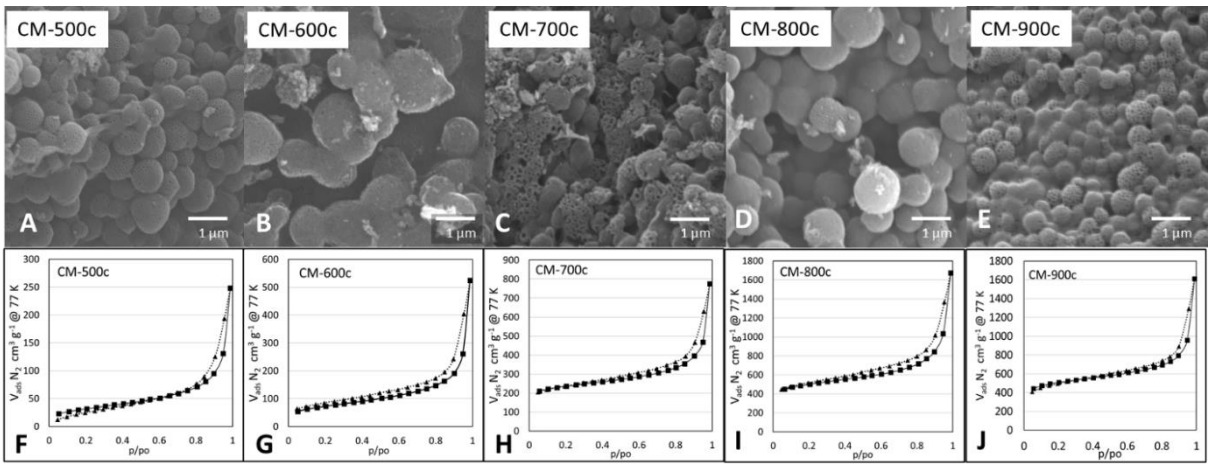

Figure 1-10. SEM images (A-E) and respective BET N_2 adsorption and desorption isotherms (F-J) of monoliths carbonized at increasing T_{hold} from 500-900°C.

Table 1-2. Surface area, product yield, and elemental composition of samples carbonized at different temperatures.

	S_{BET} $m^2\,g^{-1}$	$V_{total}\ N_2$ $cm^3\,g^{-1}$	$V_{meso\text{-}macro}\ N_2$ $cm^3\,g^{-1}$	$V_{micro}\ N_2$ $cm^3\,g^{-1}$	$d_{BJH}\ N_2$ nm	Carbon Yield mass %	XPS O/C ratio
CM-500c	109.57	0.396	0.371 (93.7%)	0.025 (6.3%)	1.517	28.14 ± 3.63	0.261
CM-600c	250.94	0.802	0.753 (93.9%)	0.049 (6.1%)	1.677	29.65 ± 1.67	0.268
CM-700c	722.55	0.995	0.914 (91.8%)	0.082 (8.2%)	1.432	30.36 ± 3.87	0.222
CM-800c	1534.80	2.149	1.979 (92.1%)	0.170 (7.9%)	1.443	30.56 ± 0.76	0.235
CM-900c	1563.34	2.129	1.859 (87.3%)	0.270 (12.7%)	1.433	26.48 ± 1.81	0.216

temperature as shown in the increasing $V_{micro}N_2$ from 6.3 % of CM-500c to 12.7 % of CM-900c. The elemental composition of the monoliths was analyzed via XPS, and showed high O/C ratio observed on all CMs. The O/C values are similar to that of methods that use multi-step activation KOH or H_2O[17,18]. The decreasing O/C ratio points to oxygen loss due to evolution of gases such as CO and CO_2. Despite carbon loss from gases however, the carbon yield by mass stays relatively constant from 26.48-30.56 %. Carbon yield was calculated by dividing the amount of carbon in the monolith by the amount of carbon in the starting TOCN mass. PSL and PF 127 do not contribute significant amounts of carbon to the material during carbonization, and TOCN is assumed to be sole source of carbon in the system.

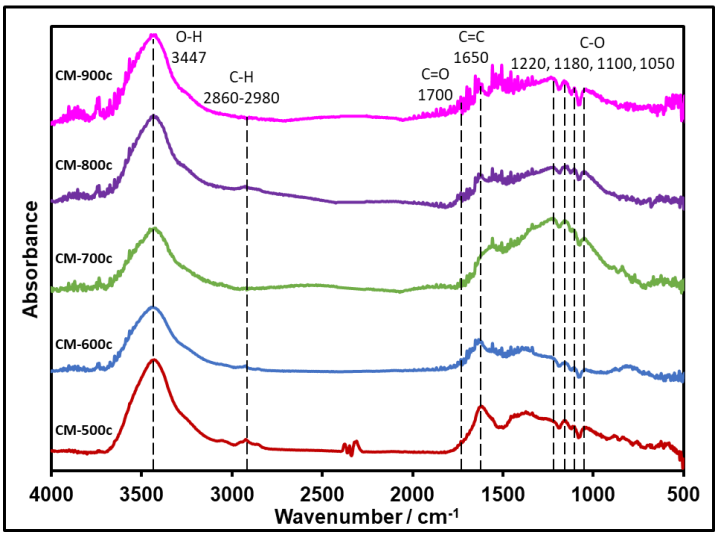

Figure 1-11. IR spectra of CM-500c to CM-900c powdered and immobilized in KBr pellet.

After the decomposition of the PSL and PF 127 templates, the material undergoes further carbonization until it is made of mostly C and O: C-O at the 1220-1050 cm^{-1} region, C=C at 1650 cm^{-1}, and C=O at 1700 cm^{-1} (**Figure 1-11**). While the O-H peak at 3447 cm^{-1} could also be another indicator for O-H groups in the material, differences in mass when the CMs were dried for BET point to adsorption of water vapor to some extent. There is almost no C-H, which is the same as that of CM-S5 (**Figure 1-4**) and CM-F5 (**Figure 1-7**). XPS analysis further confirms the elemental composition showing only peaks of C, O, and Indium (XPS stage). Focusing on the C1s peak shows no clear trend between carbonization temperature and concentrations of the amount of carbon nor the specific oxygen functional groups. The peak at 285.0 eV is known to be graphitic carbon[19], and the amount of graphitic carbon steadily decreases from CM-500c to CM-800c from the inclusion of oxygen in the monolith, then increases again at CM-900c which likely due to the higher loss of oxygen from evolution of gases (**Table 1-3**). C-O in the monolith is resolved in IR as well as XPS. From **Figure 1-11** ester C-O stretching 1220 cm^{-1}, tertiary, secondary, and primary alcohols at 1180, 1100, and 1050 cm^{-1} respectively can be observed. Aliphatic ether C-O peaks are likely merged with the tertiary and secondary alcohol peaks in this region and could not be further resolved. For XPS

the relative amount of C-O is shown to be increasing from 15.36 % for CM-500c then stabilizing at around 20 % for samples CM-600c, CM-700c, and CM-900c. CM-800c had an unnaturally high C-O percent which is likely C-O and C=O being unresolved. CM-900c had an additional peak at 293.0 eV which is most likely a π-π* interaction similar to that observed at 950°C from Yu et. Al[20]. It should be noted that for **Figure 1-11**, the IR spectra was taken using the KBr pellet method instead of ATR due to low peak intensity observed for CM-700c, CM-800c, and CM-900c. CM-500c and CM-600c could be analyzed using ATR, but CM-500c and CM-600c were analyzed using the KBr pellet method as well for data consistency.

1.3.5. Oil-Water Separation Performance

The synthesized honeycomb-like pore geometry is useful in increasing the packing density of mesopores and macropores of the carbon surface, increasing multi-modality. This hierarchical pore structure helps in water penetration, increasing contact in the bulk of the monolith, and subsequently enhancing performance for batch adsorption applications. a fossil fuel standard of octanoic acid and isooctane based on an oil and grease content in water determination method[6] was used to evaluate the adsorption capacity (q_e) of the monolith. q_e of 9.6 to 11.3 g g^{-1} were observed, with CM-500c having the highest adsorption capacity (**Table 1-4**). the theoretical maximum adsorption capacity is 12.922 g g^{-1} (total amount of oil in oil-water mixture divided by 0.02 g carbon), thus CM-500c has an experimental capacity efficiency of 90.31 %. The effect of carbonization temperature vs. adsorption capacity has a peculiar trend where q_e decreases as the carbonization temperature increases from 500 to 700 °C, but q_e increases from 700 to 900 °C.

For porous materials the mechanism for organic phase adsorption changes whether it is the exterior or the interior of the bulk material. Electrostatic interaction in the interface of the carbon, and water allowing for the adsorption of micellar particles occurs at the exterior surface

Table 1-3. XPS data of samples CM-500c to CM-900c.

	C 1s				O 1s			
	C at%	Group	B.E eV	Conc. %	O at%	Group	B.E eV	Conc. %
CM-500c	79.29	Graphitic C	285.0	71.53	20.71	C=O	531.5	64.10
		C-O	287.0	15.36		O-C=O	533.2	35.90
		C=O	288.9	4.55				
		O-C=O	290.9	8.56				
CM-600c	78.85	Graphitic C	284.9	61.55	21.15	C-O	532.2	100.00
		C-O	286.7	20.43				
		C=O	288.2	6.92				
		O-C=O	290.5	11.10				
CM-700c	81.86	Graphitic C	285.0	64.22	18.14	C-O	532.0	100.00
		C-O	286.8	19.15				
		C=O	288.4	6.45				
		O-C=O	290.6	10.18				
CM-800c	80.98	Graphitic C	284.9	45.28	19.02	C-O	532.2	80.96
		C-O	286.1	45.09		Adsorbed H_2O	534.6	10.61
		O-C=O	290.3	9.63		C=O	530.2	8.43
CM-900c	82.25	Graphitic C	284.5	59.52	17.75	C-O	532.0	94.35
		C-O	286.5	19.72		C=O	529.7	5.65
		C=O	288.1	9.02				
		O-C=O	290.5	8.39				
		plasmon loss	293.0	3.34				

Table 1-4. Carbonization temperature vs adsorption performance at 5 mg/mL.

Temp	Ave q_e g g^{-1}	Water contact angle
500°C	11.3 ± 0.9	98.3° ± 1.4
600°C	9.9 ± 1.7	113.0° ± 5.5
700°C	9.6 ± 0.8	121.5° ± 4.0
800°C	10.3 ± 0.2	103.7° ± 4.7
900°C	10.7 ± 0.1	101.7° ± 2.2

of the monolith. There is a clear decrease in the O/C ratio between 600 °C and 700 °C. The hydrophobicity of the material increases with increasing carbonization temperature, which explains that even with low surface area, CM-500c has a very high q_e resulting from lower surface tension between the monolith and water. Water contact angle can be used as a rough indicator of hydrophobicity for bulk materials[21], and the inverse trend of increasing then decreasing hydrophobicity is observed (**Table 1-4**). The rugged surface of the monolith further increases the surface area, increasing exterior adsorptive capacity. The interior however is usually inaccessible due to trapped air, and in general the smaller the pores, the more time it

takes for water to replace air in the monolith due to high surface tension[22], leading to a decrease in the effective adsorptive surface of the monolith. The hierarchical porous nature of the monolith, namely the macropores, however makes the monolith take in water relatively easier, as observed with the mass of the monolith after oil adsorption (ave. 0.59 g) far heavier than the dry monolith (ave. 0.02 g) and the theoretical maximum of oil (0.26 g) combined. Given that the macropores are due to the templating from the PSL, the degree of macroporosity for all the monoliths are relatively similar. It is also known that the observed increase in surface area is due to increased microporosity formed during higher carbonization temperature, increasing the adsorption capacity as observed for CM-900c. A similar method of inducing small spaces within the carbon structure increasing adsorption capacity has been reported but in using expanded graphite to increase adsorption capacity[23]. Even though a less significant factor compared to hydrophobicity, higher surface area allows CM-900c to have a high q_e.

The adsorption kinetics of the monolith with the highest q_e (CM-500c) was investigated (**Figure 1-12**). CM-500c shows rapid adsorption reaching 65.4 % removal in 5 min, and maximum removal reached was 81.15 % with q_e of 11.3 after 2 h (**Figure 1-12**A). The q_e changed by 1.4 % after 24 h 11.4g g^{-1}, indicating that adsorption equilibrium as already achieved by 2 h. Pseudo-first order (PFO) and pseudo-second order (PSO)[24,25] are the

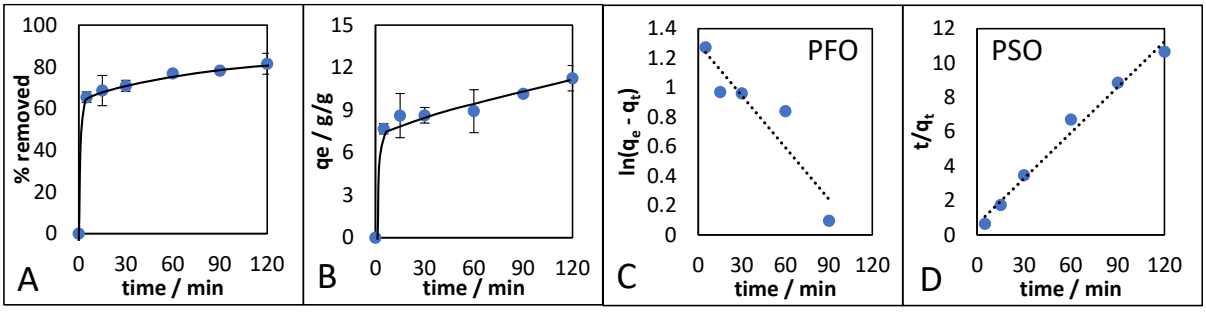

Figure 1-12. CM-500c adsorption kinetic studies. A) Percent removal of octanoic acid and isooctane with increasing time, B) q_e over time, C) pseudo-first order model (PFO), and D) pseudo-second order model.

Table 1-5. Adsorption kinetic parameters from CM-500 at 298 K.

	$q_{e,\ exp}$ (g g^{-1})	k (g g^{-1} min^{-1})	$q_{e,\ calc}$ (g g^{-1})	R^2
Pseudo-first order (PFO)	11.2554	0.0117	3.6594	0.8622
Pseudo-second order (PSO)	11.2554	0.0124	11.2986	0.9842

empirical kinetic models that give the rate of the adsorption. For PFO, the plot of $\ln(q_e - q_t)$ vs t (**Figure 1-12**C) where q_e is the adsorption capacity in equilibrium (g g^{-1}), q_t is the adsorption capacity at a given time (g g^{-1}), k_{PFO} is the rate of adsorption calculated from PFO (g g^{-1} min^{-1}), and t is time in min, shows poor correlation, and likewise a different calculated adsorption capacity at equilibrium ($q_{e,\ cal}$) of 3.6450 compared to the theoretical adsorption capacity at equilibrium ($q_{e,\ exp}$) at 11.2554. Using the PSO model on the other hand gave very good correlation of R^2 = 0.9842 and comparable $q_{e,\ exp}$ = 11.2986 g g^{-1} (**Table 1-5**). The rate of adsorption from PSO (k_{PSO}) is similar to k_{PFO}, showing agreement with the general adsorption rate performance of CM-500c. Possible physical interpretations of PFO and PSO were elucidated[25-27], and two of the conditions where a general kinetic model becomes PFO or PSO are based on 1) the active sites of the adsorbent as the rate-limiting step – ie. a function of the affinity of the adsorbate to the adsorbent, and the 2) the number of active sites of the adsorbent. Hydrophobic adsorbates with hydrophobic adsorbents are better represented by PSO, reflecting a high number of active sites or sites of adsorption in the monolith. Further studies on the adsorption kinetics of the material are needed to elucidate effect of surface functionalization on adsorption.

Lastly CM-500c was compared to commercially available activated carbon pellets using the same adsorption experiment method. The O/C ratio is comparable at 0.247 with 5.36 % difference from CM-500c. S_{BET} is much higher at 912.83 m^2 g^{-1} which is due to the high amount of micropores, comprising 72.8 % of V_{total} N_2. Despite the high S_{BET} and the abundance of micropores, the commercially available activated carbon pellets fared worse than the monolith

at 8.8 gg^{-1} (60.69 % removed), indicating that the unique porous structure formed from PS templating is highly influential to the adsorption of adsorbates into the bulk of the carbon monolith, thereby resulting to an increase in performance.

1.4. Conclusions

A carbon monolith comprised of fused hollow spheres with an open skeletal pore structure resembling a honeycomb pattern was synthesized using TEMPO-oxidized cellulose nanofibers as the carbon source. The structure formed only during HTT, which does not change during carbonization. The increase in surface area is from the increased microporosity from the high carbonization temperature, notably from 700-900 °C. While PSL is responsible for the formation of the honeycomb pattern on the surface of the spheres, the integrity of the structure as well as the template for the larger fused spheres is due to the presence of PF 127 acting as an interface, and as a precipitate micelle embedded in the TOCN matrix respectively. The hierarchical and open porous network observed is deemed good for adsorption of hydrophobic liquids due to the high carbon content and low XPS O/C ratio, thus used for oil-water separation. Using carbonization temperature-induced changes in surface area and hydrophobicity, CM-500c to CM-900c were tested for oil adsorption and was found that CM-500c had the highest adsorption capacity of 11.3 g g^{-1}, next to CM-900c of 10.7 g g^{-1}. Combining the multiple methods of optimizing structure and hydrophobicity through hydrothermal carbonization as well as templating from PSL and PF 127 resulted in a very high adsorption capacity of the carbon monolith.

1.5. References

[1] S. Sabir, *Crit. Rev. Environ. Sci. Technol.* **2015**, *45*, 1916–1945.
[2] A. Isogai, T. Saito, H. Fukuzumi, *Nanoscale* **2011**, *3*, 71–85.
[3] T. Kurort, Y. Sekiguchi, T. Ogawa, T. Sawaguchi, T. Ikemusa, T. Honda, *Nippon Kagaku Kaishi* **1977**, *1977*, 894–901.
[4] I. H. Harding, *Colloid Polym. Sci.* **1985**, *263*, 58–66.
[5] S. Kubo, R. J. White, K. Tauer, M.-M. Titirici, *Chem. Mater.* **2013**, *25*, 4781–4790.
[6] A. Pisal, *Determination of Oil and Grease in Water with a Mid-Infrared Spectrometer*, **2010**.
[7] P. Linse, M. Malmsten, *Macromolecules* **1992**, *25*, 5434–5439.
[8] S. Kubo, R. J. White, N. Yoshizawa, M. Antonietti, M.-M. Titirici, *Chem. Mater.* **2011**, *23*, 4882–4885.
[9] X. Lu, C. Jiang, Y. Hu, H. Zhong, Y. Zhao, X. Xu, H. Liu, *J. Appl. Electrochem.* **2018**, *48*, 233–241.
[10] X. Du, S. Ma, W. Zhao, Z. Zheng, T. Qi, Y. Wang, *J. Nanosci. Nanotechnol.* **2017**, *17*, 3835–3841.
[11] X. Sun, Y. Li, *Angew. Chemie - Int. Ed.* **2004**, *43*, 597–601.
[12] Q. Wu, W. Li, J. Tan, S. Liu, *RSC Adv.* **2014**, *4*, 61518–61524.
[13] X. Zhu, S. Wang, W. Huang, Y. Tian, X. Wang, *Carbon N. Y.* **2016**, *105*, 521–528.
[14] M. Sevilla, A. B. Fuertes, *Chem. - A Eur. J.* **2009**, *15*, 4195–4203.
[15] V. K. La Mer, *Ind. Eng. Chem.* **1952**, *44*, 1270–1277.
[16] F. D'Acierno, W. Y. Hamad, C. A. Michal, M. J. Maclachlan, *Biomacromolecules* **2020**, *21*, 3374–3386.
[17] Q. Abbas, M. Mirzaeian, A. A. Ogwu, M. Mazur, D. Gibson, *Int. J. Hydrogen Energy* **2020**, *45*, 13586–13595.
[18] M. Genovese, H. Wu, A. Virya, J. Li, P. Shen, K. Lian, *Electrochim. Acta* **2018**, *273*, 392–401.
[19] M. M. Titirici, A. Thomas, S. H. Yu, J. O. Müller, M. Antonietti, *Chem. Mater.* **2007**, *19*, 4205–4212.
[20] L. Yu, C. Falco, J. Weber, R. J. White, J. Y. Howe, M. M. Titirici, *Langmuir* **2012**, *28*, 12373–12383.
[21] Y. Yang, Z. Tong, T. Ngai, C. Wang, *ACS Appl. Mater. Interfaces* **2014**, *6*, 6351–6360.
[22] J. Huang, Z. Yan, *Langmuir* **2018**, *34*, 1890–1898.
[23] C. Xu, C. Jiao, R. Yao, A. Lin, W. Jiao, *Environ. Pollut.* **2018**, *233*, 194–200.
[24] X. Ma, C. Liu, D. P. Anderson, P. R. Chang, *Chemosphere* **2016**, *165*, 399–408.
[25] J. Wang, X. Guo, *J. Hazard. Mater.* **2020**, *390*, 122156.
[26] S. Azizian, *J. Colloid Interface Sci.* **2004**, *276*, 47–52.
[27] Y. Liu, L. Shen, *Langmuir* **2008**, *24*, 11625–11630.

Chapter 2

Porosity-induced improvement in KOH activation of chitin nanofiber-based porous carbon leading to ultrahigh specific capacitance

2.1. Introduction

In Chapter 1, it was shown that cellulose nanofiber-based porous carbon could be synthesized *via* nanoparticle templating with PSL. The addition of PF127 however results in the formation of secondary templates that affect the formation and distribution of the mesopores formed through PSL. Therefore, to optimize template carbon monolith synthesis conditions, using a natural nanofiber that can directly stabilize PSL could result in a more uniform pore distribution and higher PSL loading.

It was then found that TEMPO-oxidized chitin nanofibers (CtNF) could perform this function through the lowering of the ζ-potential of the nanofiber surface from the presence of amide bonds (**Scheme 2-1**). Furthermore, aside from using chitin as a natural N-doping agent for porous carbon[1,2], other methods to utilize this natural resource is presented in this chapter.

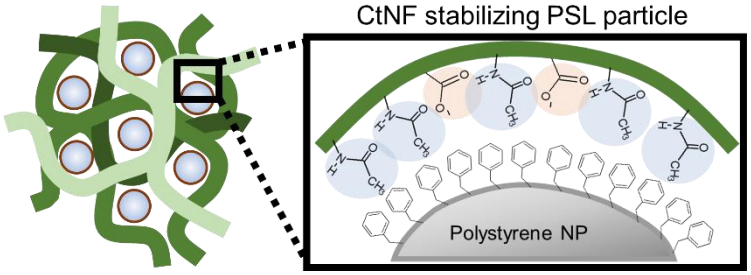

Scheme 2-1. CtNF fibers wrapping around PSL.

Hydrothermal carbonization was used again in this chapter. The hydrothermal decomposition of chitin is known to be very similar to that of cellulose, with minimal changes being that nitrogen-containing organic compounds are also found in the organic phase[3,4].

In addition, KOH activation was performed on the chitin-based CMs to improve microporosity and surface area. KOH activation is the method of etching the surface of the carbon material through the removal of C atoms through reacting with compounds formed from KOH.[5] Below 700 ^{o}C, KOH forms K_2O through thermal decomposition, as well as K_2CO_3 from reacting with surface carbon. Above 700 ^{o}C, K_2CO_3 again reacts surface carbon to decompose into metallic K and CO. K_2CO_3 could also simply decompose into CO_2 and K_2O[6].

In this study, activated hierarchically porous carbon (AHPC) was synthesized *via* PSL-based nanoparticle templating with hydrothermal carbonization and subsequent KOH activation. The effect of hydrothermal treatment, PSL amount, and carbonization were evaluated, and AHPC was tested as a potential supercapacitor electrode.

2.2. Experimental Section

2.2.1. Materials

The reagents used were chitin powder from shrimp shells (Sigma-Aldrich), NaBr (Sigma-Aldrich), TEMPO (Tokyo Chemical Industry), 8.5%–13.5% NaClO solution (Nacalai Tesque), 0.5 mol/L NaOH solution (Sigma-Aldrich), styrene monomer (Nacalai Tesque) distilled once under low vacuum, ammonium persulfate (APS) (Sigma-Aldrich), sodium dodecyl sulfate (SDS) (Wako Pure Chemical Corporation), KOH pellets (Wako Pure Chemical Corporation), 0.8% Nafion solution prepared from 5% Nafion solution (Wako Pure Chemical Corporation) with isopropanol, carbon black (Strem Chemicals, Inc.), and H_2SO_4 (Wako Pure Chemical Corporation). Excluding the styrene monomer, all reagents were used as received.

2.2.2. Synthesis of TEMPO-Oxidized Chitin Nanofibers (CtNF)

The TEMPO-oxidized synthesis of CtNFs was based the method by Isogai et al.[7,8]; it was modified with techniques used for the synthesis of cellulose nanofibers.[9] Chitin powder

(4.0 g), NaBr (0.4 g), and TEMPO (0.064 g) were added to deionized water (300 mL) and stirred for 2 h until homogeneous, which resulted in the swelling of chitin. NaClO (18 mL) was added dropwise to the solution while the pH was maintained for 2 h at 10.75 using an autotitrator and 0.5 mol L^{-1} NaOH solution. When the solution changed color from yellow to white, the reaction was terminated by adding 5 mL of ethanol. The resulting chitin pulp was isolated from the liquid *via* initial centrifugation at 8000 rpm followed by redispersion in water (40 mL) and subsequent centrifugation at 8000 rpm. This process of purifying the pulp was performed five times to maximize CtNF dispersion. The dispersion was then diluted with water (1 % wt./wt.) and defibrillated for 0.5 h by using a high-speed blender.

2.2.3. Synthesis of Activated Hierarchically Porous Carbons (AHPC)

An aqueous dispersion of CtNFs (dry wt. 100 mg), PSL, and water (total volume of 15 mL) was mixed for 1 h until homogeneous. The viscous white mixture was then transferred to a Teflon-lined stainless-steel autoclave and placed in an oven for 48 h for HT. After cooling to room temperature, the HM was taken out from the supernatant, washed three times each with ethanol and water, and freeze-dried at -47 ^{o}C for 48 h. The CMs were formed by carbonizing HC at 500–900 °C, with the temperature profile utilizing a heating rate of 5 °C min^{-1} and a hold time of 2 h. For KOH activation, CMs were ground using a mortar and pestle and mixed with KOH (aq), resulting in a slurry (3 KOH:1 CM w/w). The slurry was placed under vacuum for 5 min, for a total of five times, to ensure deep penetration of the KOH solution into the CM pores. The slurry was then dried at 85 °C overnight, and then heated at 10 °C min^{-1} to 800 °C under an Ar atmosphere and kept at this temperature for 1.5 h. The carbon material was then washed five times with 1 mol L^{-1} HCl and then placed under vacuum for 5 min to ensure the complete removal of unreacted KOH from inside the pores. Finally, AHPC was washed with

water until neutral and then dried overnight in an oven at 85 °C. The list and labels for each sample synthesized is listed in **Table 2-1**.

Table 2-1. List of samples presented in this study. The samples are labelled as the material type, followed by the sample code listed below. The material type corresponds to the step in the synthesis, with HM, CM, and AHPC corresponding to the hydrochar monolith, carbon monolith, and activated hierarchical porous carbon, respectively. The sample code consists of H for hydrothermal treatment temperature (eg. H180 → 180°C), P refers to the PSL amount (eg. P10 → 160 mg), and C refers to the carbonization temperature to form CM (eg. C5 → 500°C).

Sample code	HT Temp.	PSL Amount	Carbonization Temperature
Synthesis characterization			
P (=H220, P10C5)	220 °C	160 mg	500 °C
Px (no PSL)	220 °C	-	500 °C
Effect of Hydrothermal Treatment			
H160	160 °C	160 mg	500 °C
H180	180 °C	160 mg	500 °C
H200	200 °C	160 mg	500 °C
H220 (=P, P10C5)	220 °C	160 mg	500 °C
Amount of PSL and Carbonization Temperature			
PmCn		m	n
	220 °C	1 → 16 mg	5 → 500 °C
m = PSL amount		2 → 32 mg	6 → 600 °C
n = carbonization		5 → 80 mg	7 → 700 °C
temperature		7 → 112 mg	8 → 800 °C
		10 → 160 mg	9 → 900 °C
		20 → 320 mg	

2.2.4. Characterization

Scanning electron microscopy (SEM) micrographs were obtained using a Hitachi SU3500 microscope. Dynamic light scattering (DLS) spectra were taken using an Otsuka ELSZ -2000 Particle Size Analyzer. Brunauer-Emmett-Teller (BET) surface area measurements were performed using a Quantachrome NOVA 4200e surface area and pore size analyzer with the

associated program NovaWin for data analysis. All samples were dried at 90^{o}C for 24h in vacuum prior to surface area measurement. X-ray photoelectron spectroscopy (XPS) spectra were taken using a JEOL JPS-9010MC XPS instrument with monochromatic AlKα-radiation. CasaXPS Version 2.3.15 was used for analyzing the C1s, N1s, and O1s narrow XPS profile. Raman spectrographs were taken using a Jasco NRS-3100 Laser Raman Spectrophotometer (532.190 nm). All Raman spectra were deconvoluted using Gaussian fitting. Thermogravimetric analysis (TGA) was done using a SII TG/DTA7200 Instrument. Infrared spectrographs (IR) were taken using a Thermo Scientific Nicolet iS5 infrared spectrophotometer with an iD5 ATR attachment. Transmission electron microscopy (TEM) was performed using a Hitachi H-7650 microscope. Energy dispersive X-ray spectroscopy (EDS) data were taken using a Hitachi Miniscope TM 3000 with Swift ED 3000.

2.2.5. Electrochemical Studies

A three-electrode system was used to measure the specific capacitance of AHPC. This system consisted of an Ag|AgCl reference electrode (RE-1B, BAS), a Pt wire counter electrode, a glassy carbon electrode with the cast AHPC-based carbon film as the working electrode, and a 1 mol L^{-1} H_2SO_4 electrolyte solution. The working electrode was prepared by grinding 200 mg of AHPC into a powder ($d \leq 45$ μm) and then dispersing this powder and 5% wt./wt. carbon black in a 0.8% Nafion isopropanol solution to obtain a 50 mg mL^{-1} AHPC casting solution. A total of 2 μL of this solution was cast onto a glassy carbon electrode (diameter = 3 mm) and then air-dried for 24 h, resulting in an electrode consisting of 100 μg AHPC, 5 μg carbon black, and 0.8 μg Nafion. The electrodes were immersed in the electrolyte solution and placed under vacuum for 5 min, at five intervals, to ensure sufficiently deep penetration of the electrolyte. The entire system was then purged with Ar for 0.5 h, while maintaining the temperature at 25 °C,

before measurement. All measurements were performed using an ALS/CH Model 600e electrochemical analyzer, with ALS/CH 7002e used for data collection and analysis.

Cyclic voltammetry (CV) was performed at varying scan rates (50, 100, 200, and 300 mV s^{-1}), with a potential window of −0.2–0.8 V and at a rate of 10 cycles per scan. Galvanostatic charge-discharge (GCD) measurements were performed at varying current densities I_m (0.5, 1, 2, 3, 4, and 5 A g^{-1}), with a potential window of −0.2–0.8 V. Because all samples exhibited near-linear charge–discharge behavior, specific capacitance C_{sp} (F g^{-1}) was calculated using the following equation (**Equation 2-1**),

$$C_{sp} = \frac{I \times \Delta t}{\Delta V \times m} = I_m \times \Delta t \qquad \textbf{(Equation 2-1)}$$

where I is the current (A), Δt is the time for one charge cycle (s), ΔV is the voltage range (V), and m is the mass of the active material (g). The equation can be further simplified to Δt multiplied by current density I_m (A g^{-1}), because the potential window is 1.0 V.

2.3. Results and Discussion

2.3.1. Characterization

Characterization of TEMPO-oxidized chitin nanofibers

In a previous work, it has been reported that the pore structure of carbons derived from nanofiber-based hydrochar precursors rely on the additional mechanism of fiber entanglement that keeps the templating material (ie. PSL) in place, which is why chitin was oxidized to form nanofibers. After TEMPO oxidation, CtNF had formed fibers 20-60nm thick (**Figure 2-1**A), and the formation of carboxylic acid groups at the C6 of chitin was confirmed *via* IR (**Figure 2-1**B) with a peak appearing at 1709 cm^{-1} as well as a slight decrease in the -OH peak at 3249 cm^{-1}. XPS C1s spectra (**Figure 2-1**C) also showed an additional peak at the 288.98 eV

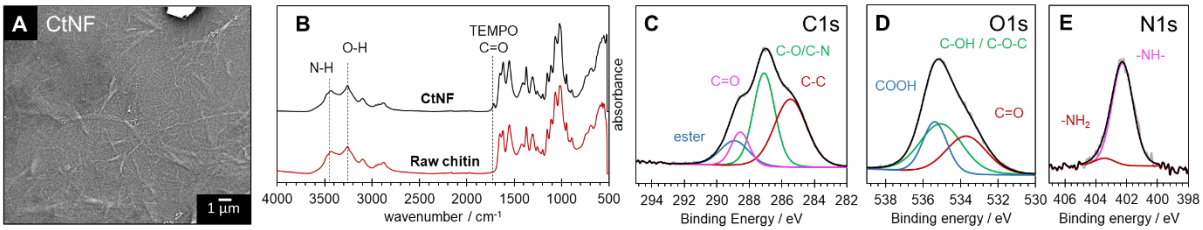

Figure 2-1. Characterization of CtNF. A) IR spectra of CtNF and raw chitin. B-D) XPS narrow spectra of CtNF for C1s, O1s, and N1s respectively. E) SEM micrograph of CtNF.

corresponding to a COOH ester group which did not show with chitin XPS. The O1s spectra (**Figure 2-1**D) shows the same result as the 535.3-535.5 eV peak corresponding to carboxyl increased, indicating successful oxidation.

Characterization of PSL-templated, CtNF-based hydrochars and carbon monoliths

When used as carbon precursors, monosaccharides[10,11] and polysaccharides[12,13] typically undergo a decomposition mechanism involving the formation of 5-hydroxymethylfurfural (5-HMF) and other organic compounds during hydrothermal treatment, which then repolymerize to form the solid called hydrochar.[14,15] Chitin and chitosan are assumed to follow a decomposition mechanism similar to that of cellulose, with nitrogen-containing compounds present in both the organic and aqueous phases after HT.[3,16] To confirm this, HMs without PSL (HM-Px) were observed using scanning electron microscopy (SEM) (**Figure 2-2**A). The porosity of the material did not change after carbonization (denoted as CM-Px, **Figure 2-2**B). The formation of a hydrochar completely retaining the shape of the autoclave vessel indicates chitin gelation.[17] Nanofiber entanglement as well as the crosslinking between compounds formed during polymer decomposition and subsequent repolymerization of 5-HMF are the driving mechanisms underlying the formation of the observed bulk structure.[9] A few remaining fibers are visible in **Figure 2-2**a, as shown in the inset; however, the fibers are largely

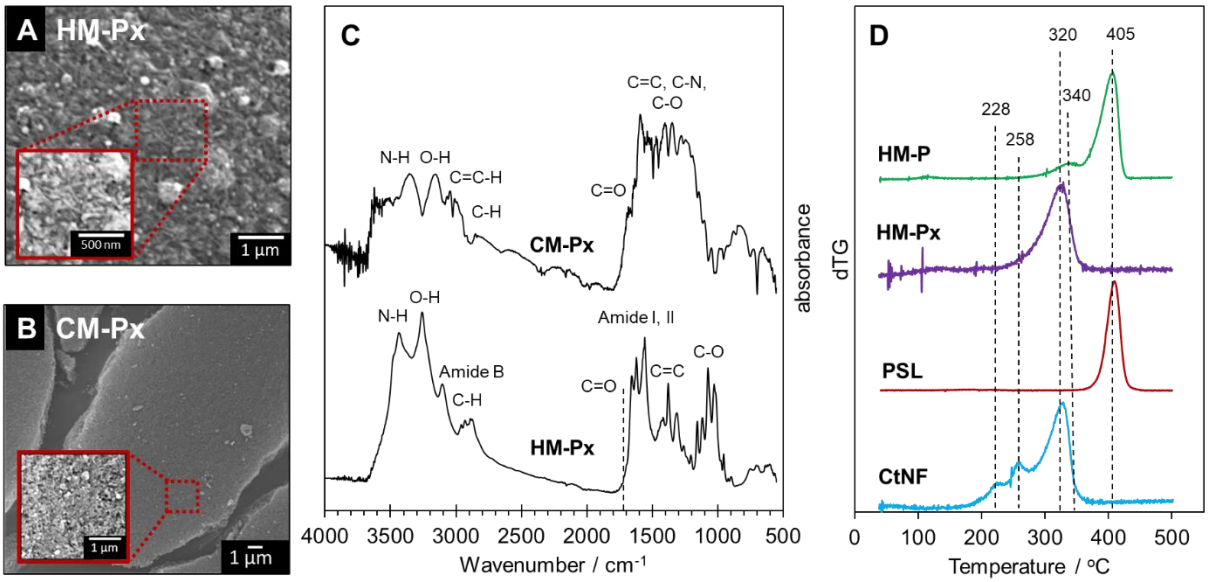

Figure 2-2. SEM images of A) the CtNF hydrochar without PSL (HM-Px) and B) its corresponding carbon monolith (CM-Px) after carbonization at 500 °C. C) IR spectra of HM-Px and CM-Px. D) dTG curves of CtNF and PSL polymer precursors and hydrochars HM-Px and HM-P.

decomposed at 220 °C. After HT, CtNFs usually forms sheets of micrometer-scale thickness, containing small pores. CtNFs were also found to form aggregates at random points with no apparent porosity (**Figure 2-2**B). The infrared (IR) spectra of HM-Px (**Figure 2-2**) confirmed that while the CtNF remained mostly intact, further oxidation occurred during HT. This is evident by the increased intensity and merging of the IR COOH peak at 1710 cm^{-1} with the amide I and II peaks at 1600–1700 cm^{-1} and 1500 cm^{-1}, respectively[18]. Desaturation was also observed with the appearance of C=C in the 1373–1416 cm^{-1} region. After carbonization (**Figure 2-2**C), the presence of high O content and low N content in the CtNFs resulted in an abundance of C=O, C-O, and C-N in CM-Px, giving rise to a large broad peak in the 1070–1745 cm^{-1} region. Some O and N atoms exist as O-H and N-H terminal functional groups, as indicated by the peaks in the 3300–3400 cm^{-1} region. The carbon in CM-Px is likely unsaturated, as indicated by the absence of a significant sp^3 C-H peak in the 2800–2900 cm^{-1} region. A

presence of a strong C=C-H stretching peak at 3055 cm^{-1} indicates the presence of unsaturated carbon.

The carbonization of CtNFs was investigated through thermogravimetric analysis (TGA) by plotting the change in mass against temperature (dTG) against the treatment temperature for both HM-P and HM-Px (**Figure 2-2**D). Raw CtNFs exhibited degradation peaks at 228, 258, and 320 °C corresponding to TEMPO COOH removal and oligomer formation, acetamide evolution, and hydrochar formation, respectively.[19] Hydrothermally treated CtNFs exhibited weak peaks at 228 and 258 °C, indicating hydrochar crosslinking between the amine groups. The broad decomposition peak of HM-Px was observed from approximately 320 °C, indicating that while CO_2 and acetamide were not the primary species released from the sample, different organic compounds were volatilized before hydrochar formation. When PSL was added to the system, hydrochar formation began at an elevated temperature of 340 °C and, thereafter, PSL degrades at 405 °C. For HM-P, volatile degradation products, possibly from the PSL–hydrochar interface, were released at temperatures below 405 °C, as indicated by the pronounced extension of the PSL peak, which starts at 365 °C.

2.3.2. Effect of Hydrothermal Treatment

The reactions that occur during HT are largely affected by temperature and result in different temperature ranges for solid and liquid products.[15] During HT, practical solid formation occurred only at 100–230 °C, while optimal solid formation was observed from ~160 °C[15]; therefore, monoliths over the 160–220 °C range were synthesized and investigated. From the SEM images of the hydrochars (HM-H160 to HM-H220), it was observed that the structure formed after varying the HT temperature differed according to the severity of fiber decomposition, which affects PSL coverage by the matrix. As expected, at low HT temperatures, only partial fiber decomposition was observed, with a higher degree of fibers visible for HM-

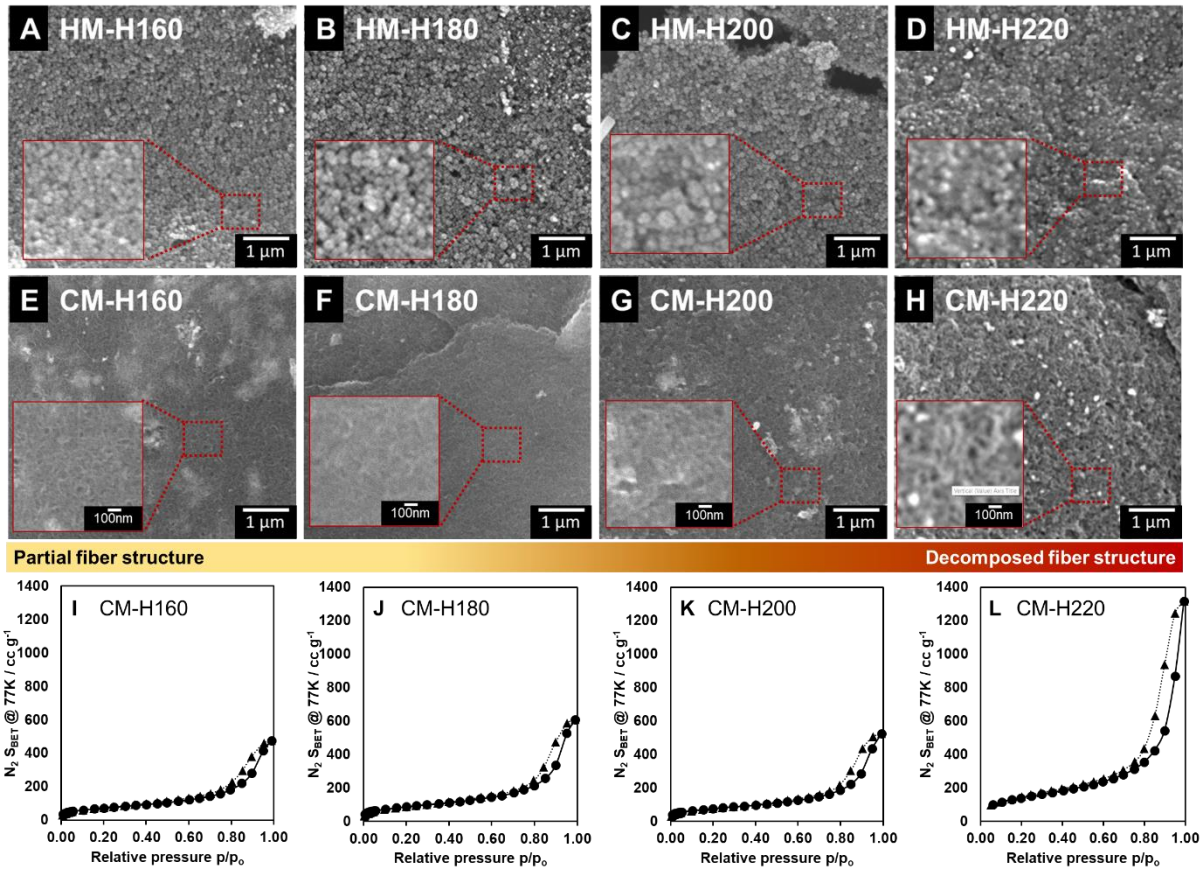

Figure 2-3. A-D) SEM images of HMs with increasing HT temperatures. E-H) CMs derived from HMs in A-D, carbonized at 500 °C. I-L) BET isotherms of CMs in E-H.

H160 and HM-H180 in **Figure 2-3**A and **Figure 2-3**B, respectively. When the degree of CtNF decomposition was low, repolymerized decomposition products were formed because HT did not allow the filling of gaps between the CtNFs and PSL, or among CtNFs, resulting in the formation of gaps within the HM. The structure was retained after carbonization, and the partial fiber structures of CM-H160 and CM-H180 (**Figure 2-3**E and F) were observed to have a low surface area (**Figure 2-3**I and J). At high HT temperatures, the degree of decomposition increased, resulting in the formation of the decomposed fiber structure in CM-H200 and CM-H220 (**Figure 2-3**G and H). The two types of structures appear to transition at approximately 180–200 °C, with HM-H200 (**Figure 2-3**C) resembling HM-H220, and HM-H180 resembling HM-H160. For CM-H220, the fibers in HM-H220 appear decomposed and have filled the

spaces between PSL (**Figure 2-3**D), resulting in pores that match the size and shape of those of PSL (**Figure 2-3**H). Over the entire temperature range investigated, the temperature was high enough to decompose CtNFs with a significant amount of the fibers converting to constituent furan and pyrrole-derived compounds[20] that repolymerize in the spaces between the CtNFs and PSL. An increase in the degree of decomposition resulted in more effective templating, as indicated by the jump in S_{BET} from an average of 285 $m^2\ g^{-1}$ for CM-H160 to an average of 475 $m^2\ g^{-1}$ for CM-H220 (**Table 2-2**). The Brunauer-Emmett-Teller N_2 adsorption-desorption (BET) isotherms changed from type IV H3 to type IV H1 (**Figure 2-3**L), indicating a uniform and continuous pore network within the carbon material. HM comprised similar functional groups, as indicated by its near-identical IR spectra. However, the X-ray photoelectron spectra (XPS) of CM-H160 and CM-H220 (**Table 2-2**) showed that there was a notable decrease in the O/C ratio, from 0.20 to 0.12 in HM-H180 and HM-H200, respectively. This likely indicates that the dehydration of hydrochar resulted in the decomposition of the fiber structure. The N content did not change significantly, remaining at approximately 3% for all HT temperatures. Based on the more defined pore network as indicated by the type IV H1 hysteresis curve, and a higher S_{BET}, 220 °C was determined to be the optimal HT temperature.

Table 2-2. BET Surface area and XPS elemental composition of CM-H160 to CM-H220 carbonized at 500°C.

HT temp	S_{BET}	BJH V_{total}	BJH V_{micro}	BJH $V_{meso-macro}$	XPS				
°C	$m^2\ g^{-1}$	cc g^{-1}	cc g^{-1}	cc g^{-1}	C%	O%	O/C	N%	N/C
160°C	264	0.77	0.07 (9.09%)	0.70 (90.91%)	80.8	16.4	0.20	2.8	0.04
180°C	317	0.98	0.08 (8.16%)	0.90 (91.84%)	80.7	15.8	0.20	3.5	0.04
200°C	275	0.86	0.08 (9.30%)	0.78 (90.70%)	86.7	9.9	0.12	3.3	0.04
220°C	475	2.06	0.12 (5.79%)	1.94 (94.21%)	85.5	10.7	0.13	3.8	0.04

2.3.3. Effect of PSL and Carbonization Temperature

Structure optimization and surface area control on the basis of PSL amount were investigated at different carbonization temperatures. These were achieved by using HM-H220 and adjusting the PSL amount from 16 to 320 mg, and the carbonization temperature from 500 to 900 °C. PSL was well distributed within the hydrochar up to 160 mg PSL (**Figure 2-4**A-C), and no apparent changes in surface morphology were observed. When the PSL amount was increased to 320 mg (**Figure 2-4**D), the aggregates of up to 1 μm in diameter were observed. The larger particles are likely partially fused or aggregated PSL not stabilized by the CtNFs. This phenomenon was also observed when PSL was hydrothermally treated without the CtNFs, which resulted in coalescence of PSL at the bottom of the Teflon-lined vessel. After the

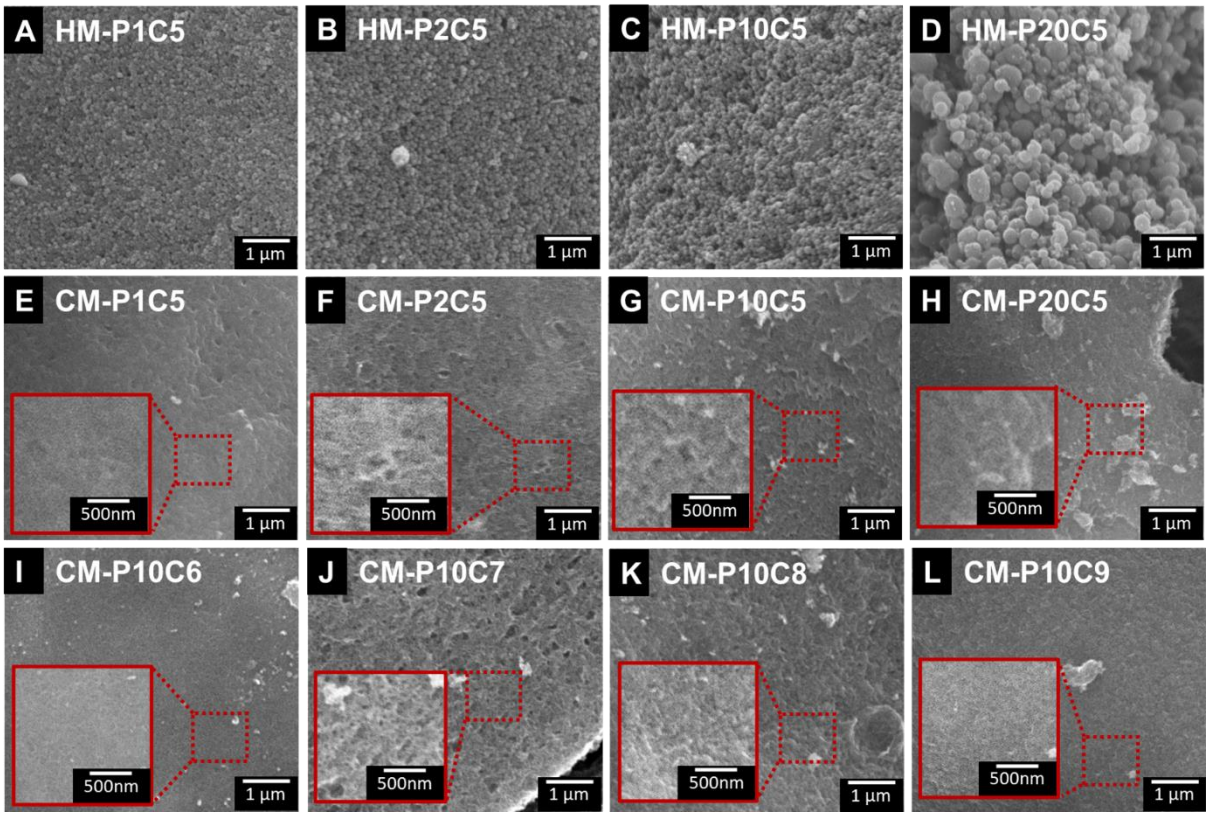

Figure 2-4. SEM images of A-D) HMs with increasing PSL amount, E-H) the corresponding CMs after carbonization at 500 °C, and I-L) CMs treated at increasing carbonization temperatures.

carbonization of the HM, the number of pores increased as the PSL amount increased from 16 to 160 mg, as observed in the SEM images of CM-P1C5–CM-P10C5 (**Figure 2-4**E-G). The average mesopore size of 31 nm is 60.5 % of the size of the PSL particles—this shrinkage is likely due to polymer degradation[21–23] as well as monolith shrinkage from the evolution of oxygen and nitrogen-based compounds[24,25]. Similar pore shrinkage was observed for other studies using PSL as a porogen[26–28]. While the pore structures of CM-P5C5 and CM-P10C5 were relatively similar, the decrease in PSL size uniformity due to PSL agglomeration was reflected in HM-P20C5 and did not change after carbonization (**Figure 2-4**H). The comparison of the SEM images of the CMs carbonized at 500–900 °C with 160 mg PSL (**Figure 2-4**I-L) indicated that increasing the carbonization temperature did not affect the mesopore structure because structure formation occurred at a temperature below 500 °C. This was predicted by the pore formation mechanism, shown in the hydrochar TGA result in **Figure 2-2**D, and was in agreement with the results of other studies utilizing PSL as the pore-inducing template.[9,29] This was also observed for all other CMs with varying amounts of PSL.

The BET analysis results indicated that increasing the PSL amount increased the surface area (**Figure 2-5**A) and that PSL had a direct effect on the morphology and uniformity of the pore structure of the CMs. CM-P1C5 and CM-P2C5 exhibited type IV H3 isotherms, which is indicative of non-uniform pore sizes. Increasing the amount of template resulted in a transition from H3 to H1 type isotherms for CM-P5C5–CM-P10C5. This indicated that with higher amounts of the template, CtNFs coating each template is further distributed among more particles, resulting in increased pore uniformity and connectivity. For CM-P20C5, a wider pore size distribution was indicated by the transition between type IV H1 and H3 isotherms. This resulted from the coalescence of PSL although a high amount of PSL was embedded in the hydrochar. One possible explanation for the plateauing of S_{BET} could be the instability of PSL during overtemplating, at which not all PSL is not stabilized by CtNFs. For 16–160 mg PSL,

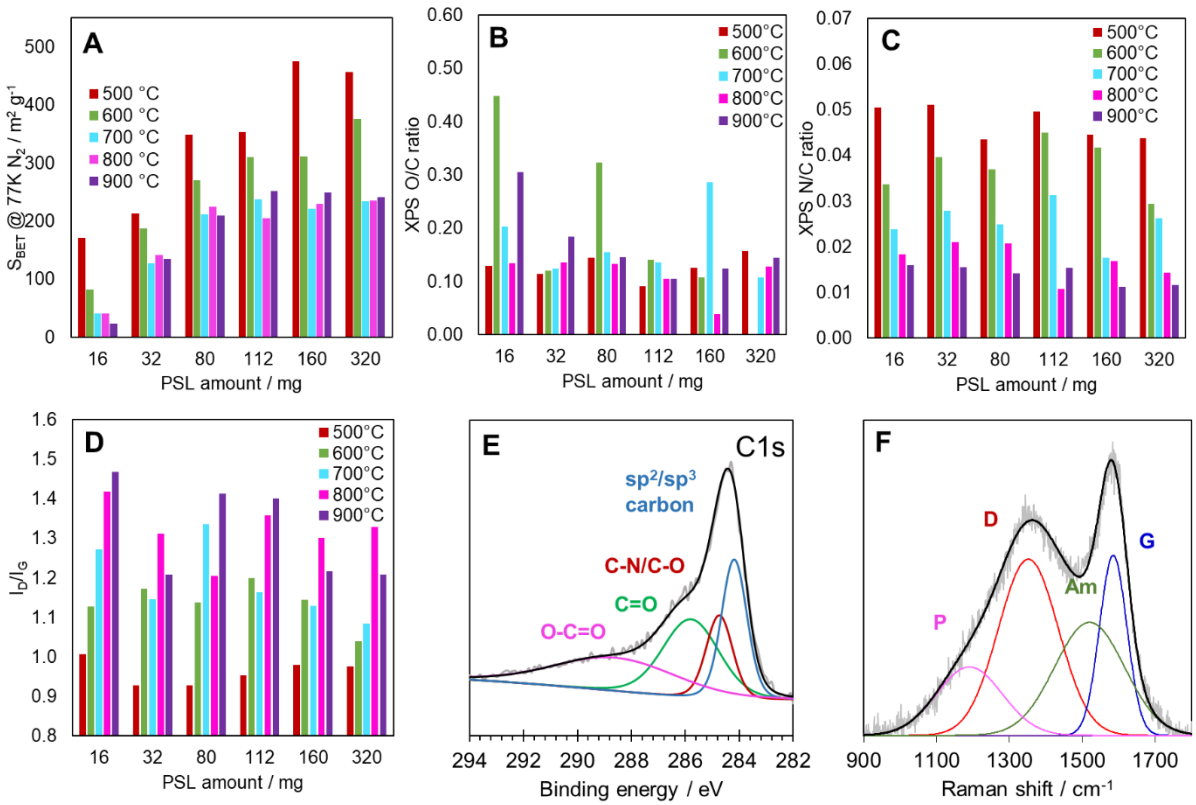

Figure 2-5. Effect of PSL amount and carbonization temperature on A) S_{BET}, B) XPS O/C ratio, C) XPS N/C ratio, and D) Raman I_D/I_G ratio of CMs. E) C1s XPS narrow spectrum of CM-P10C5. F) Raman spectrum of CM-P10C5 as a typical example.

the template did not agglomerate, and increasing the amount of templating material resulted in a corresponding increase in S_{BET}. In the presence of high PSL amount, the template agglomerated and was not uniformly distributed within the CtNF matrix, leading to a smaller increase in the surface area. The same trend was observed for the samples carbonized at high temperatures (**Figure 2-5**A), and temperature-dependent carbon sintering was observed, further lowering the overall surface area[30,31]. For CtNF-based PSL-templated hydrochars, the sintering effect causes the CMs treated at >700 °C to exhibit similar S_{BET} values.

The XPS spectra of the samples (**Figure 2-5**B) showed that the O content of the CMs, at an average value of 13.1%, was not affected by the PSL amount or carbonization temperature indicating a similar surface state across the samples. The peak fitting of the C1s spectra of CM-

P10C5 (**Figure 2-5**E) indicated an abundance of C=O/O-C=O bonds at 286–290 eV. The N content decreased with increasing temperature, regardless of the PSL amount (**Figure 2-5**C). This was likely due to the evolution of species such as N_2, NH_3, and HCN, from the N embedded in the hydrochar, following a mechanism similar to that observed for carbonized polyacrylonitrile (PAN) fibers[32,33]. The N1s peak was too small to be deconvoluted and was excluded from further analysis.

Raman analysis showed that the relationship between the PSL amount and the I_D/I_G ratio of CMs was unclear (**Figure 2-5**D). However, the carbonization temperature increased I_D/I_G at all PSL amounts, further indicating that the temperature at which PSL thermally decomposes to form mesopores does not overlap with the onset temperature of hydrochar pyrolysis. Furthermore, changes in the CM pore size could be attributed to transformations in the carbon material that could be observed through Raman spectroscopy. Ko et al. reported that increasing I_D/I_G ratios caused by increased carbonization temperature for phenolic resin-based carbons could be associated with crosslinking reactions below 700 ^oC[34]. Note that CMs were carbonized from hydrochars, which adopt a composite cellulosic fiber with resin-like structure after hydrothermal treatment[35–37]. Increased I_D/I_G ratio of the G (1585 cm^{-1}) and D (1352 cm^{-1}) bands at 700-1000^{o}C could then be explained by structural changes of the carbon structure. The observed decrease in pore size from pore sintering in CMs carbonized at 700-900 ^{o}C (CM-PmC7 to CM-PmC9) are in agreement with the first stage of the 3-stage carbon amorphization model proposed by Ferrari and Robertson[38]. The transition of graphitic carbon to nanocrystalline graphite is indicated by the increase in the I_D/I_G as well as the shift of the G-band position[39]. CM-PmC5 had an average G position of 1583 cm^{-1}. This then increases to 1586 cm^{-1} and 1592 cm^{-1} for CM-PmC7 and CM-PmC9, respectively. CM-PmC7 to CM-PmC9 samples undergoing both transformations before and after 700 ^{o}C further explains the temperature-dependent pore sintering effect. CMs with varying amount of PSL had very similar

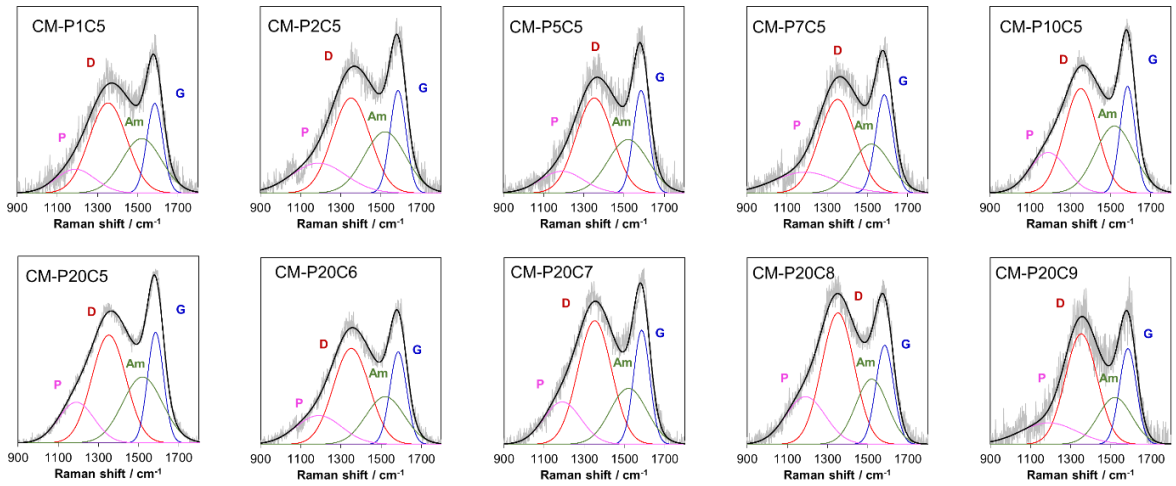

Figure 2-6. Top: Deconvoluted Raman spectra of samples with increasing PSL content. Bottom: Deconvoluted Raman spectra of CM with 320mg PSL carbonized at increasing treatment temperatures.

G-band positions, further confirming that mesoporosity did not have an effect in carbon transformation. In addition to the I_D/I_G ratio, peak fitting indicated additional peaks for Am (1520 cm^{-1}) and P (1190 cm^{-1}) that are attributed to amorphous carbon and sp^3-bonded carbon[40,41] point to a highly amorphous carbon material (**Figure 2-5**F, **Figure 2-6**).

2.3.4. Effect of KOH Activation

Having established that PSL templating does not induce micropore formation, KOH activation was performed at 800 °C with a mass ratio of 3:1 KOH/carbon[2,42] to increase the surface area through micropore formation. The SEM images show that the structure formed during carbonization was largely retained after activation, as indicated by the similar mesopore structures formed in AHPC-P10C5 and AHPC-P20C5 (**Figure 2-7**A, B). Observation of AHPC-P10C5 under TEM indicated pore connectivity shown by CM-H220 was also retained given the distribution of the lighter regions associated with voids within the AHPC (**Figure 2-8**). Sintered pores were observed for samples such as AHPC-P20C9 (**Figure 2-7**C) and it was

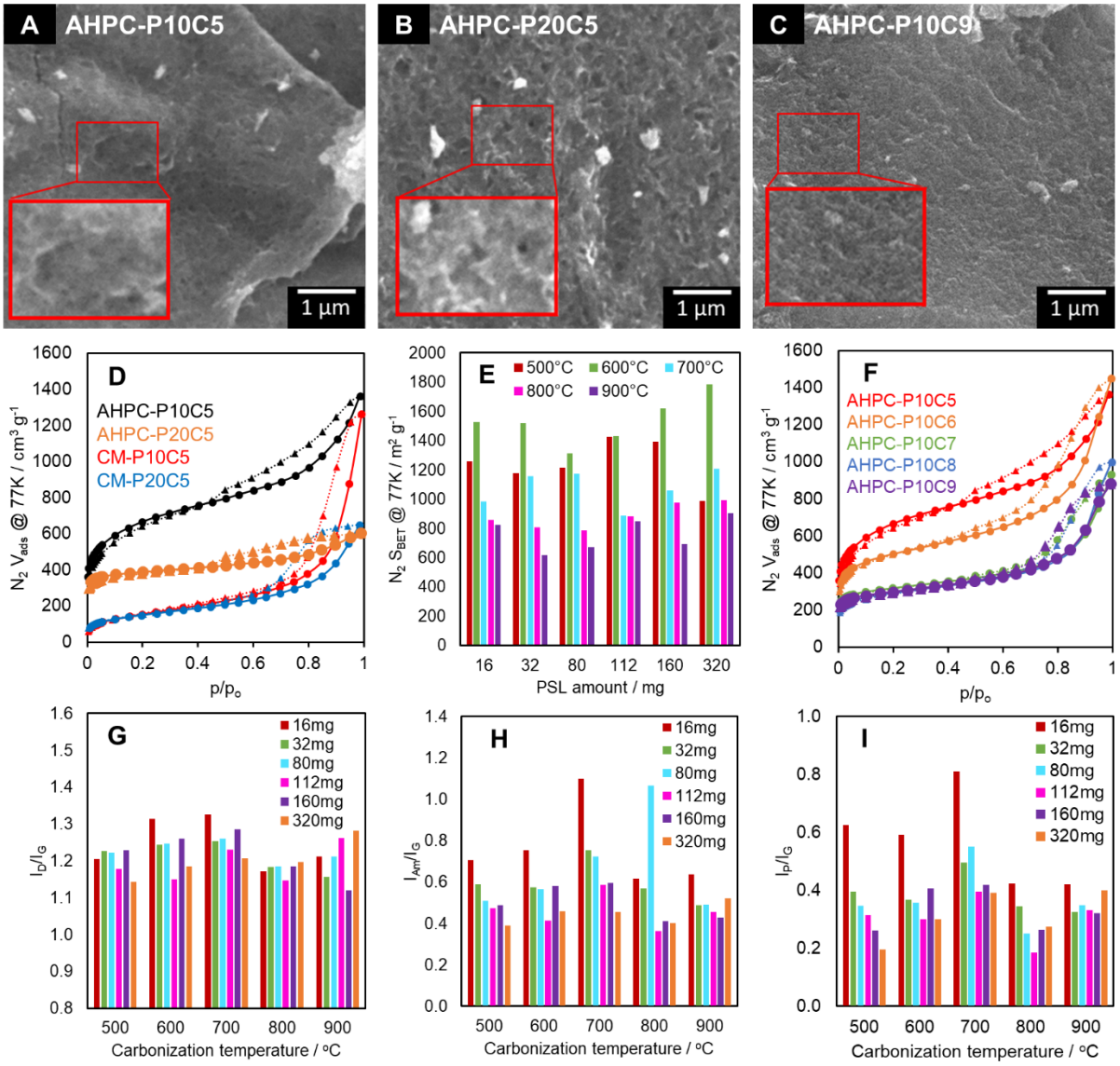

Figure 2-7. SEM images of A) AHPC-P10C5, B) AHPC-P20C5, and C) AHPC-P20C9. D) BET isotherms of CMs and AHPCs with different PSL amounts. E) PSL amount and initial carbonization temperature as a function of S_{BET} of AHPCs activated at 800 °C. F) BET isotherms of AHPC-P10Cn synthesized at different carbonization temperatures. Plots of G) I_D/I_G, H) I_{Am}/I_G, and I) I_P/I_G of AHPCs with different PSL amounts and initial carbonization temperatures.

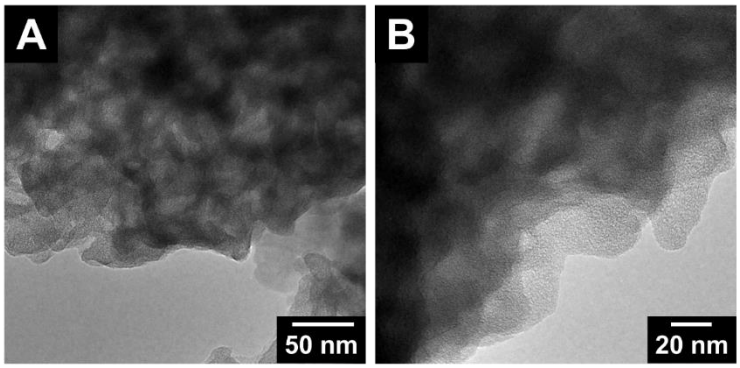

Figure 2-8. TEM image of AHPC-P10C5 at A) lower and B) higher magnification.

confirmed that KOH activation largely results in the formation of micropores, and not mesopores, as shown in the BET isotherms (**Figure 2-7**D). An upward shift in the low p/p_o region of the isotherms was observed for both AHPC-P10C5 and AHPC-P20C5, indicating the formation of micropores. Across the investigated PSL range (**Figure 2-7**E), the AHPC surface area did not increase linearly as was observed for the CMs, which was expected considering that S_{BET} is largely influenced by micropores, and not mesopores. The carbonization temperature prior to activation affected the susceptibility of carbon to form micropores (**Figure 2-7**F), with the CM carbonized at 500–600 °C exhibiting a higher S_{BET} than that of the CM carbonized at 700–900 °C. This was likely due to the formation of thermally inert carbon during carbonization at higher temperatures, which would not react with KOH present during the secondary heat treatment. All AHPCs had a higher S_{BET} than the CMs, although the effectiveness of activation was much higher for the CMs synthesized at 500–600 °C. The BJH analysis of the pore volume showed an increased V_{total} in relation to that of the CMs, and the ratio of V_{total} contributed by V_{micro} increased from an average of 5% for the CMs to ~35% for the AHPC-PmC5 samples. For 16–160 mg PSL, the amount of the templating material was found to have an effect on V_{micro}, as shown by the increase from 0.31 cc g^{-1} for AHPC-P1C5 to 0.84 cc g^{-1} for AHPC-P10C5. For AHPC-P20C5, V_{micro} dropped to 0.18 cc g^{-1}, which was likely due to the initial weak pore structure of CM-P20C5 being unable to support further etching.

With increasing carbonization temperature, KOH activation resulted in fewer micropores as indicated by the decrease in V_{micro}. Conversely, the $V_{meso\text{-}macro}$ ratio increased with increasing carbonization temperature until it reached an average of 90%. Notably, the mesopores formed during carbonization were not significantly affected by KOH activation, as indicated by the average decrease of 5% in $V_{meso\text{-}macro}$ observed across all CMs and AHPCs.

The XPS spectra showed that for AHPC-PmC5–AHPC-PmC8, there was a 10%–15% and 16%–22% increase, respectively, in the average AHPC O/C content in relation to that of the CM. This trend was not observed for all AHPC carbonized at 900 ºC (AHPC-PmC9), wherein the O/C content remained at 11.3%–18.6%. Notably, surface nitrogen was largely removed after KOH activation to the point that the N at% cannot be accurately measured. Measuring the elemental composition of AHPC-P10C5 using energy dispersive X-ray spectroscopy (EDS) showed no traces of N (**Figure 2-9**).

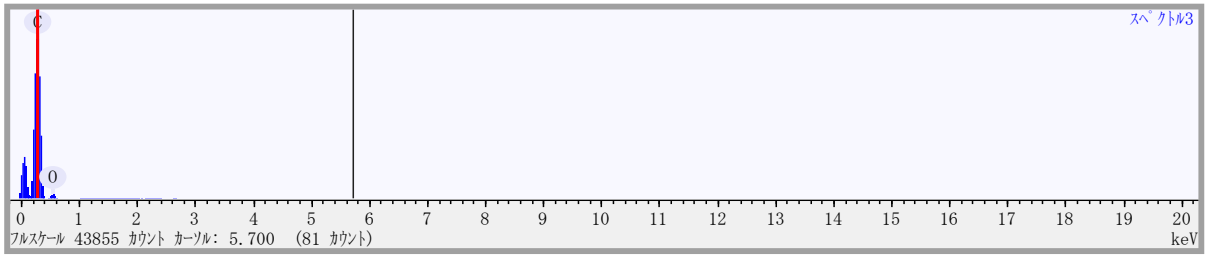

Figure 2-9. EDS spectra of AHPC-P10C5.

The Raman spectra of the AHPCs showed that I_D/I_G was unaffected by the initial CM carbonization temperature after activation (**Figure 2-7**G). There was a slight decrease in I_D/I_G and a very clear decrease in I_{Am}/I_G (**Figure 2-7**H) and I_P/I_G (**Figure 2-7**I) with increasing PSL amounts for CM-PmC5 to CM-PmC7. It is likely that a higher degree of porosity resulted from the increased PSL content, allowing for deeper penetration of KOH and subsequent removal of amorphous surface carbon. The effect of PSL-based porosity on I_D/I_G was not as significant as

that on I_P/I_G or I_{Am}/I_G, indicating the selective removal of amorphous and surface sp^3 carbon instead of sp^2 carbon. Previous studies showed that through the selective removal of amorphous carbon, graphitic sections of the material were revealed.[40,41] Referring to the 3-stage amorphization model to determine the effect of KOH activation on CMs reveal that the structural changes in AHPC are still within the first stage, with the G-band increasing for AHPC-PmC5 (1588 cm^{-1}) and APHC-PmC6 (1589 cm^{-1}) from their corresponding CMs from 1583 cm^{-1} and 1584 cm^{-1}, respectively. AHPC-PmC7 to AHPC-PmC9 were largely unaffected with the G-band staying at 1588 cm^{-1}. High I_D/I_G indicates the exposure of edge sites on graphene layers, with increasing PSL amount skewing the ratio slightly toward the exposure of basal planes. This was also reflected in the XPS spectra, wherein the clear separation of sp^2 and sp^3 carbon peaks was evident along with a higher peak ratio of sp^2 carbon than that of sp^3 carbon.

2.3.5. Electrochemical Studies

Due to the well-developed micro- and mesopore structure of AHPC, electrochemical studies were carried out to test the potential of AHPC as a supercapacitor electrode. Micropores are generally considered as small voids or channels <2 nm in diameter that provides the material with high surface area, allowing the buildup of charge[43]. However, during charge-discharge cycles of the electrochemical cell, small pore width (<0.7 nm) was reported to show "gate" effects where inefficient or even electrolyte penetration results in lower experimental specific capacitance than the theoretical maximum[44]. Having mesopores evenly spaced out and acting as larger channels greatly benefits carbon-based electrode materials in achieving higher specific capacitance[45,46].

As all materials exhibited nearly ideal charge–discharge behavior for both CV, and GCD, the specific capacitance (C_{sp}) at 0.5 A g^{-1} was calculated. **Figure 2-10** shows that for AHPC-PmC5, AHPC-PmC6, and AHPC-PmC7, increasing the PSL amount (i.e., the degree of

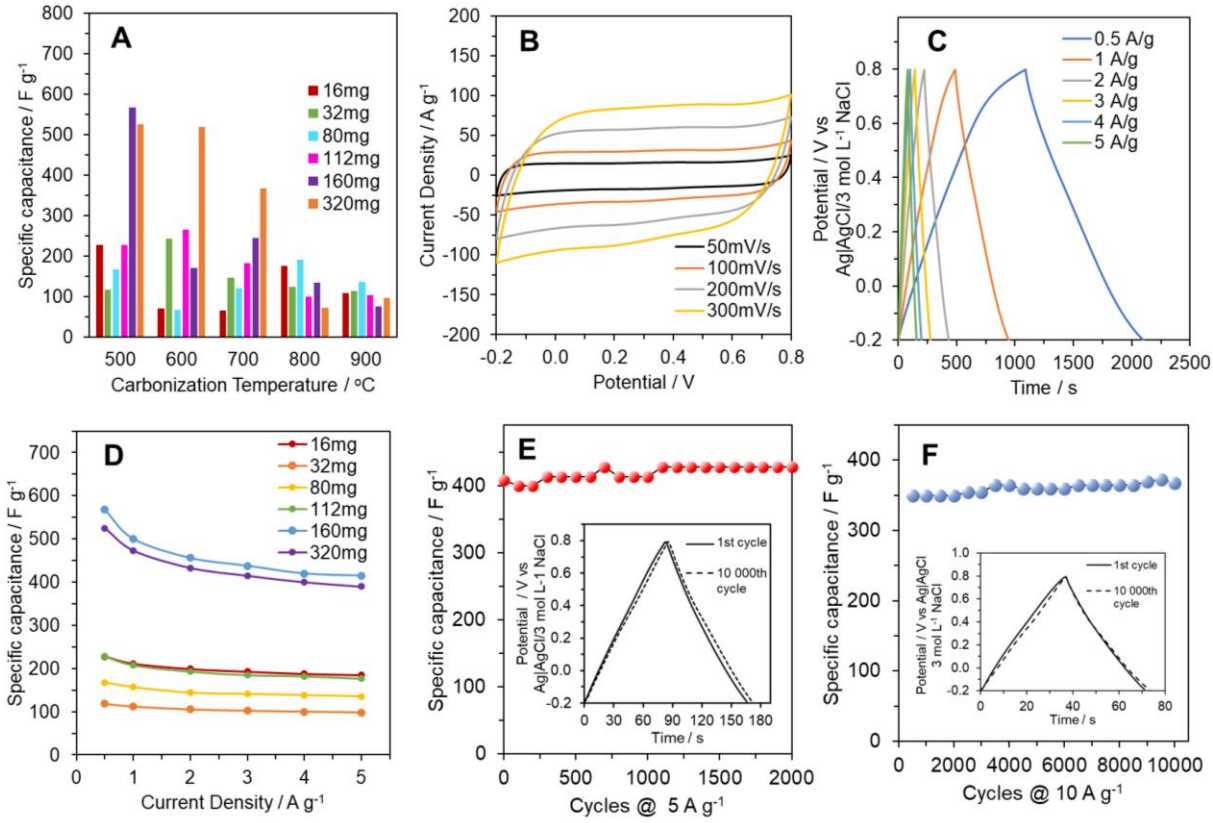

Figure 2-10. A) Effect of PSL amount and carbonization temperature on specific capacitance at 0.5 A g^{-1}. B) CV curves C) GCD curves, D) capacitance retention plot of AHPC-P10C5 up to 5 A g^{-1}, and charge cycle plot of AHPC-P10C5 at E) 5 A g^{-1} and F) 10 A g^{-1}.

mesoporosity of the carbon material) results in a general increase in C_{sp} owing to deeper penetration of the electrolyte and faster ion migration within the material. For AHPC-PmC5, the highest C_{sp} of 567 F g^{-1} was recorded for AHPC-P10C5, followed by 526 F g^{-1} for AHPC-P20C5. This coincides with the optimal PSL amount observed to be fully stabilized by the hydrothermally treated chitin matrix. Additionally, improvements to the micro- and mesopore structures enabled more efficient removal of amorphous carbon. This was shown by the decrease in the amount of amorphous carbon along with the high I_D/I_G ratio, which likely point to a high degree of graphene edge site exposure. Randin et al.[47] and Velickỳ et al.[48] showed that the specific capacitance of the edge site (50-70 µF cm^{-2}) is much higher than that of the

basal plane (16 μF cm^{-2}). A similar trend was observed at both 600 °C and 700 °C, whereat increased carbonization temperature resulted in a decrease in the maximum C_{sp} to 518 F g^{-1} and to 367 F g^{-1} for AHPC-P20C6 and AHPC-P20C7, respectively. Because the pore structure of CMs is retained within this temperature range, it is likely that the decrease in C_{sp} from 500 to 600 °C was caused by several factors: the difference in retained N content after activation, the higher I_P/I_G ratio for AHPC-P20C6, and the reduced S_{BET} upon pore sintering. Despite having no N content, AHPC-P20C6 exhibited high C_{sp}, which was likely due to graphene edge site exposure. Additionally, the I_P/I_G values for AHPC-P20C5, AHPC-P20C6, and AHPC-P20C7 increased, while C_{sp} decreased. This indicated that owing to the susceptibility of KOH activation, the CM carbonization temperature affected C_{sp} through the extent of carbon edge plane exposure. At 800–900 °C, it is likely that a different phenomenon was responsible for low C_{sp}. The thermal inertness of the CM precursor, resulting from the high carbonization temperature, and a low S_{BET} value may have affected KOH activation efficiency, resulting in low C_{sp}.

Further characterization of the optimal sample (AHPC-P10C5) was conducted. AHPC-P10C5 has EDLC that was stable at a wide scan rate of 50–300 mV s^{-1} (**Figure 2-10**B) and nearly linear charge–discharge behavior at all tested current densities (**Figure 2-10**C). It was shown that AHPC-P10C5 and AHPC-P20C5 exhibited very high C_{sp} at 0.5 A g^{-1}, and capacitance retention of 73% was observed at 5 A g^{-1} (**Figure 2-10**D). C_{sp} was known to decrease at higher current densities owing to the insufficient penetration of pores by the electrolyte. The capacitance retention after 2000 charge–discharge cycles was investigated (**Figure 2-10**E). The carbon material was found to be stable and exhibited unchanged GCD curves. Further increasing the current density to 10 A g^{-1} and charging-discharging for 10 000 cycles still showed no decrease in performance and near-identical charge-discharge behavior (**Figure 2-10**F). The specific capacitance dropped to 352 F g^{-1}, corresponding to only 62.1 %

capacitance retention, but the stable performance over long periods of use still make AHPC-P10C5 a good potential supercapacitor electrode material.

2.4. Conclusions

This study shows a potentially commercially viable method for the effective use of natural polymers such as CtNFs as carbon precursors for advanced carbon applications in energy storage and supercapacitor applications through more selective KOH activation, specifically targeting amorphous carbon. AHPC was successfully synthesized from TEMPO-oxidized, hydrothermally treated CtNFs by using a PSL template. The synthesis method of the material is relatively more facile than other methods, making it applicable for scalable production in order to meet future market demands. HT was found to affect the hydrochar structure via temperature-dependent fiber decomposition. The PSL amount affects the extent of mesopore formation while the carbonization temperature affects pore sintering. The degree of porosity of the carbonized materials after KOH activation was found to affect both the surface area and specific capacitance of the material. Enhanced mesoporosity resulted in increased micropore formation and exposure of edge sites. The optimized AHPC-P10C5 sample was found to be a promising supercapacitor material, exhibiting EDLC and C_{sp} reaching up to 567 F g^{-1} at a current density 0.5 A g^{-1}. At increased current density, AHPC-P10C5 had a capacitance retention of 73%, while after 2000 charge cycles at 5 A g^{-1} and 10 000 cycles at 10 A g^{-1}, C_{sp} was almost unchanged. This makes this material a viable alternative to nanocarbon-based materials for energy storage system and supercapacitor applications.

2.5. References

1] L. Gao, L. Xiong, D. Xu, J. Cai, L. Huang, J. Zhou, L. Zhang, *ACS Appl. Mater. Interfaces* **2018**, *10*, 28918–28927.

[2] J. Zhou, L. Bao, S. Wu, W. Yang, H. Wang, *Carbohydr. Polym.* **2017**, *173*, 321–329.

[3] K. Sakanishi, N. Ikeyama, T. Sakaki, M. Shibata, T. Miki, *Ind. Eng. Chem. Res.* **1999**, *38*, 2177–2181.

[4] S. Suenaga, M. Osada, *Cellulose* **2018**, *25*, 6873–6885.

[5] M. Genovese, H. Wu, A. Virya, J. Li, P. Shen, K. Lian, *Electrochim. Acta* **2018**, *273*, 392–401.

[6] C. Falco, J. P. Marco-Lozar, D. Salinas-Torres, E. Morallón, D. Cazorla-Amorós, M. M. Titirici, D. Lozano-Castelló, *Carbon N. Y.* **2013**, *62*, 346–355.

[7] Y. Kato, J. Kaminaga, R. Matsuo, A. Isogai, *Carbohydr. Polym.* **2004**, *58*, 421–426.

[8] Y. Fan, T. Saito, A. Isogai, *Biomacromolecules* **2008**, *9*, 192–198.

[9] M. A. Ferry, J. Maruyama, T.-A. Asoh, H. Uyama, *RSC Adv.* **2021**, *11*, 2202–2212.

[10] P. Li, C.-N. Feng, H.-P. Li, X.-L. Zhang, X.-C. Zheng, *J. Alloys Compd.* **2021**, *851*, 156922.

[11] S. Kubo, R. J. White, N. Yoshizawa, M. Antonietti, M.-M. Titirici, *Chem. Mater.* **2011**, *23*, 4882–4885.

[12] H. Su, J. Wang, L. Yan, *ACS Sustain. Chem. Eng.* **2019**, *7*, 18476–18482.

[13] X. Chai, H. He, H. Fan, X. Kang, X. Song, *Bioresour. Technol.* **2019**, *282*, 142–147.

[14] E. Savitri, Sumarno, A. Rosyadi, *Macromol. Symp.* **2015**, *353*, 212–219.

[15] A. M. Borrero-López, E. Masson, A. Celzard, V. Fierro, *Ind. Crops Prod.* **2018**, *124*, 919–930.

[16] T. M. Aida, K. Oshima, C. Abe, R. Maruta, M. Iguchi, M. Watanabe, R. L. Smith, *Carbohydr. Polym.* **2014**, *106*, 172–178.

[17] S. Suenaga, M. Osada, *ACS Appl. Polym. Mater.* **2019**, *1*, 1045–1053.

[18] A. Martínez Cortizas, O. López-Costas, *Sci. Rep.* **2020**, *10*, 17888.

[19] P. Köll, G. Borchers, J. O. Metzger, *J. Anal. Appl. Pyrolysis* **1991**, *19*, 119–129.

[20] A. L. Pauline, K. Joseph, *Fuel* **2020**, *279*, 118472.

[21] C. Matei Ghimbeu, V. A. Luchnikov, *Microporous Mesoporous Mater.* **2018**, *263*, 42–52.

[22] L. Chuenchom, R. Kraehnert, B. M. Smarsly, *Soft Matter* **2012**, *8*, 10801.

[23] X. Meng, H. Cui, J. Dong, J. Zheng, Y. Zhu, Z. Wang, J. Zhang, S. Jia, J. Zhao, Z. Zhu, *J. Mater. Chem. A* **2013**, *1*, 9469.

[24] X. Xie, B. Goodell, Y. Qian, M. Peterson, J. Jellison, *Holzforschung* **2008**, *62*, 591–596.

[25] X. L. Zhou, H. Zhang, L. M. Shao, F. Lü, P. J. He, *Waste and Biomass Valorization* **2021**, *12*, 1699–1724.

[26] W. W. Lukens, G. D. Stucky, *Chem. Mater.* **2002**, *14*, 1665–1670.

[27] R. Balgis, T. Ogi, A. F. Arif, G. M. Anilkumar, T. Mori, K. Okuyama, *Carbon N. Y.* **2015**, *84*, 281–289.

[28] R. Ji, S. Wei, Y. Xia, C. Huang, Y. Huang, H. Zhang, F. Xu, L. Sun, X. Lin, *J. Energy Storage* **2020**, *27*, 101134.

[29] S. Kubo, R. J. White, K. Tauer, M.-M. Titirici, *Chem. Mater.* **2013**, *25*, 4781–4790.

[30] J. Fang, B. Gao, A. R. Zimmerman, K. S. Ro, J. Chen, *RSC Adv.* **2016**, *6*, 24906–24911.

[31] J. Guo, A. Chong Lua, *J. Anal. Appl. Pyrolysis* **1998**, *46*, 113–125.

[32] M. Gehring, H. Tempel, A. Merlen, R. Schierholz, R.-A. Eichel, H. Kungl, *RSC Adv.* **2019**, *9*, 27231–27241.

[33] B. Saha, G. C. Schatz, *J. Phys. Chem. B* **2012**, *116*, 4684–4692.
[34] T. H. Ko, W. S. Kuo, Y. H. Chang, *J. Appl. Polym. Sci.* **2001**, *81*, 1084–1089.
[35] S. K. Hoekman, A. Broch, A. Warren, L. Felix, J. Irvin, *Biofuels* **2014**, *5*, 651–666.
[36] T. Gagić, A. Perva-Uzunalić, Ž. Knez, M. Škerget, *Ind. Eng. Chem. Res.* **2018**, *57*, 6576–6584.
[37] A. Bengtsson, P. Hecht, J. Sommertune, M. Ek, M. Sedin, E. Sjöholm, *ACS Sustain. Chem. Eng.* **2020**, *8*, 6826–6833.
[38] A. C. Ferrari, J. Robertson, *Phys. Rev. B - Condens. Matter Mater. Phys.* **2001**, *64*, 1–13.
[39] J. McDonald-Wharry, M. Manley-Harris, K. Pickering, *Carbon N. Y.* **2013**, *59*, 383–405.
[40] J. Maruyama, S. Maruyama, T. Fukuhara, T. Nagaoka, K. Hanafusa, *Beilstein J. Nanotechnol.* **2019**, *10*, 985–992.
[41] J. Maruyama, S. Maruyama, T. Fukuhara, K. Hanafusa, *J. Phys. Chem. C* **2017**, *121*, 24425–24433.
[42] J. Huang, Y. Liang, H. Hu, S. Liu, Y. Cai, H. Dong, M. Zheng, Y. Xiao, Y. Liu, *J. Mater. Chem. A* **2017**, *5*, 24775–24781.
[43] D. Arvind, G. Hegde, *RSC Adv.* **2015**, *5*, 88339–88352.
[44] A. G. Pandolfo, A. F. Hollenkamp, *J. Power Sources* **2006**, *157*, 11–27.
[45] A. Eftekhari, Z. Fan, *Mater. Chem. Front.* **2017**, *1*, 1001–1027.
[46] J. A. Fernández, S. Tennison, O. Kozynchenko, F. Rubiera, F. Stoeckli, T. A. Centeno, *Carbon N. Y.* **2009**, *47*, 1598–1604.
[47] J.-P. Randin, E. Yeager, *J. Electroanal. Chem. Interfacial Electrochem.* **1972**, *36*, 257–276.
[48] M. Velický, P. S. Toth, C. R. Woods, K. S. Novoselov, R. A. W. Dryfe, *J. Phys. Chem. C* **2019**, *123*, 11677–11685.

Chapter 3

Facile synthesis of templated activated carbon from cellulose nanofibers and MgO nanoparticles *via* integrated carbonization-activation method as an eco-friendly supercapacitor

3.1. Introduction

Due to the shift towards sustainable production of carbon materials, biomass-based activated carbon (AC) for supercapacitor electrode applications that use less energy-intensive synthesis methods as well as utilize sustainably sourced raw resources have garnered attention in recent years.[1] AC synthesis starts with carbon materials as its precursor that is mixed with an activating agent such as KOH,[2,3] or CO_2,[4] to be heated at higher temperatures.[5] When starting from biomass, the synthesis process becomes long and energy-intensive because converting biomass to activated carbon would then take 2 heat treatment steps, thus making biomass-based AC production less environmentally friendly. An alternative and more eco-friendly method is performing both carbonization and activation within one heat treatment cycle.[6,7] AC synthesized *via* one-step carbonization-activation has been reported to have nearly identical or had higher surface area than that of AC synthesized through the conventional two-step method.[8,9]

In Chapters 1 and 2, nanofibers were hydrothermally treated to induce crosslinking to fully stabilize PSL within the hydrochar matrix. The long process of precursor treatment like the carbonization treatment discussed prior is also energy-intensive. Thus, direct conversion of cellulose to carbon while performing nanoparticle templating would allow not only the raw materials but the fabrication process eco-friendly as well. One challenge however is that PSL as a template requires hydrothermal treatment to be compatible with nanofibers. Meanwhile, metal oxides (MOx) such as SiO_2,[10] zeolites,[11] ZnO,[12] and MgO[13,14] that range from

nanospheres to nanorods, are more mechanically and thermally stable than polymer NPs, and do not need additional interface stabilizers. MOx NPs could then easily be removed by washing the carbon material in acid such as HCl.[15]

Thus, in this work, an optimized, green, and facile synthesis method for templated activated carbon (TAC) from TEMPO-oxidated cellulose nanofibers (TOCN) with dispersed 50nm MgO NPs and KOH *via* an integrated MgO drying and one-step carbonization-activation heat treatment method is presented (**Scheme 3-1**). The effects of mesopore and micropore-inducing agents MgO and KOH, and activation temperature, were investigated and optimized. The electrochemical properties of TAC was then evaluated to determine its potential as a potential eco-friendly supercapacitor electrode material.

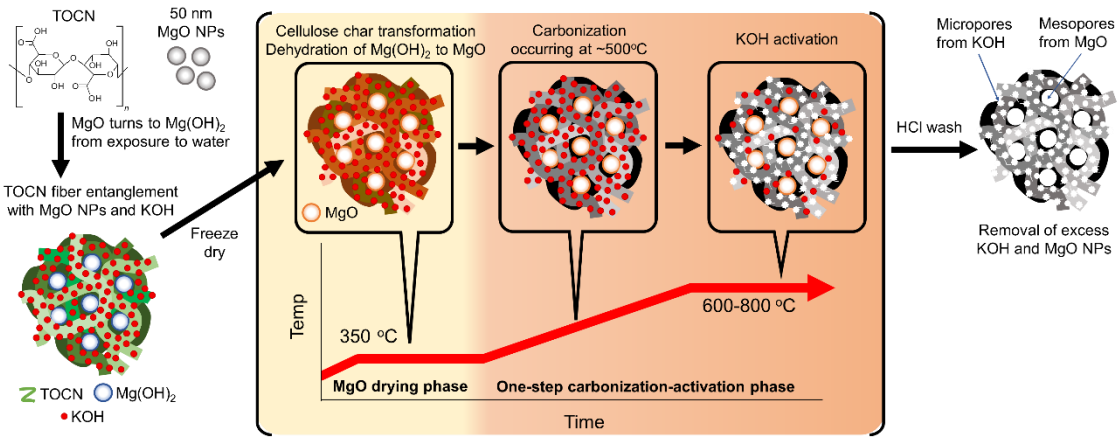

Scheme 3-1. Synthesis of TACs *via* continuous, one-step carbonization activation of TOCN.

3.2. Experimental Section

3.2.1. Materials

The list of reagents used are as follows: cellulose powder (Nacalai Tesque), TEMPO (Tokyo Chemical Industry), sodium bromide (Sigma-Aldrich), 8.5-13.5 % sodium hypochlorite solution (Nacalai Tesque), 0.5 mol/L NaOH solution (Sigma-Aldrich), 99.9 % 0.05µm magnesium oxide (Wako Pure Chemical Corporation), potassium hydroxide pellets (Wako Pure

Chemical Corporation), hydrochloric acid (Wako Pure Chemical Corporation) 0.8 % Nafion solution prepared from 5 % Nafion solution (Wako Pure Chemical Corporation) diluted with isopropanol, carbon black (Strem Chemicals. Inc.), and sulfuric acid (Wako Pure Chemical Corporation). All reagents were used as received.

3.2.2. Synthesis of Templated Activated Carbons (TAC)

In a typical synthesis, 10 g of TOCN dispersion (corresponding to 100 mg dry cellulose), MgO with average size 52.6 ± 5.9 nm (Fig. S1), KOH, and water for a total volume of 15 mL were placed in a 50 mL conical tube, and shaken until the KOH was fully dissolved, and the MgO was homogeneously dispersed. The mixture was freeze-dried for 48 h, yielding cellulose monoliths (CM). CMs were then loaded into an electric furnace under Ar atmosphere with a constant Ar flow rate of 300 mL min^{-1}. The heat treatment was performed as follows: using a heating rate of 5 ^{o}C min^{-1}, the temperature was raised to 350 ^{o}C and held for 1 h, followed by a heating rate of 10 ^{o}C min^{-1} to raise the temperature to 800 ^{o}C held for 1.5 h. The samples were then cooled slowly overnight. The activated carbon with MgO were washed with 6 mol L^{-1} hydrochloric acid to remove excess KOH as well as dissolve the MgO template, forming TACs. The TACs were washed with water until neutral pH, and dried in an oven at 85 ^{o}C overnight. The list of experiments and their corresponding conditions are listed in **Table 3-1**.

Table 3-1. List of experiments performed and the TAC label code for the corresponding conditions with constant 100 mg TOCN content.

Code	Mass of KOH / mg	Mass of MgO / mg	Activation Temperature / ^{o}C
Studies on the effect of MgO and KOH on pore formation			
KxM30	-	300	800
K5Mx	50	-	800
Variation of KOH amount			
K2	20	100	800
K5 (=M10)	50	100	800
K7	70	100	800
K10	100	100	800
Variation of MgO amount			
M5	50	50	800
M10 (=K5)	50	100	800
M30 (=C800)	50	300	800
M50	50	500	800
Variation of Activation Temperature			
C600	50	300	600
C700	50	300	700
C800 (=M30)	50	300	800

3.2.3. Characterization

Scanning Electron Microscopy (SEM) micrographs were taken using a Hitachi SU3500 microscope. Thermogravimetric analysis (TGA) was conducted using a SII TG/DTA7200 instrument. Brunauer-Emmett-Teller (BET) surface area analysis was performed using a Quantachrome NOVA 4200e Surface Area & Pore Size Analyzer. Barrett-Joyner-Halenda (BJH) and Density Functional Theory (DFT) pore size analysis methods were also performed through the same software used for the BET. All samples were vacuum dried at 90^{o}C for 24h prior to analysis. X-ray Photoelectron Spectroscopy (XPS) spectra were taken using a JEOL JPS-9010MC XPS instrument with monochromatic AlKα-radiation. CasaXPS Version 2.3.15 was used in analyzing the C1s narrow XPS profile. Raman spectrographs were taken using a Jasco NRS-3100 Laser Raman Spectrophotometer (532.190 nm).

3.2.4. Electrochemical Studies

A three-electrode system was used to measure the electrochemical specific capacitance of TACs. The system consisted of an Ag|AgCl reference electrode (RE-1B, BAS) with an internal solution of 3 mol L^{-1} NaCl, a Pt wire counter electrode, and a glassy carbon electrode (diameter = 3 mm, BAS), with TAC-based carbon as the working electrode, and a 1 mol L^{-1} sulfuric acid solution as the electrolyte. The working electrode was prepared by first grinding 200 mg TAC into a powder ($d \leq 45$ μm), then dispersing the TAC powder, and 5 wt% carbon black in a 0.8 % Nafion and isopropanol solution to obtain a 30 mg mL^{-1} casting solution. 1.5 μL of the solution was cast on the glassy carbon part of the electrode, and then air-dried for 24 h to give a total TAC loading mass of 45 μg and an average disc thickness of 12.7 ± 4.2 μm. Prior to measurement, the working electrode was immersed in the electrolyte solution and placed under vacuum at 5 min intervals five times to ensure deep penetration of the electrolyte and the removal of bubbles on the electrode surface. The entire system was purged with Ar and kept at a constant temperature of 25°C throughout the measurement. All measurements were performed using an ALS/CH Model 600 electrochemical analyzer, with the program ALS/CH 7002e used for data collection.

CV was performed at varying scan rates (50, 100, 200, 300, 500 mV s^{-1}) with a potential window of -0.2-0.8 V and a rate of 10 cycles per scan. GCD measurements were performed at varying current densities i_m (0.5, 1, 2, 3, 4, 5 A g^{-1}), with a potential window of -0.2-0.8 V. Because all samples exhibited near-linear charge-discharge behavior, specific capacitance C_{sp} was calculated from the GCD spectra using the equation below (**Equation 3-1**),

$$C_{sp} = (I \times \Delta t)/(\Delta V \times m) = i_m \times \Delta t \qquad \textbf{(Equation 3-1)}$$

where I is the current (A), Δt is the time for one charge cycle (s), ΔV is the voltage range (V), and m is the mass of the active material (g). The equation can be further simplified to Δt multiplied by i_m, because the potential window is 1.0 V.

3.3. Results and Discussion

3.3.1. Characterization

Even though only one continuous heat treatment is performed on the CMs, a number of transformations occur to form TAC. Using TGA (**Figure 3-1**), it was determined that TOCN undergoes the dehydration at 219 °C,[16] then subsequent degradation at 316 °C and 363 °C.[17,18] MgO dispersed in TOCN turned into $Mg(OH)_2$, which then underwent dehydration at 209 °C and 363 °C to form back into MgO (**Figure 3-1**B).[19] Mass loss from further pyrolysis occurs at 448 °C, and lastly 715 °C mass loss from KOH activation through gaseous evolution of CO_2 and K_2O[20] also shown in the thermal decomposition TGA of KOH (**Figure 3-1**C).

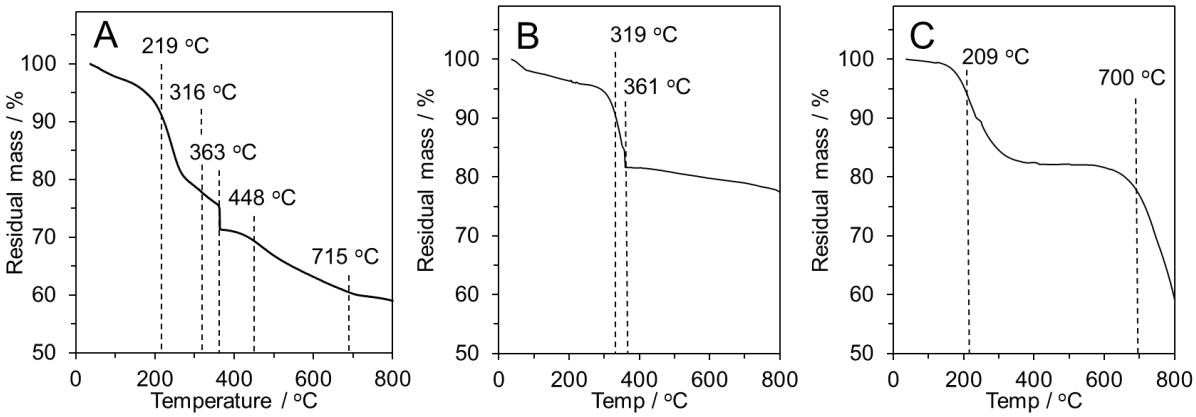

Figure 3-1. TGA curve of A) TAC-K5, B) MgO, and C) KOH.

To determine the effect of MgO and KOH on the pore formation mechanism of TAC, samples with no MgO (TAC-K5Mx) and no KOH (TAC-KxM30) were synthesized. From the SEM micrographs, TAC-K5Mx showed macropores (**Figure 3-2**A) naturally forming from carbonized TOCN, but not mesopores. Meanwhile, the addition of MgO with TAC-KxM30 (**Figure 3-2**B) resulted in the formation of mesopores, but no macropores were present in TAC-K5Mx. The BET curves of both samples are in agreement with the SEM (**Figure 3-2**C) as

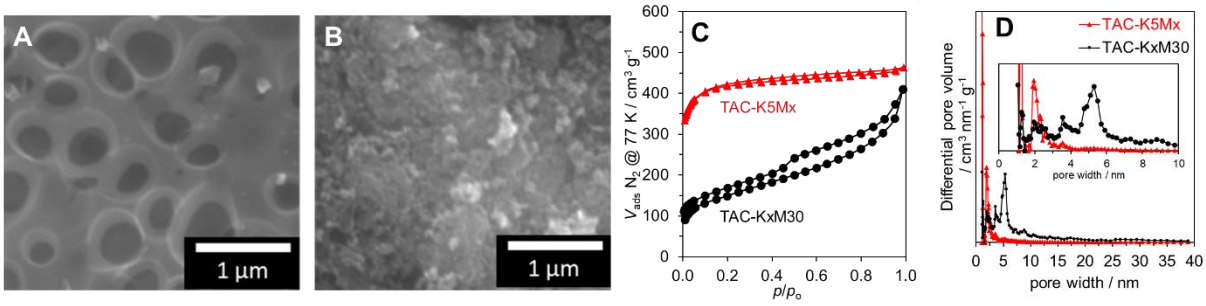

Figure 3-2. SEM micrographs of A) TAC-K5Mx and B) TAC-K5M30 and the corresponding C) BET curves and D) DFT pore size distribution.

shown by the significant difference in the absorbed N_2 at the 0.0-0.2 p/p_o region, and the lack of a hysteresis loop for TAC-K5Mx. The DFT distribution (**Figure 3-2**D) also highlights that TAC-KxM30 does not have any significant degree of microporosity. The small degree of microporosity observed for TAC-KxM30, evidenced by BJH micropore volume (V_{micro}) at 0.18 cm^3 g^{-1} is likely the effect of carbonizing TAC-KxM30 at 800 ^{o}C, resulting in some micropore formation.

3.3.2. Effect of KOH and MgO

Effect of KOH

After confirming that the pore formation mechanism of KOH and MgO are mutually exclusive, the amount of each pore inducing agent was optimized. The amount of KOH was adjusted to 20-100 mg, which was determined by predicting the eventual KOH:carbon impregnation ratio.[6,21] Studies that perform carbonization and activation separately have commonly reported using 1:1 to 4:1 KOH:carbon.[6,22] Because the average CM mass yield from 100 mg TOCN is 20 ± 4 mg, the amount of KOH was adjusted to 20, 50, 70, and 100 mg corresponding to 1:1, 2.5:1, 3.5:1, and 5:1 KOH:carbon.

As shown in the SEM micrographs (**Figure 3-3**A-D), the effect of KOH on both micro- and mesopore structure is dependent on the amount of KOH. TAC-K2 and TAC-K5 show a

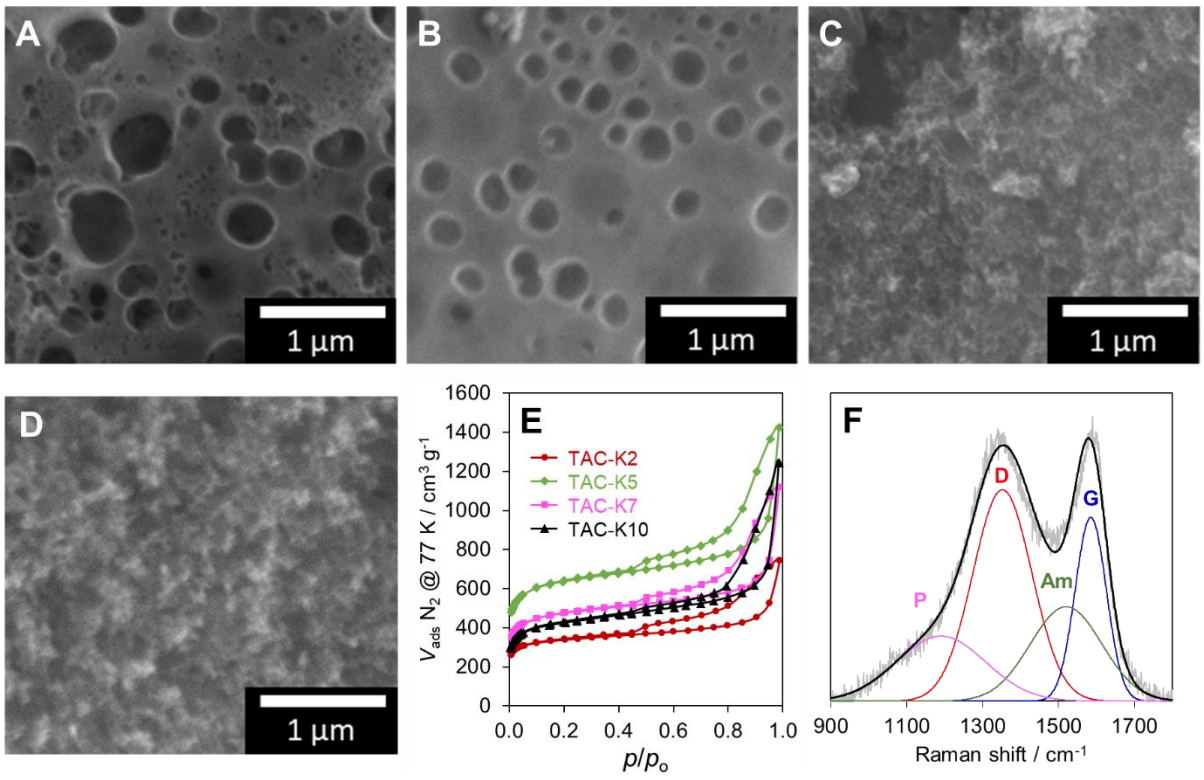

Figure 3-3. SEM micrographs of A) TAC-K2, B) TAC-K5, C) TAC-K7, and D) TAC-K10, and their respective E) BET curves. F) Raman spectra of TAC-K5.

similar morphology as that of TAC-K5Mx (**Figure 3-3**A, B), thus KOH does not contribute to meso-macropore formation. When the KOH amount is increased to 70-100 mg (TAC-K7 and TAC-K10, respectively), the surface morphology exhibits a porous structure (**Figure 3-3**C, D) which was likely formed as excessive amounts of KOH led to formation of KOH crystals that then served as another templating material.[23] This is evidenced by the increase in the meso-macropore volume ($V_{meso-macro}$) from 70.0 % of TAC-K5 to 73.5 % and 73.9 % of TAC-K7 and TAC-K10, respectively (**Table 3-2**). However, excessive template loading leads to pore and network collapse,[16] resulting in lower surface area (S_{BET}) from 1611 m^2 g^{-1} (TAC-K5) to 1407 m^2 g^{-1} (TAC-K10). Signs of pore uniformity were also seen in the BET curves (**Figure 3-3**E), as shown by TAC-K2 and TAC-K5 exhibiting Type IV H1/3 hysteresis loop. TAC-K7 and TAC-K10 meanwhile exhibit a Type IV H3 hysteresis loop, indicating less pore uniformity.

Table 3-2. S_{BET}, BJH pore volume analysis, and XPS elemental composition of TAC with varying amounts of KOH.

Sample	S_{BET} / $m^2\ g^{-1}$	BJH V_{total} / $cm^3\ g^{-1}$	BJH V_{micro} / $cm^3\ g^{-1}$	%	BJH $V_{meso-macro}$ / $cm^3\ g^{-1}$	%	XPS C at%	O at%	O/C
TAC-K2	1102	0.97	0.29	29.6	0.68	70.4	86.35	13.65	0.158
TAC-K5	1611	1.88	0.56	30.0	1.32	70.0	88.07	11.93	0.135
TAC-K7	1560	1.46	0.39	26.5	1.08	73.5	86.24	13.76	0.160
TAC-K10	1407	1.85	0.48	26.1	1.36	73.9	86.69	13.31	0.154

TAC-K5 also has a S_{BET} of 1611 $m^2\ g^{-1}$ (**Table 3-2**). To prevent uncontrolled secondary templating while still having the highest S_{BET}, 50 mg KOH was selected as the optimal KOH amount.

Varying the amount of KOH from the tested range does not seem to have a clear effect on the ratios of the carbon phases observed via Raman spectroscopy. Peak fitting of the Raman spectra for TAC-K5 (**Figure 3-3**F) however, shows that TAC shows a relatively high degree of amorphousness as observed from the P-band (1190 cm^{-1}) and Am-band (1520 cm^{-1}). All TAC samples had similar values for I_D/I_G, as well as I_P/I_G and I_{Am}/I_G, indicating that both graphitic and amorphous sections of TAC were unaffected.

The same observation as made using XPS, where the relative C % and O % did not vary (**Table 3-2**) despite higher amounts of KOH. Analysis of both C1s and O1s narrow spectra likewise show similar ratios for all deconvoluted peaks.

Effect of MgO

Increasing the amount of MgO results in higher degree of mesoporosity. SEM micrographs of TAC-M5 to TAC-M50 (**Figure 3-4**A-C) show an increasing number of pores made by MgO especially with honeycomb-like porosity for TAC-M30 (**Figure 3-4**B). The DFT pore size distributions (**Figure 3-4**D) confirm the increase in mesoporosity as a result of increased MgO loading. The mesopores range from the size of 5-30 nm, and all peaks

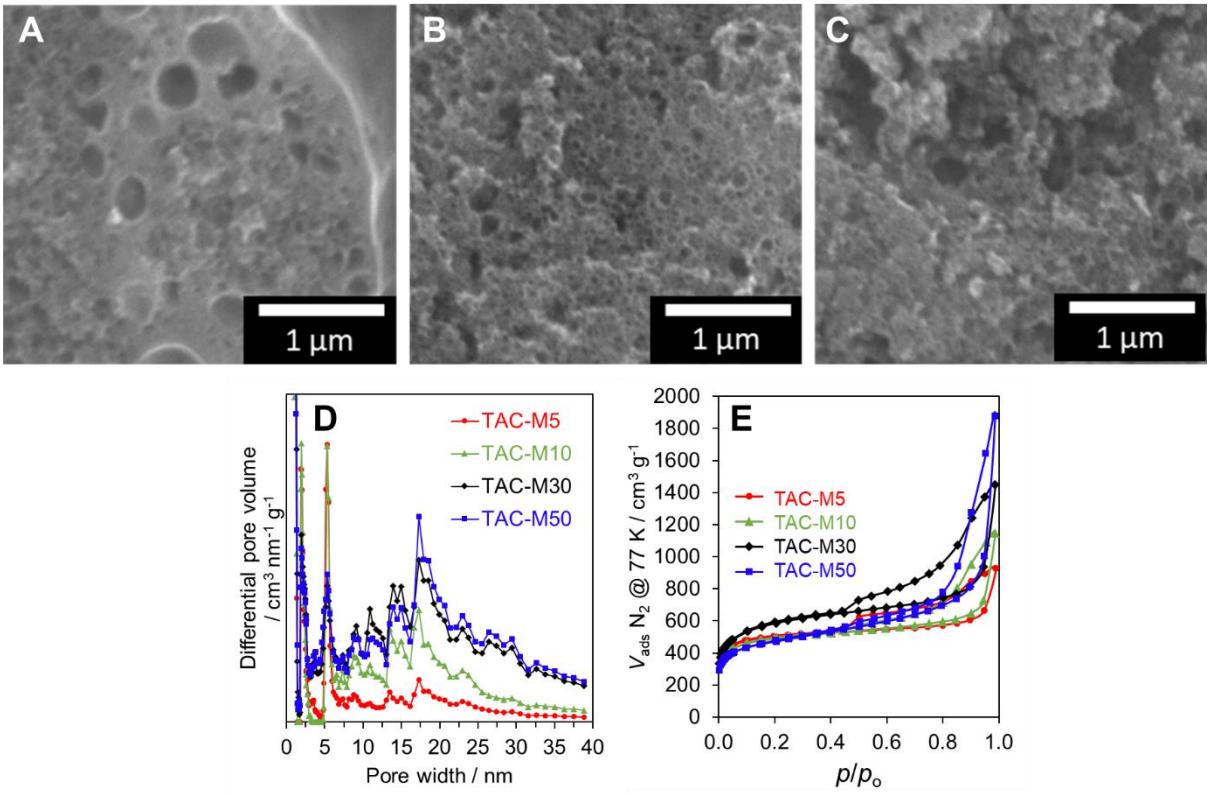

Figure 3-4. SEM micrographs of a) TAC-M5, b) TAC-M30, and c) TAC-M50, and their respective d) BET curves and e) DFT pore size plots. Note that TAC-M10 is the same as TAC-K5.

consistently grow in proportion to the amount of MgO. However, the pore distribution curve peaks of TAC-M30 and TAC-M50 having similar intensities indicate that the degree of mesoporosity does not further increase when over-templating occurs. The BET curves (**Figure 3-4**E) likewise show a similar increase in the size of the hysteresis loop at the 0.5-1.0 p/p_o region. The 0-0.2 p/p_o region of **Figure 3-4**D however does not change, again showing that MgO does not affect microporosity. The optimal amount of MgO that could be loaded into TOCN is observed to be at 300 mg, with the highest SBET observed at 1711 m^2 g^{-1} (**Table 3-3**). V_{total} and $V_{meso\text{-}macro}$ increases proportionally with MgO amount, but template overloading occurred at 500 mg as shown by the disappearance of a clear pore structure (**Figure 3-4**C) and decrease in S_{BET} for TAC-M50.

Table 3-3. S_{BET}, BJH pore volume analysis, and XPS elemental composition of TAC with varying amounts of MgO.

Sample	S_{BET} / $m^2\ g^{-1}$	BJH V_{total} / $cm^3\ g^{-1}$	BJH V_{micro} / $cm^3\ g^{-1}$	%	BJH $V_{meso-macro}$ / $cm^3\ g^{-1}$	%	XPS C at%	O at%	O/C
TAC-M5	1626	1.15	0.44	37.9	0.72	62.1	83.46	16.54	0.198
TAC-M10	1611	1.88	0.56	30.0	1.32	70.0	88.07	11.93	0.135
TAC-M30	1711	2.80	0.60	21.4	2.20	78.6	84.99	15.01	0.177
TAC-M50	1574	2.92	0.58	19.9	2.34	80.1	87.34	12.66	0.145

Similar to that of KOH, the amount of MgO did not have a clear effect on the I_D/I_G ratio of the TAC samples, while there is an increase in the amount of amorphous carbon from TAC-M5 to TAC-M30 evident from the I_P/I_G and I_{Am}/I_G peaks. The values for all Raman bands begin to plateau with TAC-M50, indicating that above 300 mg, MgO starts to affect only the surface area. Likewise, the amount of MgO does not have a clear effect on the elemental composition of TAC, as shown in the XPS elemental composition C at% and O at% (**Table 3-3**), but the increased mesoporosity resulted in the slight increase of C=O bond formation as seen in the C1s narrow spectra rising from 17.7 % of TAC-M5 to 31.2 % of TAC-M30.

3.3.3. Effect of Activation Temperature

After optimizing the amount of KOH and MgO, the effect of activation temperature on TAC-M30 was investigated. The mesopore structure of TAC treated from 600-800^{o}C remained the same when observed with SEM (**Figure 3-5**A and B, **Figure 3-4B**). S_{BET} however significantly increased from 731 $m^2\ g^{-1}$ of TAC-C600 to 1711 $m^2\ g^{-1}$ of TAC-C800 (**Figure 3-5**C, **Table 3-4**). Likewise, V_{total}, V_{micro}, and $V_{meso-macro}$ all increased for TAC-C800, while the relative ratio of V_{micro} to $V_{meso-macro}$ stayed the same. Therefore, the overall porosity of TAC is affected by the final hold temperature of the heat treatment. DFT pore distribution also shows

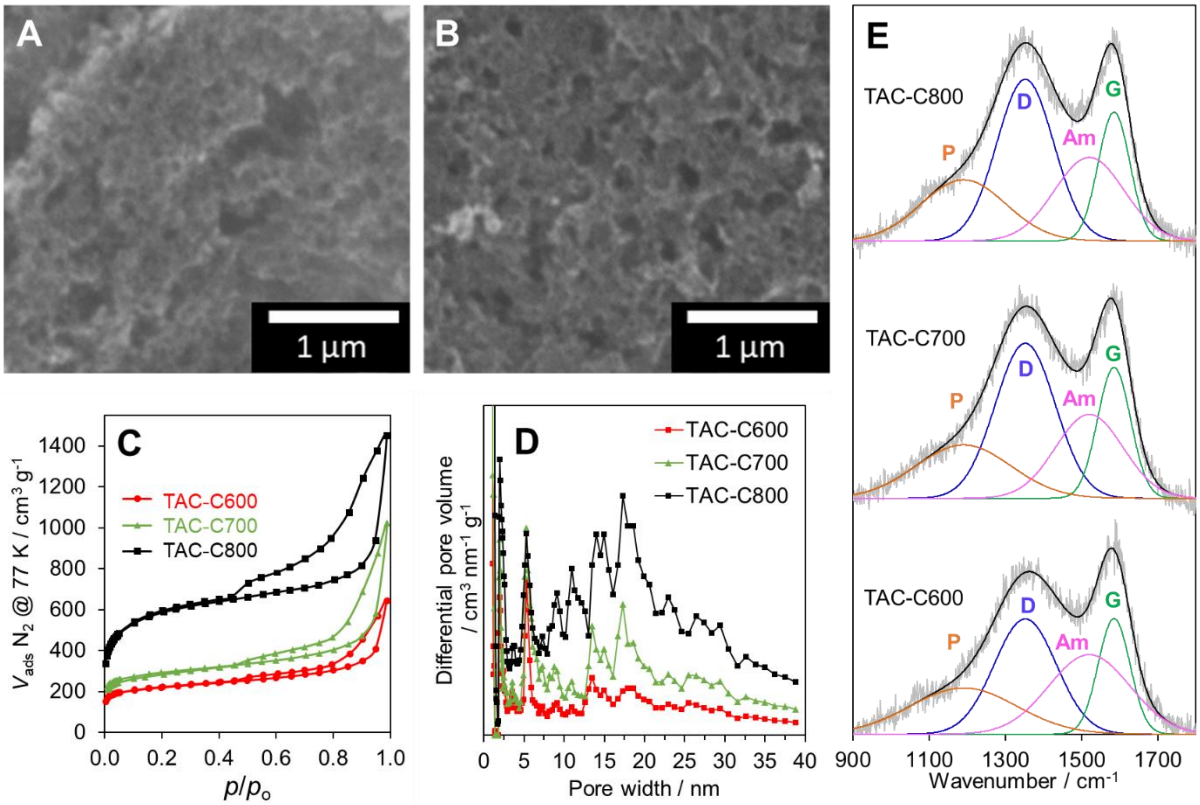

Figure 3-5. SEM micrographs of a) TAC-C600 and b) TAC-C700. TAC-C600 to TAC-C800 characterization through c) BET, d) DFT pore size distribution, and e) Raman spectra. Note that TAC-C800 is the same as TAC-M30.

the same trend with all peaks increasing with higher temperature (**Figure 3-5**D). The increase in microporosity (**Figure 3-5**C) can be explained by the temperature-dependent reactions of KOH that results in surface etching. Below 700ºC KOH forms K_2O and K_2CO_3,[24] but reactions where K_2CO_3 react with more carbon to form CO or CO_2 only occur above 700ºC, thus etching the surface to form the micropores.[5] Activation further progresses with higher temperature, shown by TAC-C800 having the highest surface area.

Higher activation temperature also resulted in the increase in I_D/I_G ratio (**Figure 3-5**E) from the increasing D-band. This could either indicate that more edge sites of the graphitic basal plane are being exposed,[25] or that there is an increasing number of defects on the basal

Table 3-4. S_{BET}, BJH pore volume analysis, and XPS elemental composition of TAC activated at varying temperatures.

Sample	S_{BET} /	BJH V_{total} /	BJH V_{micro} /		BJH $V_{meso-macro}$ /		XPS		
	$m^2\ g^{-1}$	$cm^3\ g^{-1}$	$cm^3\ g^{-1}$	%	$cm^3\ g^{-1}$	%	C at%	O at%	O/C
TAC-C600	731	0.957	0.24	25.2	0.72	74.8	83.46	16.54	0.198
TAC-C700	1196	1.653	0.31	19.0	1.34	81.0	88.07	11.93	0.135
TAC-C800	1711	2.798	0.60	21.4	2.20	78.6	84.99	15.01	0.177

plane from increased KOH etching. The relative phases of amorphous carbon associated with the I_P/I_G and I_{Am}/I_G are similar for TAC-C700 and TAC-C800.

The elemental composition of the TAC did not change significantly despite the elevated activation temperature (**Table 3-4**). Slight decrease in O content, possibly from the evolution of CO and CO_2 during activation, was observed. Higher ratios of C=O and lower C-O percent for TAC-C700 and TAC-C800 compared to TAC-C600 indicate oxidation as the primary route for O release at high temperature.

3.3.4. Electrochemical Studies

The performance of TACs activated at different temperatures as potential supercapacitors were studied. From the CV curves in **Figure 3-6**A-C, electrochemical capacitance increased with increasing temperature like from the following factors: 1) increase in S_{BET}, 2) better-developed hierarchical porosity, and 3) exposure of edge sites during highest S_{BET} among all TAC samples, and has both optimized KOH and MgO amounts, resulting in a well-developed pore structure, resulting in a very high capacitance of 269 F g^{-1} at 0.5 A g^{-1}. The increased number of edge sites from higher activation temperature, indicated by Raman spectroscopy, could also explain the trend in increasing specific capacitance. A study by Randin et al.[26] reported that edge site capacitance is higher (50-70 μF cm^{-2}) compared to the basal plane (16 μF cm^{-2}). The difference is apparent between TAC-C600 and TAC-C700, with I_D/I_G increasing from 0.997 to 1.184, respectively. Compared to that of TAC-C600, TAC-C700 also

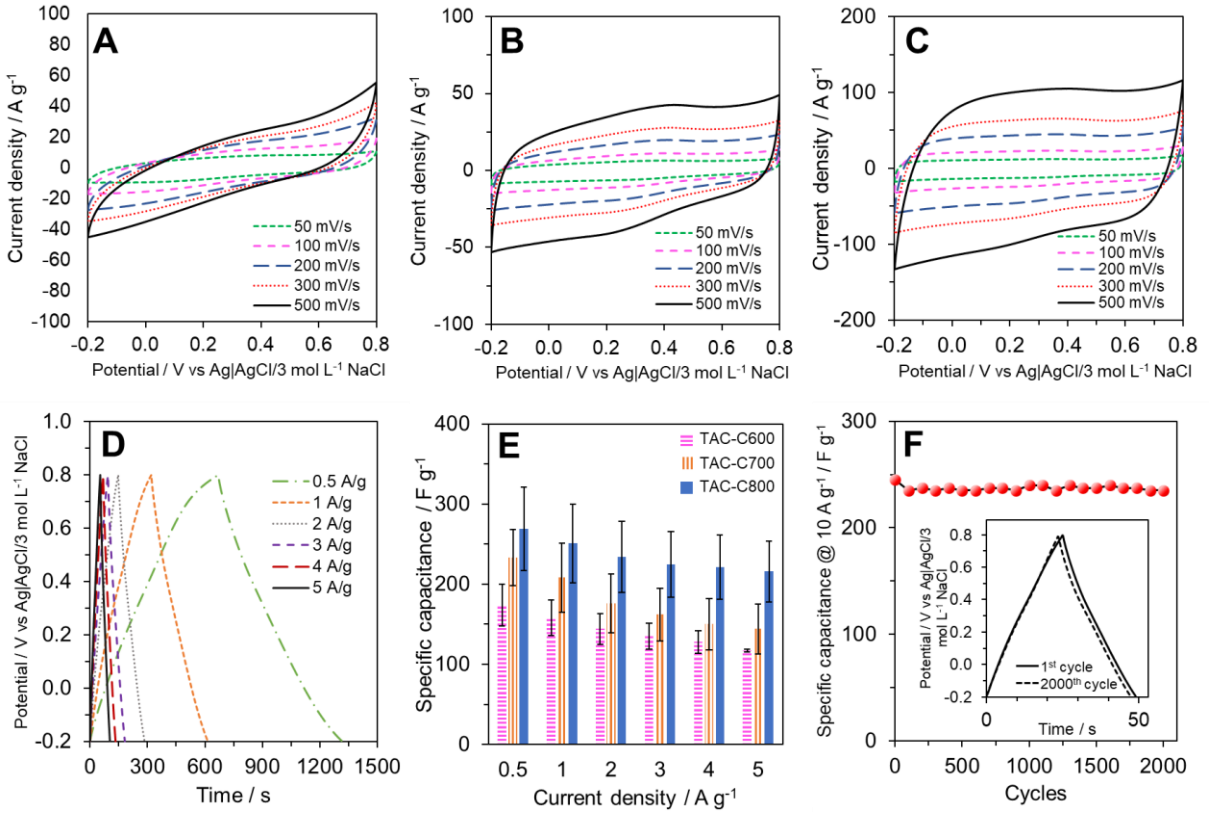

Figure 3-6. CV curves of A) TAC-C600, B) TAC-C700, and C) TAC-C800 ay scan rates from 50-500 mV s^{-1}. D) specific capacitance of TAC-C600, TAC-C700, and TAC-C800 at various current densities. E) GCD plots of TAC-C800 at various current densities. F) cycle stability plot of TAC-C800 measured at 10 A g^{-1}.

had more rectangular voltammogram shape, indicating stable charge-discharge behavior desired in supercapacitor materials. The difference in the I_D/I_G between TAC-C700 and TAC-C800 is smaller, and both samples exhibited good charge-discharge behavior, thus the difference in specific capacitance between TAC-C700 and TAC-C800 could be better explained by the increase in surface area and pore volume instead (**Table 3-4**). Both samples exhibited stable CV curves from 50-500 mV s^{-1} (**Figure 3-6**). Despite the different charge-discharge behavior observed in CV for TAC-C600, all samples had stable GCD curves (**Figure 3-6**D,

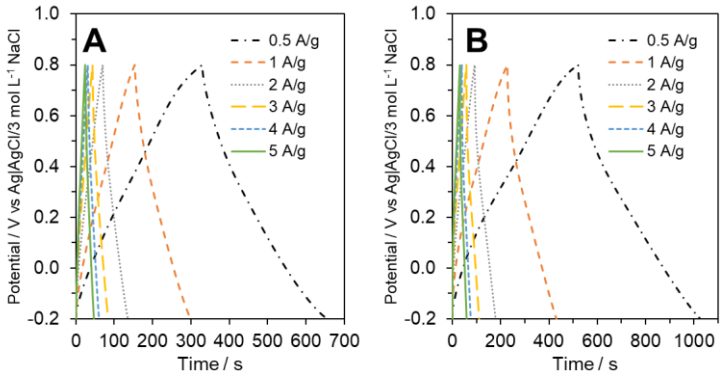

Figure 3-7. GCD curves of a) TAC-C600 and b) TAC-C700 at varying current densities.

Figure 3-7A, B) at 0.5-5 A g^{-1}. TAC-C600 however had the least stable charge-discharge behavior (**Figure 3-6**A). All TAC had no ion impurities such as residual K^{+} or Mg^{2+} ions that could influence the measured specific capacitance, as confirmed from the lack of peaks on both the XPS wide and narrow spectra.

Measuring the specific capacitance of all samples at increasing current density (**Figure 3-6**E) showed that TAC-C600 decreased to 117 F g^{-1} at 5 A g^{-1}, which corresponded to a capacitance retention of 67.2 %. TAC-C700 had a capacitance drop to 144 F g^{-1} and a capacitance retention of 61.8 %. TAC-C800 on the other hand had a much higher capacitance retention of 80.3 %, dropping only to 216 F g^{-1} at 5 A g^{-1}. TAC-C800 cycle stability was further evaluated by repeating 2000 charge-discharge cycles at 10 A g^{-1} (**Figure 3-6**F), and showed that TAC-C800 still had a cycle stability of 95.92 %. The first and 2000th cycles were also nearly identical, indicating no decrease in the charge-discharge stability.

To confirm the synergistic effect of pore formation by MgO and KOH in TAC, the electrochemical properties of TAC-K5x and TAC-KxM30 were also evaluated to compare with TAC-C800 (**Figure 3-8**). Due to not having a well-developed micropore structure, TAC-KxM30 did not exhibit high specific capacitance as evidenced by the small area of the CV

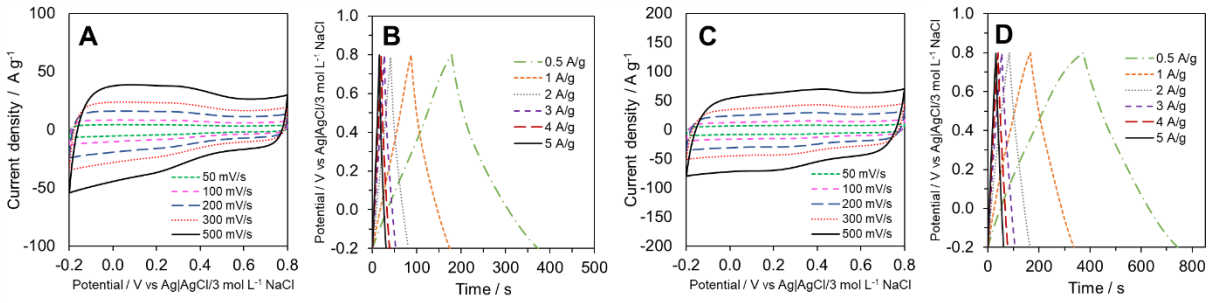

Figure 3-8. CV and GCD curves for TAC-KxM30 (a, b), and TAC-K5Mx (c, d), respectively.

curves. There was also uneven charge-discharge behavior (**Figure 3-8**A), which is not optimal for the operational electrical output demanded from supercapacitor electrode materials. The same observation could be said about the GCD curves (**Figure 3-8**B), and the calculated C_{sp} of TAC-KxM30 is only 92.8 F g^{-1} at 0.5 A g^{-1}. Meanwhile, TAC-K5Mx had much more stable charge-discharge behavior across all scan rates (**Figure 3-8**C), but due to the lack of the mesopores both S_{BET} and electrolyte penetration are lower compared to TAC-K5M30. This reflected in the GCD curves (**Figure 3-8**D), and the calculated C_{sp} at 0.5 A g^{-1} was 185.4 F g^{-1}.

3.4. Conclusions

This study presented a facile and eco-friendly method of utilizing TEMPO-oxidized cellulose nanofibers to stabilize MgO NPs as the carbon precursor for KOH-activated AC *via* an integrated MgO drying, carbonization, and activation heat treatment method. It was shown that KOH and MgO contribute to the formation of a hierarchical porous structure through different mechanisms that do not affect one another. Activation temperature affected the overall pore formation process. Due having excellent surface area, pore volume, and graphene basal plane edge site exposure, TAC-C800 exhibited high specific capacitance of 269 F g^{-1} at 0.5 A g^{-1} with good capacitance retention of 80.3 % when current density was increased to 5 A g^{-1}. Cycle stability of 95.92 % was observed even after undergoing 2000 charge-discharge cycles at 10 A g^{-1}, therefore making TAC-C800 a viable material for supercapacitor applications.

3.5. References

[1] P. González-García, *Renew. Sustain. Energy Rev.* **2018**, *82*, 1393–1414.
[2] B. Chang, B. Yang, Y. Guo, Y. Wang, X. Dong, *RSC Adv.* **2015**, *5*, 2088–2095.
[3] B. Ding, S. Huang, K. Pang, Y. Duan, J. Zhang, *ACS Sustain. Chem. Eng.* **2018**, *6*, 177–185.
[4] A. Dobashi, J. Maruyama, Y. Shen, M. Nandi, H. Uyama, *Carbohydr. Polym.* **2018**, *200*, 381–390.
[5] Z. Heidarinejad, M. H. Dehghani, M. Heidari, G. Javedan, I. Ali, M. Sillanpää, *Environ. Chem. Lett.* **2020**, *18*, 393–415.
[6] G. Lin, R. Ma, Y. Zhou, Q. Liu, X. Dong, J. Wang, *Electrochim. Acta* **2018**, *261*, 49–57.
[7] Y. Jiang, Z. He, X. Cui, Z. Liu, J. Wan, Y. Liu, F. Ma, *New J. Chem.* **2022**, 6078–6090.
[8] Y. Wang, J. Cui, Q. Qu, W. Ma, F. Li, W. Du, K. Liu, Q. Zhang, S. He, C. Huang, *Microporous Mesoporous Mater.* **2022**, *329*, 111545.
[9] O. Oginni, K. Singh, G. Oporto, B. Dawson-Andoh, L. McDonald, E. Sabolsky, *Bioresour. Technol. Reports* **2019**, *7*, 100266.
[10] H. Li, Y. Zhao, S. Liu, P. Li, D. Yuan, C. He, *Microporous Mesoporous Mater.* **2020**, *297*, 109960.
[11] H. Noh, S. Choi, H. G. Kim, M. Choi, H.-T. Kim, *ChemElectroChem* **2019**, *6*, 558–565.
[12] H. Wang, S. Yu, B. Xu, *Chem. Commun.* **2016**, *52*, 11512–11515.
[13] E. Unur, S. Brutti, S. Panero, B. Scrosati, *Microporous Mesoporous Mater.* **2013**, *174*, 25–33.
[14] T. Morishita, Y. Soneda, T. Tsumura, M. Inagaki, *Carbon N. Y.* **2006**, *44*, 2360–2367.
[15] S. Li, X. Song, X. Wang, C. Xu, Y. Cao, Z. Xiao, C. Qi, M. Wu, Z. Yang, L. Fu, X. Ma, J. Gao, *Carbon N. Y.* **2020**, *160*, 176–187.
[16] M. A. Ferry, J. Maruyama, T.-A. Asoh, H. Uyama, *RSC Adv.* **2021**, *11*, 2202–2212.
[17] P. Köll, G. Borchers, J. O. Metzger, *J. Anal. Appl. Pyrolysis* **1991**, *19*, 119–129.
[18] S. D. Stefanidis, K. G. Kalogiannis, E. F. Iliopoulou, C. M. Michailof, P. A. Pilavachi, A. A. Lappas, *J. Anal. Appl. Pyrolysis* **2014**, *105*, 143–150.
[19] L. Yan, J. Zhuang, X. Sun, Z. Deng, Y. Li, *Mater. Chem. Phys.* **2002**, *76*, 119–122.
[20] J. Wang, S. Kaskel, *J. Mater. Chem.* **2012**, *22*, 23710.
[21] L. Gao, H. Lu, H. Lin, X. Sun, J. Xu, D. Liu, Y. Li, *Chem. Res. Chinese Univ.* **2014**, *30*, 441–446.
[22] Y. Wu, J.-P. Cao, X.-Y. Zhao, Z.-Q. Hao, Q.-Q. Zhuang, J.-S. Zhu, X.-Y. Wang, X.-Y. Wei, *Electrochim. Acta* **2017**, *252*, 397–407.
[23] M. Li, C. Liu, H. Cao, H. Zhao, Y. Zhang, Z. Fan, *J. Mater. Chem. A* **2014**, *2*, 14844–14851.
[24] Z. Wang, Y. Tan, Y. Yang, X. Zhao, Y. Liu, L. Niu, B. Tichnell, L. Kong, L. Kang, Z. Liu, F. Ran, *J. Power Sources* **2018**, *378*, 499–510.
[25] J. Maruyama, S. Maruyama, T. Fukuhara, K. Hanafusa, *J. Phys. Chem. C* **2017**, *121*, 24425–24433.
[26] J.-P. Randin, E. Yeager, *J. Electroanal. Chem. Interfacial Electrochem.* **1972**, *36*, 257–276.

Concluding Remarks

This dissertation was the compilation of studies showcasing the potential natural polymer nanofibers as prime candidates as carbon precursors when using nanoparticle templating to control and improve the morphology and porosity of carbon materials.

In Chapter 1, TEMPO-oxidized cellulose nanofibers (TOCN) dispersed in water were paired with Pluronic F-127 (PF127)-stabilized polystyrene latex (PSL) to induce templating. Through hydrothermal treatment, a unique structure of fused carbon spheres with a honeycomb surface was created. It was confirmed this structure is formed through Pluronic F-127 acting as both an interface stabilizer as well as the source for a larger secondary template, which is retained even after freeze-drying the hydrochar. The amount of PSL and PF127, the conditions of hydrothermal treatment, and the carbonization temperature all had an effect on the overall formation of the carbon monolith (CM). The hierarchical porosity obtained from PSL and PF127 resulted in higher surface area and potential for this material to be used as an oil adsorbent for oil-water separation applications.

In Chapter 2, the second-most abundant natural polymer, chitin, was also oxidized using TEMPO to yield chitin nanofibers (CtNF). It was found that through the use of chitin nanofibers, the addition of an interface stabilizing polymer becomes unnecessary when using PSL as the porogen. Therefore, CtNF-based porous carbon monoliths synthesized *via* hydrothermal carbonization had a more uniformly distributed mesopore structure, and even higher template loading capacity than that of cellulose-based carbon. The effects of hydrothermal treatment, the amount of PSL, as well as carbonization temperature were investigated. After developing micropores through KOH activation, the material was found to be fit for electrochemical applications due to it high surface area, chemical inertness, and graphene edge site exposure coming from the selective removal of amorphous carbon.

Lastly, in Chapter 3 it was shown that a fully-optimized system for synthesizing templated activated carbon (TAC) was possible through direct conversion of TOCN with MgO nanoparticles (NPs). Impregnating the TOCN fibers with KOH allowed for an integrated heat treatment being possible, where MgO NP drying, carbonization, and activation could occur consecutively within one heat treatment cycle. The method is very facile, rapid, and energy-efficient, making both the reagents as well as the synthesis method being more eco-friendly. KOH and MgO both acted as porogens for micro- and mesopore, respectively. Activation temperature was also optimized to maximize the surface area of TAC. The material was also tested for its electrochemical properties, and found that it also had potential for being used as a supercapacitor electrode.

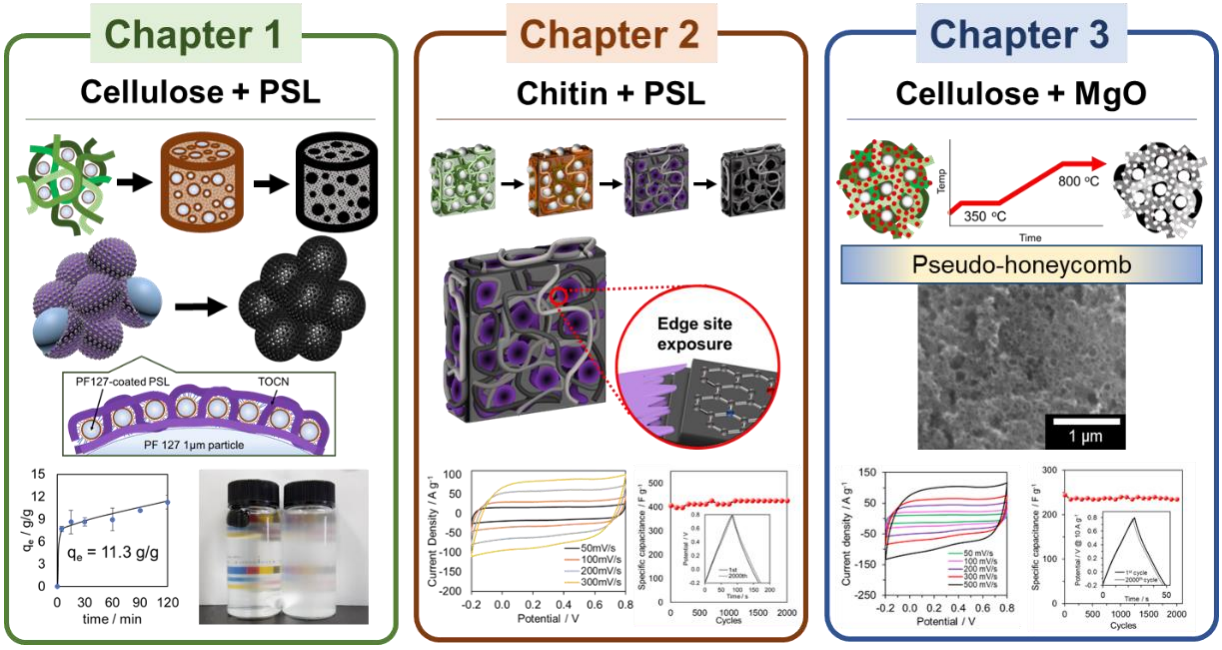

Scheme B-1. Graphical diagram for this dissertation.

In summary, natural polymer nanofiber-based materials with its NP-stabilizing properties allows this material to be a reliable biomass precursor material for converting into porous carbon. Using this type of biomass expands the potential and could help further

incentivize the use of biomass as a precursor material not only to help create an eco-friendly circular economy, but also through advantages in chemical properties. With this, a long-term and truly sustainable approach to porous carbon could help reshape the future of fields that require carbon materials as components or active ingredients.

List of Publications

1. Fused sphere carbon monoliths with honeycomb-like porosity from cellulose nanofibers for oil and water separation

   Mark Adam Ferry, Jun Maruyama, Taka-Aki Asoh, Hiroshi Uyama

   RSC Advances, **2021**, 11, 2202-2212.

   https://doi.org/10.1039/D0RA08950H

2. Porosity-induced improvement in KOH activation of chitin nanofiber-based porous carbon leading to ultrahigh specific capacitance

   Mark Adam Ferry, Jun Maruyama, Taka-Aki Asoh, Hiroshi Uyama

   ChemSusChem, **2022**, e202200932.

   https://doi.org/10.1002/cssc.202200932

3. Facile synthesis of templated activated carbon from cellulose nanofibers and MgO nanoparticles *via* integrated carbonization-activation method as an eco-friendly supercapacitor

   Mark Adam Ferry, Jun Maruyama, Taka-Aki Asoh, Hiroshi Uyama

   Electrochemistry, **2022**, 90, 7, 077004.

   https://doi.org/10.5796/electrochemistry.22-00059

List of Conferences

1. **Mark Adam Ferry**, Jun Maruyama, Taka-Aki Asoh, Hiroshi Uyama, "TEMPO-oxidized nanocellulose-based mesoporous carbon synthesis and optimization *via* soft templating and hydrothermal reaction", *FilSSO Filipino Scholars Symposium 2018* (FSS 2018), Osaka, Japan, 10 Dec 2018.

2. **Mark Adam Ferry**, Jun Maruyama, Taka-Aki Asoh, Hiroshi Uyama, "Synthesis of fused hollow carbon spheres with honeycomb surface from nanocellulose for electrochemical applications", FilSSO *Filipino Scholars Symposium 2019* (FSS 2019), Osaka, Japan, 21 Jun 2019.

3. **Mark Adam Ferry**, Jun Maruyama, Taka-Aki Asoh, Hiroshi Uyama, "Green synthesis of hollow carbon spheres with honeycomb surface from cellulose nanofibers", *JSPS Core-to-Core Program Bioplastic Joint Satellite Symposium*, Davao, Philippines, 23-25 Jul 2019

4. **Mark Adam Ferry**, Jun Maruyama, Taka-Aki Asoh, Hiroshi Uyama, "Synthesis of honeycomb porous carbon monoliths from TEMPO-oxidized cellulose nanofibers for oil-water separation", *10th JACI/GSC Symposium*, Online, 28-29 Jun 2021.

5. **Mark Adam Ferry**, Jun Maruyama, Taka-Aki Asoh, Hiroshi Uyama, "Synthesis of fused hollow carbon spheres with honeycomb surface *via* hydrothermal carbonization of cellulose nanofibers for oil water separation", *The International Chemical Congress of Pacific Basin Societies 2021* (Pacifichem 2021), Online, 16-21 Dec 2021.

6. **Mark Adam Ferry**, Jun Maruyama, Taka-Aki Asoh, Hiroshi Uyama, "Porosity-induced improvement of KOH activation of chitin nanofiber-based carbon", *11th JACI/GSC Symposium*, Online, 15-16 Jun 2022.

Acknowledgements

Through the 5 years I have stayed in Osaka University, I am blessed to have met amazing people that without them, this endeavor would not have been possible.

I would like to thank Osaka University and the Japanese Government Ministry of Science, Culture, Sports, and Education (MEXT) for the opportunity and financial aid to undertake graduate studies in Osaka University.

I would like to express my sincerest gratitude to my advisor, Prof. Hiroshi Uyama of Osaka University for believing in me and allowing me to be a part of his laboratory as a Masters and Doctoral student from 2017 to 2022. His support and innumerable opportunities he had given me allowed me to grow as a researcher.

I would also like to express my utmost gratitude to Dr. Jun Maruyama of the Osaka Institute of Industrial Science and Technology (ORIST) for the invaluable support and guidance through all of the research we have collaborated with. He is what made all of the research possible. He is the reason why I can proudly stand where I am today.

I would like to thank to Prof. Taka-Aki Asoh of Osaka University for being the advisor I could count on for the little, everyday things that are equally important in doing research work. I would like to thank Prof. Hidehiro Sakurai for believing in me and giving me the chance to apply for Osaka University when he visited my university. He gave me the fighting chance to succeed. I would also like to thank to Prof. Yu-I Hsu for her incredible support during the last phases of this research. I would also like to thank my manuscript reviewers Professor Masaya Nogi and Professor Takashi Hayashi for their invaluable insight for this endeavor.

I would like to thank all the people who had given me technical support to finish this research: the Division of Environmental Technology in ORIST (Shohei Maruyama and Tomoko Fukuhara), Kuwabata Laboratory of Osaka University (Prof. Susumu Kuwabata and Prof. Taro Uematsu), Sakurai Laboratory (Prof. Hidehiro Sakurai, Prof. Yuki Yakiyama, and

Prof. Yuta Uetake), Imanaka Laboratory (Prof. Nobuhito Imanaka, Prof. Shinji Tamura, and Yo Shimura), and Hitoshi Haneoka of the Comprehensive Analysis Center.

I would like to thank the previous and present staff of Uyama Laboratory – Yoko Uenishi, Tomoko Shimizu, Mie Iwamoto, Dr. Yasushi Takeuchi, Dr. Xinnan Cui, Kyoko Tanimura, Chiaki Yoshizawa, Erina Katsuragawa, Chikako Abe, Fumie Kamada, and Prof. Takashi Tsujimoto for making the laboratory feel like my second home.

I would like to thank all the students of Uyama Lab from 2017 to 2022. Most notably, I would like to say special thanks to: Dr. Tomonari Kanno, Haouyan Zhou, Jin Qian, Jinhee Kim, Moe Sugahara, Prof. Akihide Sugawara, Yuuya Higuchi, Tatsuya Higashigaki, Lulu Huang, Zhicheng Suo, Qianying Li, Weiting Wu, Ginga Hoshi, Toshiki Honda, Tatsuya Yamamoto, Anna Shigaki, Kotoha Fukushima, Jiaxin Alice Chen, Yuya Fujiwara, Shiho Takai, Airi Ozaki, Dr. Chen Qian, Dr. Yankun Jia, Dr. Zhengtian Xie, Dr. Toshiki Tamiya, Dr. Shunsuke Mizuno, Dr. Masatoshi Kato, Dr. Naharullah Bin Jamaluddin, Dr. Raghav Soni, Dr. Hanyu Wen, Dr. Yanting Lyu, Yuka Kashihara, Kohei Kikkawa, Yuji Kiba, Takeshi Hiraoka, Yuki Shioji, Atsushi Koizumi, Yuxiang Jia, Nontarin Roopsung, Emil Hajili, Madhurangika Panchabashini Horathal Pedige, Manji He, Kazuki Shibasaki, May Myat Noe, Hasinah binti Mohamed Rafiq, Motoi Oda, Kaita Kikuchi, Koki Tsujita, Hajime Fujimori, Suzune Miki, An Thuy Le Huynh, Izzah Durrati Binti Haji Abdul, Rika Onishi, and Judit Rebeka Molnar.

I would like to mention my fellow friends and students who were with me the entire journey: Nazgul Assan, Manunya Tepakidareekul, Justine Kalaw, Xinxi Li, Yan Wang, Luwei Zhang, and Meng Wei. We have made it.

Most importantly, I would like to dedicate this research to my family, Maria Dolores Malaluan Ferry, Henry Timoteo Ferry, and Trisha Marie Malaluan Ferry, as well as to my partner Shohei Fukagawa. Your love and support were, and always will be, my inspiration.

Mark Adam Malaluan Ferry
June 2022

Erit lux mundi in cognitione scientiae.

Maging ilaw ng mundo sa pamamagitan ng pagtuklas ng agham.

Be a light in the world by discovering science.

科学の発見することで世界の光になれ。